Ageostrophic effects on large scale circulation, eddy mixing and dissipation in the ocean

Dissertation zur Erlangung des Doktorgrades
an der Fakultät für Mathematik, Informatik und Naturwissenschaften
Fachbereich Geowissenschaften
der Universität Hamburg

vorgelegt von
Nils Brüggemann
Hamburg, 2013

– Korrigierte Fassung –

Tag der Disputation: 24.01.2014

Folgende Gutachter empfehlen die Annahme der Dissertation:

Prof. Dr. Carsten Eden

Dr. Johann Jungclaus

Eidesstattliche Erklärung

Hiermit erkläre ich an Eides statt, dass ich die vorliegende Dissertationsschrift - abgesehen von der Beratung durch meine akademischen Lehrer - selbst verfasst und keine anderen als die angegebenen Quellen und Hilfsmittel benutzt habe. Diese Arbeit hat weder ganz, noch in Teilen, bereits an anderer Stelle einer Promotionskommission zur Erlangung des Doktorgrades vorgelegen.

Hamburg, 04.12.2013

Zusammenfassung

Die im Zuge dieser Doktorarbeit angefertigten Studien sollen zu einem besseren Verständnis des Einflusses ageostrophischer Prozesse auf die Ozeandynamik beitragen. Dazu werden drei unterschiedliche Fallstudien betrachtet – die großskalige Zirkulation, durch Wirbel induzierte Vermischungsprozesse innerhalb der Deckschicht des Ozeans sowie die Rolle ageostrophischer Dynamik hinsichtlich der Ermöglichung eines direkten Weges zur Energiedissipation. Des Weiteren wird untersucht, in wie weit es möglich ist, die komplexe ageostrophische Dynamik mittels Parametrisierungen zu vereinfachen.

In der ersten Fallstudie werden zonal gemittelte Modelle der großskaligen meridionalen Umwelzbewegung untersucht. Während die Dynamik im Inneren des Ozeans mittels einer geostrophischen Balance beschrieben werden kann, sind für eine korrekte Beschreibung des westlichen Randstromes ageostrophische Prozesse zu berücksichtigen. Hinsichtlich zonal gemittelter Modelle ist es von entscheidender Bedeutung, dass beide dynamischen Regime, sowohl der innere Ozean als auch der westliche Randstrom, angemessen repräsentiert werden. Es wird gezeigt, dass Modelle, die keine angemessene Berücksichtigung beider Regime beinhalten, dynamische Inkonsistenzen aufweisen. In dieser Arbeit wird daher eine neue Parameterisierung für den zonal gemittelten Transport entwickelt, in der beide dynamischen Regime berücksichtigt werden und die daher keine dynamischen Inkonsistenzen aufweist. Die dynamische Konsistenz der neuen Parametrisierung kann aus einer guten Übereinstimmung zwischen einem zonal aufgelösten und dem neu entwickelten zonal gemittelten Model geschlossen werden.

Die zweite Fallstudie beschäftigt sich mit der Vermischung von Wirbeln innerhalb der Deckschicht des Ozeans. Eine schwache Stratifizierung der Deckschicht hat zur Folge, dass ageostrophische Prozesse innerhalb der Deckschicht eine große Rolle spielen. Zwei Parametrisierungen werden untersucht, die explizit diese ageostrophischen Prozesse berücksichtigen. Die erste Parametrisierung basiert auf einer linearen Stabilitätsanalyse, während der zweiten eine Skalierung der potentiellen Energiebilanz zu Grunde liegt. Die Fähigkeit beider Parametrisierungen, den Vermischungseffekt dieser Wirbel zu diagnostizieren wird mittels numerischer Simulationen für eine Vielzahl verschiedener dynamischer Bedingungen untersucht. Ein wichtiges Resultat dieser Untersuchungen ist, dass sich die parametrisierten Wirbelflüsse im Mittel nicht weniger als um einen Faktor zwei von den diagnostizierten Wirbelflüssen unterscheiden. Für ein Szenario einer sich im Gleichgewicht befindlichen Strömung schneidet dabei die Parametrisierung, die auf der linearen Stabilitätsanalyse basiert, ein wenig besser ab. Im Gegensatz dazu schneidet die Parametrisierung, die auf

der Skalierung der potentiellen Energiebilanz basiert, in einem Szenario einer sich restratifizierenden Dichtefront besser ab. In beiden Szenarien wird die vertikale Struktur der Wirbelflüsse besser von der auf der linearen Stabilitätsanalyse basierenden Parametrisierung wiedergegeben.

Die dritte Fallstudie untersucht den Einfluss von ageostrophischer Dynamik auf die kinetische Energiedissipation. Numerische Simulationen für eine Vielzahl von dynamischen Bedingungen, charakterisiert durch ihre Richardson-Zahl, werden benutzt, um den Energiefluss im Wellenzahlraum zu diagnostizieren. Die Untersuchungen zeigen, dass in der Gegenwart quasi-geostrophischer Dynamik ein Fluss der kinetischen Energie hin zu großen Skalen erfolgt. Im Gegensatz bewirken ageostrophische Prozesse einen kinetischen Energiefluss zu kleineren Skalen. Horizontal divergente Geschwindigkeiten, welche sich unter ageostrophischen Bedingungen entwickeln, sind verantwortlich für diesen Fluss zu kleineren Skalen. Eine wichtige Konsequenz ist, dass die Energiedissipation auf kleinen Skalen in der Gegenwart von ageostrophischen Prozessen stärker ist. Um den Effekt der ageostrophischen Dynamik auf die Energiedissipation zu quantifizieren, wird die Abhängigkeit der Energiedissipation von der Richardson-Zahl untersucht und ein Potenzgesetz abgeschätzt, welches die Abhängigkeit der kleinskaligen Energiedissipation von der Richardson-Zahl beschreibt.

Abstract

This thesis aims to provide a better understanding of the role of ageostrophic processes in ocean dynamics by analyzing three different case studies – the large-scale circulation, the mixing of eddies in the upper ocean and the ability of ageostrophic dynamics to feature a direct route to dissipation. Furthermore, it examines to which extent parameterizations can yield adequate simplifications of the more complex ageostrophic phenomena.

The first case study concerns zonally averaged models of the large-scale meridional overturning circulation. Ageostrophic processes need to be considered here to correctly describe the dynamics in western boundary currents, while the interior ocean can be described by a geostrophic balance. Both, interior geostrophic and ageostrophic dynamics in the western boundary current need to be considered for the zonally averaged flow. It is illustrated that many zonally averaged models which do not consider both regimes show dynamical inconsistencies in comparison with zonally resolved models. A new parameterization for the zonally averaged flow is developed, in which both dynamical regimes are directly represented and which does not suffer from those inconsistencies. Zonally resolved models show good agreement with the new zonally averaged model, demonstrating that the new parameterization is dynamically consistent.

The second case study deals with the mixing of eddies in the upper ocean. Since the stratification is often weak within the mixed layer, ageostrophic processes are likely to occur here. Two parameterizations for the eddy mixing are compared, which especially take ageostrophic dynamics into account. The first is based on linear stability analysis while the second is based on a scaling of the potential energy release. Numerical simulations for a wide range of dynamical conditions are used to diagnose the ability of these parameterizations to predict the mixing effect of the eddies. It turns out that the mean difference between both parameterizations and the diagnosed eddy fluxes is less than a factor of two. While the parameterization based on linear stability analysis performs slightly better in an equilibrated forced-dissipative flow scenario, the parameterization based on the scaling of the potential energy release performs better in a scenario of a re-stratifying density front. In addition it is found that the vertical structure of the eddy fluxes is better described by the former in both scenarios.

The third case study investigates the role of ageostrophic dynamics for kinetic energy dissipation. Numerical simulations for a wide range of different dynamical conditions characterized by their Richardson number are used to diagnose the energy flux in wavenumber space. It is found that quasi-geostrophic dynamics feature an upscale kinetic energy flux

while kinetic energy is transferred towards smaller scales for ageostrophic dynamics. Horizontal divergent velocities evolving under ageostrophic conditions can be identified to be responsible for the downscale flux. An important consequence is that the small-scale dissipation is larger in the presence of ageostrophic dynamics. To quantify the effect of ageostrophic dynamics on the small-scale dissipation, its dependency on the Richardson number is investigated and a power law relating the energy dissipation with the Richardson number is estimated.

Contents

Chapter 1

Introduction

The equations that describe the physical components of the climate system are known in principle for more than 100 years. However, their solutions bear still major challenges since the non-linear character of these equations inhibits analytic solutions. It is often not necessary to consider these mathematical equations in their full complexity. In such cases, it is possible to make assumptions about the underlying dynamics, which reduce the mathematical complexity without inhibiting adequate solutions.

A basic example for ocean dynamics is the concept of geostrophic balance, in which the horizontal pressure gradient force is nearly balanced by the Coriolis force. The resulting flow can be directly calculated from the underlying pressure field. It changes only in time if there are temporal changes of the pressure field. The geostrophic balance holds often to a good approximation for the large-scale dynamics in the interior ocean. However, other ageostrophic forces become important on shorter spatial and temporal scales or close to the boundaries of the ocean, and the geostrophic balance is not a reasonable assumption anymore.

Fig. 1.1 indicates spatial and temporal scales of important dynamical regimes within the ocean. Dynamics on the largest spatial and temporal scales, like Rossby waves or mesoscale eddies, are in geostrophic balance. In contrast, ageostrophic processes become important for processes on smaller space and time scales, like internal waves or small-scale turbulence. Although the scales of these different dynamics might be separated by some orders of magnitude, it is essential to note that there are many interactions between the different regimes and thus interactions of processes between different length and time scales. In particular, it is not sufficient to consider only the Rossby wave and mesoscale eddy regime to understand the large-scale circulation. Ageostrophic processes directly influence

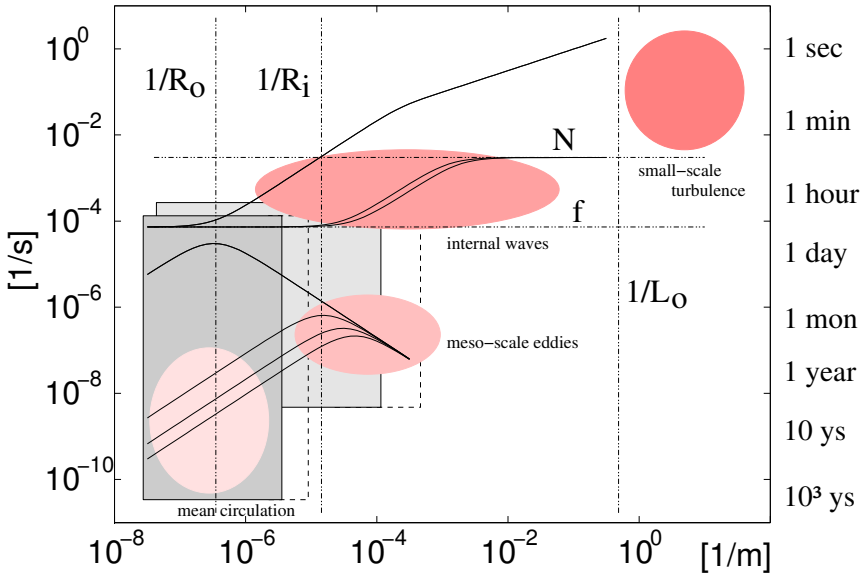

Figure 1.1: Space and time scales of important ocean processes. Red circles denote important dynamical regimes. The lower left grey rectangle indicates the resolution of current global climate models, while the upper right rectangle denotes the resolution of current basin-scale ocean models. Dashed extensions of the rectangles indicate the expected increase in resolution due to an increase in computational power expected for the next years. Black lines denote the dispersion relation of Rossby waves (lower left side), internal waves (middle) and surface waves (upper half). The horizontal dashed lines indicate the regime for internal waves with frequencies between the Coriolis parameter f and the vertical stratification N. Vertical dashed lines indicate the first internal Rossby radius R_i, the barotropic Rossby radius R_o and the Ozmidov scale L_o (from Carsten Eden personal communication, see also Olbers et al. (2012)).

the large-scale circulation e.g. by providing a sink for kinetic energy due to dissipation or by providing potential energy due to diapycnal mixing. Both phenomena are key processes for larger scale dynamics, like the meridional overturning circulation (MOC), for instance.

Since numerical models require a discretization in space and time, they have to neglect processes below their spatial and temporal resolution. Limitations in the computational power are responsible for the fact that current ocean models are not able to achieve both, a global integration for climatic relevant time periods and a resolution of ageostrophic small-scale processes. As can be inferred from Fig. 1.1, global as well as regional ocean models are hardly able to resolve the internal wave field and small-scale turbulence, although these processes influence the larger scales.

Parameterizations are a common strategy to tackle this problem. In this case, theoretically or empirically based assumptions are used to find an approximative representation of

the unresolved processes. To ensure a minimum lack of accuracy, the parameterizations itself as well as the outcome of any model using these parameterizations have to be carefully validated.

This thesis aims at investigating ageostrophic dynamics within three different case studies, a zonally averaged ocean model, the mixing of eddies in the upper ocean and the ability of ageostrophic dynamics to feature a direct route of kinetic energy to dissipation. Furthermore, it examines to which extent parameterizations can yield adequate simplifications of the more complex ageostrophic phenomena.

In Chapter 2, the influence of ageostrophic dynamics on the meridional overturning circulation (MOC) is investigated. Although the meridional circulation is considered predominantly to be in geostrophic balance, ageostrophic dynamics play a fundamental role in the establishment of a western boundary current. Therefore, they influence the entire MOC and the meridional transport of heat or other substances. Zonally averaged models of the MOC do not explicitly distinguish between the interior ocean and this western boundary current and therefore cannot directly consider both, the geostrophic and the ageostrophic regime. On the other hand zonally averaged models are a powerful tool for parameter studies or long-term simulations since the simulation of a two-dimensional domain naturally causes much less computational costs than that of a three-dimensional domain. Furthermore, to search for dynamical consistent simplifications that are necessary to develop a zonally averaged model can finally lead to a better understanding of the MOC. Therefore, a way to implicitly consider the ageostrophic boundary current and the geostrophic interior in a dynamically consistent closure for zonally averaged models is introduced in Chapter 2.

In Chapter 3, the focus is on ageostrophic processes that predominantly occur near the ocean surface. Turbulent mixing in the upper ocean causes low stratification within the first hundred meters and establishes the so called mixed layer. Eddies that arise in the mixed layer are likely to be subject to ageostrophic dynamics, in contrast to eddies in the stronger stratified ocean interior which are assumed to be in quasi-geostrophic balance. In Chapter 3 it is investigated to which extent parameterizations are able to account for the effect of mixed layer eddies. The performance of two parameterizations, the first based on linear stability analysis (Stone, 1972b) and the second based on a scaling of the potential energy release (Fox-Kemper et al., 2008), is compared for different mixed layer scenarios.

Besides the mixing of heat or other substances, a turbulent flow plays an important role for the transfer of energy between different scales. In Chapter 4, it is examined how

direction and magnitude of the energy fluxes in wavenumber space change as soon as ageostrophic processes become relevant. The main energy source of the ocean is given by atmospheric and tidal forcing. Both act predominantly on large scales like a few hundred kilometers. Energy dissipation, on the other hand, is mainly achieved due to molecular friction and diffusion, therefore occurring on the smallest scales. Thus, there have to be processes that are responsible for an energy transport from the large scales to the small molecular scales. Three-dimensional small-scale turbulence is known to provide such a downscale energy cascade (Kolmogorov, 1941) but since it acts on scales much smaller than the oceanic forcing scales, it is likely no candidate to explain the energy transfer on larger scales. In contrast, geostrophic turbulence coincides on spatial and temporal scales with the forcing scales, but the theory of geostrophic turbulence rather suggests an upscale energy transport (Charney, 1971). The geostrophic turbulence thus does not provide a direct route to dissipation. Less is known about the energy fluxes for turbulence acting between the small-scale and the geostrophic scales. Therefore, it is analyzed in Chapter 4, how ageostrophic processes like mixed layer eddies are able to influence the strength and direction of the energy flux.

In the next section, a short introduction to geostrophic and ageostrophic dynamics will be given. The explicit role of ageostrophic dynamics for the three case studies will be discussed in more detail in the following sections.

1.1 Geostrophic and ageostrophic dynamics

The equation of the vertical component of vorticity $\zeta = \partial_x v - \partial_y u$ yields some insight into the dynamics of a flow system. The non-dimensional form of this equation in hydrostatic and Boussinesq approximation reads[1]:

$$\underbrace{\gamma \partial_{\hat{t}} \hat{\zeta}}_{\text{I}} + \underbrace{\gamma \hat{\boldsymbol{u}} \cdot \hat{\nabla} \hat{\zeta}}_{\text{II}} + \underbrace{\frac{\gamma}{\mathrm{R}_\beta} \hat{\beta} \hat{v}}_{\text{III}} - \underbrace{\hat{f} \partial_{\hat{z}} \hat{w}}_{\text{IV}} = \underbrace{\mathrm{Ro} \hat{\zeta} \partial_{\hat{z}} \hat{w}}_{\text{V}} + \underbrace{\mathrm{Ro}(\partial_{\hat{y}} \hat{w} - \partial_{\hat{z}} \hat{v}) \partial_{\hat{x}} \hat{w} + \mathrm{Ro}(\partial_{\hat{z}} \hat{u} - \partial_{\hat{x}} \hat{w}) \partial_{\hat{y}} \hat{w}}_{\text{VI}} + \underbrace{\frac{\gamma \mathrm{Ek}}{\mathrm{Ro}} \hat{F}(\zeta)}_{\text{VII}}, \quad (1.1)$$

where hats indicate non-dimensional variables, $\boldsymbol{u} = (u, v, w)^T$ denotes the three-dimensional velocity, $f = 2\Omega \sin\theta$ the planetary vorticity, Ω the rotation frequency of the earth, θ

[1] Derivations and scalings of this section closely follow Olbers et al. (2012), chapter five.

latitude, β the meridional gradient of the planetary vorticity and $F(\zeta)$ friction. The magnitudes of the individual terms in Eq. (1.1) depend on dimensionless parameters like the Rossby number Ro (ratio between inertial and Coriolis force), the Rhines number R_β (ratio between inertial force and variations of the Coriolis force over the considered spatial scales), the ratio between advection of relative vorticity and stretching of planetary vorticity γ and the Ekman number Ek (ratio between friction and Coriolis force). In terms of characteristic scales of a flow system these parameters can be expressed as

$$\mathrm{Ro} = \frac{U}{fL}, \qquad \mathrm{R}_\beta = \frac{U}{\beta L^2}, \qquad \gamma = \frac{U^2 H}{W L^2 f}, \qquad \mathrm{Ek} = \frac{D}{fU}, \tag{1.2}$$

where L and H denote horizontal and vertical length scales, U and W horizontal and vertical velocity scales and D a typical scale for the magnitude of friction.

For a large part of the ocean, it is valid to assume that $\mathrm{Ro} \ll 1$, $\gamma \lesssim 1$ (see below) and $\mathrm{Ek} \ll \mathrm{Ro}$. In this case, the right hand side of Eq. (1.1) vanishes and the terms on the left hand side have to balance each other. This regime is called geostrophic.

It is common to distinguish between two important sub-regimes within the geostrophic regime, namely the quasi-geostrophic and the planetary-geostrophic regime. While the planetary-geostrophic regime is characterized by a balance between stretching (IV) and advection (III) of planetary vorticity, the quasi-geostrophic regime is characterized by a balance between stretching of planetary (IV) and advection of relative vorticity (II). The Rhines scale $L_\beta = \sqrt{U/\beta}$ which distinguishes both regimes can be obtained by comparing the magnitude of the advection of relative (II) to planetary (III) vorticity. Dynamics with typical length scales smaller than the Rhines scale, $L < L_\beta$, are in quasi-geostrophic balance. In contrast, if $L > L_\beta$, the dynamics are in planetary-geostrophic balance. Note that a balance between (III) and (IV) for the planetary-geostrophic regime implies that $\mathrm{R}_\beta < 1$ and $\gamma = \mathrm{R}_\beta$, which is only achieved if the vertical velocity scales like $W = (\mathrm{Ro}/\mathrm{R}_\beta)(H/L)U$. In contrast, a balance between (II) and (IV) for the quasi-geostrophic regime implies $\mathrm{R}_\beta > 1$ and $\gamma = 1$ and therefore a different scaling for the vertical velocity of $W = \mathrm{Ro}(H/L)U$.

The dynamical regime of planetary-geostrophic balance can be found in the interior of the ocean for the large-scale circulation (in Fig. 1.1, it corresponds to the long wave branch of the Rossby waves). In this case, the equation for the vertical vorticity component, Eq. (1.1), reduces to the Sverdrup relation $\beta v = f\partial_z w$ meaning that any source of upwelling $\partial_z w$ by e.g. wind-induced Ekman pumping or diapycnal mixing causes a poleward mass

transport. While this equation is a good approximation to the large-scale flow of the interior ocean, it is violated at the western ocean boundary where $\gamma \mathrm{Ek}/\mathrm{Ro} \approx 1$ and friction (term VII in Eq. (1.1)) enables a boundary layer current that is important for the meridional mass and heat transport. As far as models for the zonally integrated meridional flow are concerned, an interplay between the ageostrophic boundary currents and the geostrophic interior has to be carefully considered. How to parameterize both regimes in a zonally integrated flow is introduced in Chapter 2.

In contrast to the regime of planetary-geostrophic balance, the dynamical regime of quasi-geostrophic balance describes many aspects of baroclinic and barotropic instabilities, mesoscale eddies and geostrophic turbulence (in Fig. 1.1, it corresponds to the intermediate and short wave branch of the Rossby waves). It holds within large parts of the ocean except close to lateral or surface boundaries and is therefore of fundamental importance for ocean dynamics. However, especially in the ocean surface mixed layer, in regions dominated by convection or within strongly sheared and weakly stratified boundary currents, the dynamics are characterized by small vertical and horizontal spatial scales but large horizontal and vertical velocity scales yielding large Ro, large R_β and $\gamma \approx 1$. In this case, stretching of relative vorticity (V), vortex tilting (VI) and the geostrophic terms become of comparable magnitude in the vorticity balance Eq. (1.1). Furthermore, the advection of momentum is no longer negligible, and the geostrophic balance is not valid anymore.

Two aspects of these type of ageostrophic dynamics are considered in Chapter 3 and Chapter 4. In Chapter 3, it is investigated to which extent these ageostrophic dynamics influence the re-stratification of the upper ocean mixed layer and different parameterizations for the mixing of eddies induced by baroclinic instabilities are compared. The focus of Chapter 4 is on the influence of ageostrophic processes on energy dissipation. In contrast to a downscale kinetic energy flux for quasi-geostrophic dynamics (Charney, 1971), the direction of the kinetic energy flux can be reversed if the dynamic is dominated by ageostrophic processes. This change of the direction of the kinetic energy flux has large influence on the small-scale dissipation and is analyzed in Chapter 4.

1.2 Effects of ageostrophic processes on the meridional overturning circulation

Atmosphere and ocean together transport about 6 PW heat at maximum from low to high latitudes (Trenberth and Caron, 2001). The ocean's contribution of this heat flux is roughly

25% (Trenberth and Caron, 2001), which points to the importance of the ocean for the climate system. A number of current systems is responsible for this heat flux. The zonal average of all these current systems is called meridional overturning circulation (MOC).

The mechanisms that drive the MOC are mechanical forcing and internal mixing. Fig. 1.2 shows a schematic of the main processes involved in the Meridional Overturning Circulation of the Atlantic (AMOC), an important contributor to the total MOC. A simplified picture of the AMOC can be obtained by dividing it into two overturning cells, a surface cell transporting North Atlantic Deep Water (NADW) in a clockwise orientation and a lower cell transporting Antarctic Bottom Water (AABW) in an anti-clockwise orientation (a detailed review of the MOC can be found e.g. in Kuhlbrodt et al. (2007)).

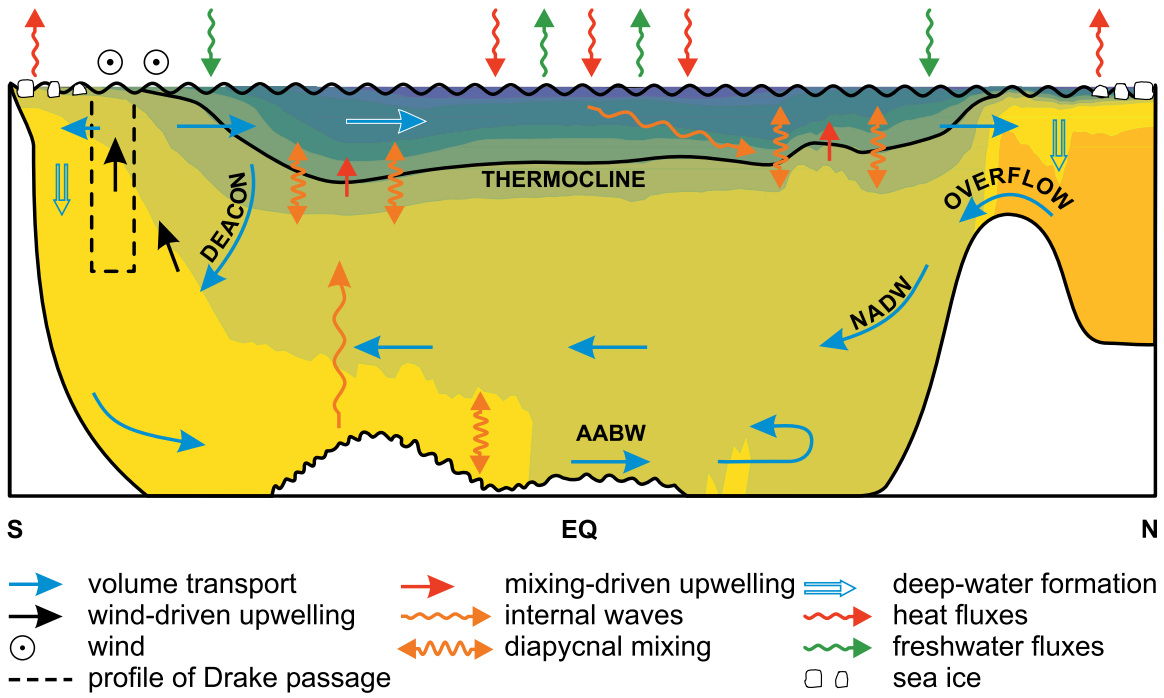

Figure 1.2: Schematic of the MOC. Color shading denotes the density structure with light surface water masses in blue and heavy bottom water masses in yellow. Volume transports are depicted by blue arrows and basically follow density contours. Two overturning cells can be identified. An upper cell containing North Atlantic Deep Water (NADW) circles clockwise and a lower cell containing Antarctic Bottom Water (AABW) circles anti-clockwise. Lifting of the dense water masses might either occur due to the breaking of internal waves and their induced diapycnal mixing (orange and red arrows) or due to wind-driven upwelling (black arrows) through Ekman suction in the Southern Ocean that is partly compensated by an eddy overturning (from Kuhlbrodt et al. (2007)).

Surface cooling by cold and dry winds causes deep water formation in the Labrador Sea and the Nordic Seas. The Greenland-Iceland-Scotland ridge system prevents a direct inflow of the dense bottom waters formed in the Nordic Seas into the North Atlantic. An overflow of the dense water masses over these ridges is accompanied by an entrainment of other water masses. Together, these water masses contribute substantially to the volume flux of the MOC (e.g. Quadfasel and Käse, 2013). The combination of the deep water masses from the Nordic Seas and those of the Labrador Sea are called North Atlantic Deep Water (NADW). The NADW spreads southwards in energetic western boundary currents and partly recirculates in the interior.

Energy is needed to lift the dense water masses up again in order to close the overturning loop. One process that induces such a lifting is diapycnal mixing. This mixing is predominantly caused by the internal waves which are generated by tidal and wind stress forcing. Energy transfer to large vertical wavenumbers by non-linear wave-wave interactions and critical layer absorption cause these waves to break. This internal wave dissipation provides energy for diapycnal mixing. Measurements of the diapycnal diffusion within the ocean reveal that this process is too small in most regions of the ocean to explain the strength of the MOC (e.g. Polzin et al., 1997). However, there are some exceptions where the diapycnal diffusion is large, e.g. over rough topography (e.g. Garabato et al., 2004).

Another competing process, responsible for lifting of dense water masses is wind-induced upwelling in the Southern Ocean. A divergence of the Ekman transport at the Southern Ocean induces an upwelling that lifts the dense deep water masses and inclines the isopycnals. Since inclined isopycnals yield baroclinically unstable conditions, mesoscale eddies are generated, which cause an overturning partly compensating the Ekman upwelling. At the surface the water mass properties are changed due to atmospheric buoyancy fluxes; e.g. heat fluxes into the ocean typically cause a warming of these water masses. The loop of the upper cell of the AMOC is closed by a return flow of the upper water masses towards the North Atlantic. Until now it is not entirely clear which process is most important in lifting the dense NADW, either wind-induced upwelling or diapycnal mixing (e.g. Ferrari and Wunsch, 2009).

The deep water formation of AABW takes place at the shelf along the Antarctic continent predominantly within the Weddel and Ross Sea. Since the water masses are denser than those of the NADW, they supply the lower circulation cell of the AMOC. On its way northward, the AABW is lifted e.g. by diapycnal mixing from the bottom to depths that

are still below the NADW and where it recirculates towards the Southern Ocean closing the lower cell of the AMOC.

Simple models have been of great benefit to obtain a qualitative understanding of the MOC. Nevertheless, fundamental open questions remain and there is still a need for a better qualitative and quantitative understanding of the different aspects of the MOC. Nowadays, this understanding is predominantly extended by the use of complex numerical ocean or climate models. However, simple models like that described in Chapter 2 are still of great benefit in e.g. interpreting results from the complex models or in deriving new hypothesis about fundamental processes of the MOC.

The box model of Stommel (1961) is one of the simplest models of the MOC. Stommel (1961) divides the ocean in two parts, a southern and northern box, and describes the overturning by an upper and lower pipe flow between both boxes (see Fig. 1.3 for a schematic of the model). Since the underlying equations of the box model are non-linear, complex solutions exist that contain multiple equilibria and hysteresis loops. Although this model only yields a very simplified qualitative picture of the MOC, it has brought interest to whether such multiple equilibria can also be found in more complex numerical simulations. In fact, McManus et al. (2004) report large variations concerning the MOC strength during the past and Rahmstorf (1996) and Rahmstorf et al. (2005) find multiple equilibria and hysteresis loops related to different fresh water fluxes in more complex numerical ocean models. However, Stommel's box model does not make any assumptions of a geostrophically balanced flow. An astonishing fact, keeping in mind that by far the largest part of the ocean is in geostrophic balance. Hence, the model implicitly assumes that the overturning can exclusively be described by frictionally dominated and thus ageostrophic flows.

A different approach is taken by Stommel and Arons (1960) who assume that the interior flow is in geostrophic balance. In addition, a vertical decomposition of the ocean into an upper and an abyssal layer is assumed. The vertical water exchange between both layers is simplified such that it consists of two parts. A local prescribed deep water source pumps water from the upper into the lower layer. Simultaneously, a homogeneously distributed upward mass flux balances this localized deep water source. The former might be interpreted as parameterization for downwelling induced by ocean convection while the latter might be understood as a representation of diapycnal mixing. If all these assumptions are applied, the resulting equations that describe the flow are linear and can be solved analytically. Despite these simplifications, the model describes a flow system that

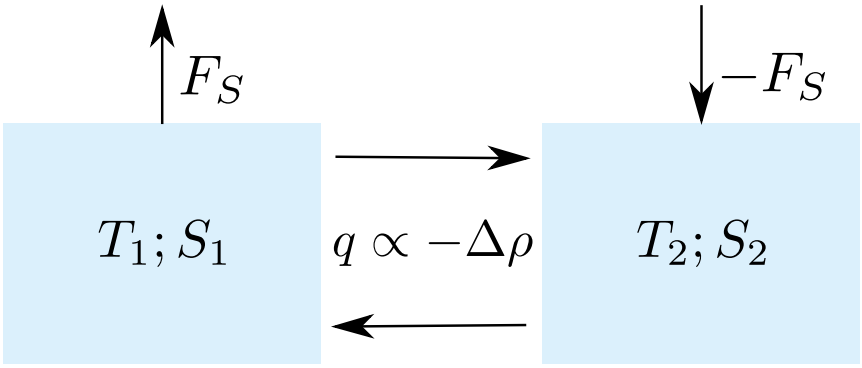

Figure 1.3: Schematic of the Stommel (1961) box model. The ocean is divided into a northern and southern box connected with a surface and an abyssal pipe flow q. The magnitude of q is assumed to be proportional to the density difference $\Delta\rho$ between both boxes. The surface heat flux is assumed to keep the temperature always at the fixed values T_1 and T_2 for the southern and northern box, respectively. Salinity is allowed to change by a fresh water flux F_S that is equal in magnitude but of opposing sign for both boxes. The density difference $\Delta\rho$ that controls the exchange flow q is calculated by a linear equation of state. The direction of the overturning (sign of q) depends on the strength of F_S which sets the pressure difference $\Delta\rho$.

already contains important aspects of the MOC, in particular it predicts the existence of a deep western boundary current that is not part of the geostrophic balanced interior flow. To explain the balance in this western boundary current, friction and thus ageostrophic dynamics, has to be taken into account.

The models discussed so far are only very rudimentary representations of the MOC. A next step towards more realistic models is to consider zonally averaged primitive equations. In these type of models, the complexity of a three dimensional flow is reduced by projecting the flow on the meridional-vertical plane. Complications arise in such a concept as soon as zonal gradients of a quantity begin to play a role. These gradients cannot be represented in a zonally averaged framework and thus have to be parameterized. Since any meridional flow in geostrophic balance is determined by a zonal pressure gradient, there is a priori no information about the geostrophically balanced meridional transport in a zonally averaged model. If the geostrophically balanced part of the meridional flow is of major importance as normally assumed, any zonally averaged ocean model misses a fundamental aspect of the MOC as long as there are no parameterizations for the zonal pressure gradient.

Parameterizations of Marotzke et al. (1988) and Wright and Stocker (1991) for the zonally integrated meridional flow assume that friction is at least as important as the Coriolis force in the meridional momentum budget. In this case, the meridional pressure

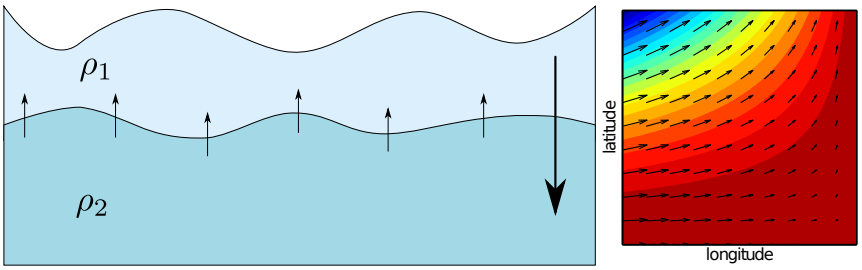

Figure 1.4: Left: Two dimensional sketch of the Stommel and Arons (1960) model. The ocean is divided into two layers and the interchange between both layers is prescribed by a localized downward volume flux (large black arrow) and spatial homogeneous upwelling (small black arrows). Right: Horizontal flow in the lower layer (arrows). Assuming a northern deep water source and homogeneous upwelling yields a northward flow along pressure contours (color shaded) in the lower layer (opposite in the upper layer). Mass conservation demands a westward boundary current that flows southward in the lower and northward in the upper layer. The prediction of such western boundary currents is one of the main results of the Stommel and Arons (1960) model.

gradient is proportional to the friction on the meridional flow and therefore directly related to the strength of the meridional flow itself. Such type of closure is quite similar to the assumptions made in Stommel's box model. However, Straub (1996) notes that the assumption of Stommel (1961) by which the meridional flow is determined by the meridional pressure gradient is inconsistent to the model of Stommel and Arons (1960) where the meridional flow is only determined by the location of the deep water source and not by the meridional pressure gradient. The model of Stommel and Arons (1960) is directly based on the planetary-geostrophic balance of the vorticity equation Eq. (1.1). Therefore, it is assumed to be more appropriate to describe the local meridional mass transport. In contrast Stommel's box model only considers the integrated effect of the meridional mass transport.

Chapter 2 of this thesis aims at answering the questions:

- Are zonally averaged ocean models that parameterize the zonally averaged meridional flow with the zonally averaged meridional pressure gradient dynamically inconsistent?

- If yes, how can geostrophic and ageostrophic dynamics be considered in order to obtain a dynamical consistent model of the zonally averaged meridional overturning circulation?

1.3 Parameterizations for eddy fluxes in an ageostrophic environment

Studies from Holland (1978), among others, reveal that mesoscale eddies have a major influence on the large-scale circulation and many studies aim at quantifying this influence (e.g. Gent and McWilliams, 1990; Larichev and Held, 1995; Killworth, 1997; Eden, 2011). As soon as more sophisticated satellite data with increased spatial resolution became available, variability even below the spatial scales of the mesoscale eddy field – the so called sub-mesoscale – was observed (Scully-Power, 1986; Munk et al., 2000). Fig. 1.5 shows two pictures of such phenomena. The first is a photograph taken from an astronaut out of a space shuttle where microlayer surfactants that become visible in the sunglitter indicate cyclonic spiral-shaped eddies. The second picture shows a phytoplankton bloom off the coast of Argentina taken by the NASA MODIS/TERRA sensor[2] with many filaments at the edges of the phytoplankton patch. Both patches indicate strongly sheared filaments that are typical for sub-mesoscale processes.

Meanwhile, a variety of processes like e.g. ageostrophic baroclinic instability, frontogenesis or symmetric instability have proven to be responsible for sub-mesoscale features (e.g. Haine and Marshall, 1998). A common feature of those processes is the fact that they come along with large Rossby numbers (e.g. Thomas et al., 2008). The considerations of Sec. 1.1 demonstrate that ageostrophic dynamics in the upper ocean are caused by the stretching and tilting of relative vorticity (term V and VI in Eq. (1.1)) and not necessarily by friction (term VII). Thus, the ageostrophic dynamics considered here are different from those discussed for the large-scale meridional circulation in Sec. 1.2. For sub-mesoscale eddies rather deviations from a quasi-geostrophic balance (term II and IV) than from a planetary-geostrophic balance (term III and IV) are relevant.

Fig. 1.6 shows a sketch of a typical situation in the upper ocean that causes sub-mesoscale eddies. Wind-induced turbulence and surface cooling are responsible for a low stratification of the upper water masses in contrast to the stronger stratified underlying pycnocline. These low stratified water masses are often accompanied by meridional density gradients which are caused, e.g. by mesoscale eddy straining or differential atmospheric heat and fresh-water fluxes. In this case, the flow is baroclinically unstable and features eddies that re-stratify the inclined density surfaces by converting potential energy into

[2]The picture is taken from `http://lance-modis.eosdis.nasa.gov/cgi-bin/imagery/single.cgi?image=Argentina.A2004348.1415.1km.jpg`.

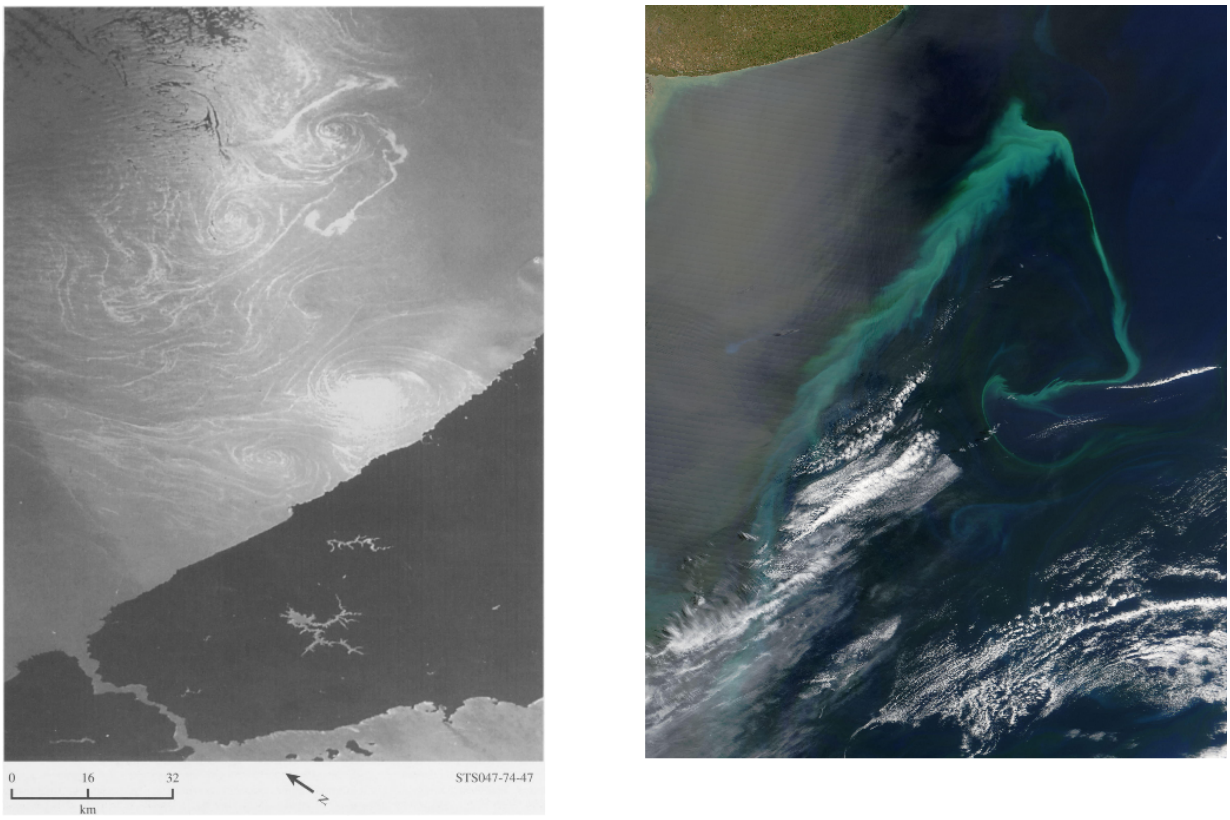

Figure 1.5: (left) Sunglitter photograph of spiral eddies in the Mediterranean off Egypt taken from a space shuttle cruise with a handheld Hasselblad 6x6 cm camera (from Munk et al. (2000)). (right) Phytoplankton bloom off Argentina taken of the NASA MODIS/TERRA sensor.

kinetic energy. The effect of these eddies on the density field can be decomposed into an advective and a diffusive component. While the advective component is responsible for the re-stratification by an adiabatic overturning of the inclined density surface (see Fig. 1.6), the diffusive component is diabatic and causes diapycnal mixing.

An appropriate scale for eddies arising as a result of baroclinic instability is given by the first baroclinic Rossby radius $L_r = NH/f$, where N is the square root of the vertical buoyancy stratification, H a depth scale and f the Coriolis parameter. Low values of the stratification and the depth scale of the mixed layer feature a Rossby radius that is much smaller than its counterpart of the ocean interior. Therefore, the eddies occurring in the mixed layer have smaller spatial scales than interior mesoscale eddies. Since the velocity of the mixed layer eddies is comparable to those of the ocean interior, the small spatial length scales of the mixed layer eddies yield a large Rossby number. In fact, the Rossby

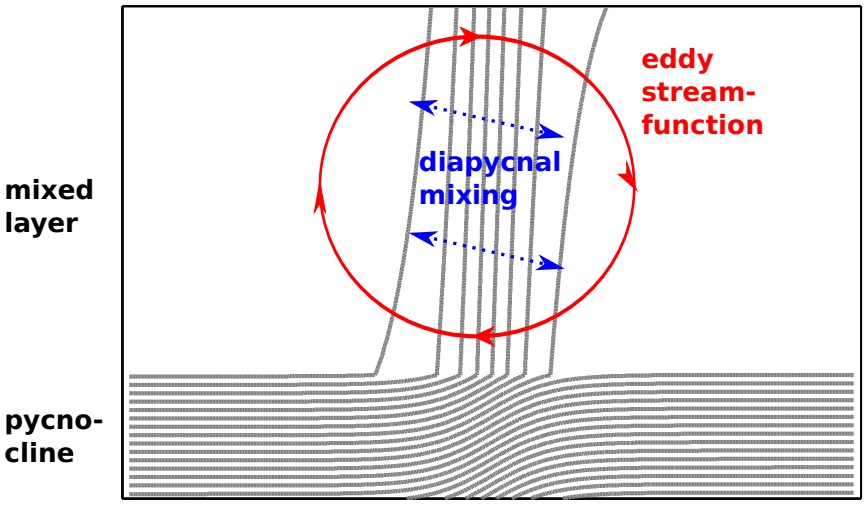

Figure 1.6: Schematic of the spin-down of a buoyancy front induced by mixed layer eddies (adapted from Fox-Kemper et al. (2008)). Contours indicate buoyancy with lighter water masses at the left hand side and heavier at the right hand side of the domain. Eddies extract available potential energy and convert it into eddy kinetic energy, developing an overturning circulation that ranges from the ocean surface to the bottom of the mixed layer determined by the depth of the pycnocline. In addition, mixed layer eddies can be responsible for enhanced diapycnal diffusivities.

number is often larger than one, indicating that ageostrophic processes are relevant for the mixed layer eddies (McWilliams, 1985b; Munk et al., 2000; Shcherbina et al., 2013).

For numerical ocean models, the ageostrophic dynamics build a major challenge since they occur on scales of the order of meters to a few kilometers and current global ocean models as well as many regional ocean models are not able to directly resolve mixed layer eddies (the resolution of a state of the art global ocean model might inferred from e.g. Jungclaus et al. (2013)). Nevertheless, their mixing has large influence on the transport of heat, trace gases and organic substances between the upper ocean mixed layer and the abyssal ocean (Oschlies, 2002). Therefore, the eddies influence the air-sea gas exchange, the depth of the mixed layer and other important quantities of the climate system by interfering with bio-geochemical cycles and the air-sea gas exchange of trace gasses like e.g. CO_2 or heat (Lévy et al., 2001, 2012).

In order to account for the influence of mixed layer eddies on the climate system, parameterizations have to be developed that represent the eddy overturning and mixing. Fox-Kemper et al. (2008) use a scaling for the potential energy release induced by baroclinic instability to relate this energy release with the kinetic energy of the eddies. By using

these considerations, they construct a parameterization that especially accounts for eddies in the mixed layer, but might also be representative of the mixing of mesoscale eddies. A competing approach results from Stone (1972b), who uses linear stability analysis for a parameterization of eddy mixing induced by ageostrophic baroclinic instability. Although this approach is aimed to parameterize ageostrophic mixing effects in the atmosphere, it is likely to be also applicable within the ocean mixed layer.

These two approaches are based on very different concepts. Therefore, it is difficult to argue which parameterization is more applicable. In Chapter 3, the parameterizations of the eddy fluxes are related to fundamental parameters of the flow: the Richardson number as the ratio between vertical stratification and vertical shear of the horizontal velocity, the Rossby number and the aspect ratio. Using these parameters in the algebraic expression makes a direct comparison of the parameterizations possible and the following question is discussed:

- What are the main differences between eddy flux parameterizations based on linear stability analysis and parameterizations based on scalings of the eddy potential energy release?

Relating the parameterized eddy mixing of the flow to its dynamical characteristics allows to investigate the performance of the parameterization under geostrophic as well as under ageostrophic dynamical conditions. A numerical ocean model is used to simulate the eddy mixing under such idealized different dynamical conditions. By comparing the diagnosed eddy fluxes with the parameterized counterparts, the following question is addressed:

- How do parameterizations of mixed layer eddy fluxes perform under ageostrophic and geostrophic conditions?

1.4 The route to dissipation in the presence of ageostrophic dynamics

Understanding and quantifying the ocean's energy budget is of fundamental importance for future climate predictions. Nevertheless, it bears major challenges since it requires a detailed understanding of nearly all ocean processes. If the ocean is assumed to be in steady state, then its total energy has to be conserved and all incoming and outgoing energy fluxes have to balance each other.

To better distinguish between long and short term influences on the ocean energy budget, Lorenz (1955) introduces a decomposition of the kinetic and potential energy into a mean and an eddy-induced part. Lorenz's energy cycle contains the exchange between kinetic (MKE) and available potential (MPE) energy of the mean circulation and the kinetic (EKE) and available potential (EPE) energy of the eddy circulation. Therefore, Lorenz (1955) defined available potential energy as the difference between the total potential energy and a minimum potential energy that the system would have after an adiabatic rearrangement of all fluid particles (see Tailleux (2013) for an extension of APE to multi-component Boussinesq fluids with a non-linear equation of state). Apart from theses fluxes between the energy reservoirs, there might also be external sources of energy e.g. due to atmospheric forcing or sinks of energy due to dissipation.

Fig. 1.7 shows the Lorenz energy cycle diagnosed from a global eddy-permitting ($1/10^o$) numerical ocean model (Storch et al., 2012). Although the energy forcing due to surface fluxes of each individual energy reservoir is nearly balanced by a direct dissipative flux out of this reservoir, there are also energy fluxes between the individual energy reservoirs. The processes that can be associated with these exchanges are: barotropic instability for an exchange between MKE and EKE, baroclinic instability for an exchange between MPE and EPE and between EPE and EKE, and wind-driven upwelling for an exchange between MKE and MPE.

Atmospheric forcing predominantly acts on very large scales. Since kinetic energy dissipation can only occur at molecular scales, there has to be a downscale energy flux that connects the atmospheric large-scale energy input with the molecular small-scale energy sink. Fig. 1.8 shows a schematic of the paradigm how energy is redistributed between different scales by the turbulent dynamics. Following Charney (1971), geostrophic turbulence yields a downscale available potential and an upscale kinetic energy flux. Kinetic energy injected at large scales thus cannot reach the small scales directly and must either be dissipated at the large scales or transformed into available potential energy. Numerical simulations from Storch et al. (2012) suggest that 26% of the MKE surface flux is transformed to MPE, 6% to EKE and that 74% is dissipated as can be inferred from Fig. 1.7. Available potential energy is transported towards smaller scales until it reaches the scale of the first internal Rossby radius. At this scale baroclinic instability (Eady, 1949; Stone, 1966) transforms available potential energy into kinetic energy (fluxes between MPE and EPE and between EPE and EKE in Fig. 1.7). Since baroclinic instability is assumed to transform most of the available potential energy, the remaining downscale flux of available

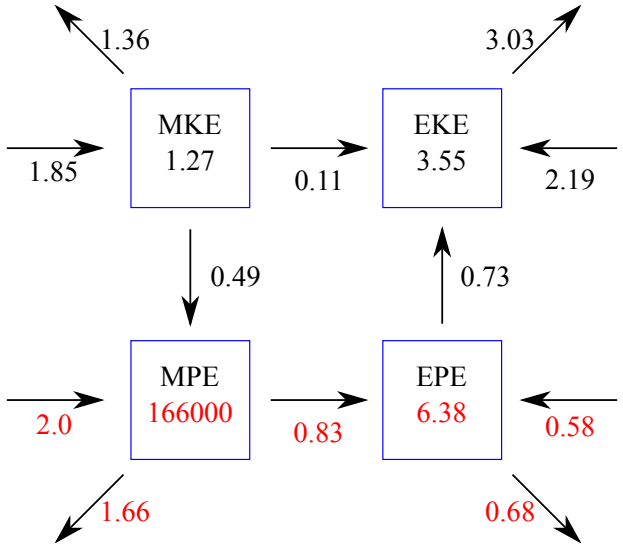

Figure 1.7: Lorenz energy cycle of a $1/10^o$ eddy permitting model forced by 6-hourly surface fluxes (Storch et al., 2012). The rectangles contain energy reservoirs for mean kinetic energy (MKE), eddy kinetic energy (EKE), mean potential energy (MPE) and available potential energy (APE) and numbers are given in 10^{18} J. Arrows between the reservoirs denote energy exchanges, horizontal ones pointing into the reservoirs denote the wind generated energy input for MKE and EKE and the generation of APE due to thermohaline surface fluxes for MPE and EPE. Diagonal arrows pointing out of the boxes denote energy sinks by dissipation. All energy fluxes are given in 10^{12} W. Note, that red numbers depend on the choice of a reference density profile that is chosen to be the global area average of the time mean density. Black numbers are independent of the reference density (adapted from Storch et al. (2012) and Olbers et al. (2012)).

potential energy to scales smaller than the Rossby radius has to be rather weak.

Following the theory of geostrophic turbulence, the kinetic energy induced by baroclinic instability has to be transported upscale again and the turbulent eddies would grow in size up to the basin scale and have to dissipate there. Since such basin-scale eddies are not found in the ocean, there has to be an eddy damping process that yields an energy dissipation on spatial scales between the Rossby radius and the basin scale. Some possible candidates might be lee wave generation (Bell, 1975; Nikurashin and Ferrari, 2011), loss of balance resulting from e.g. Lighthill radiation of gravity waves (Ford et al., 2000) or ageostrophic instabilities (Molemaker et al., 2005).

In addition, there might be an alternative route to dissipation due to the presence of ageostrophic processes. In fact, Capet et al. (2008c) and Molemaker et al. (2010) observe in different numerical model studies a downscale kinetic energy flux as soon as ageostrophic

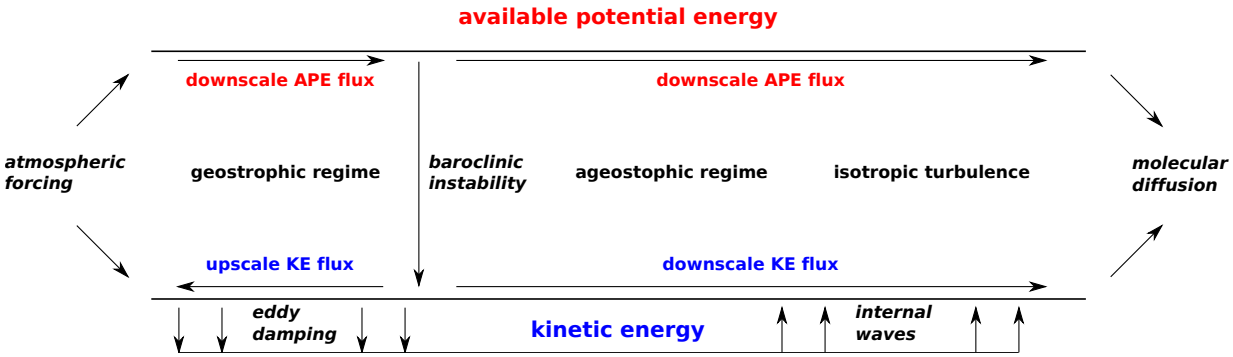

Figure 1.8: Schematic of the energy flux within the ocean. The length scale decreases from left to right and the upper part depicts the available potential energy APE and the lower part kinetic energy KE. Atmospheric forcing yields an energy source at the largest scales. APE is transported downscale until it reaches spatial scales comparable to the first baroclinic Rossby radius where baroclinic instability sets in and transforms APE into KE. Within the geostrophic regime, KE is subject to an inverse energy cascade that transports energy upscale towards the basin scale. Processes like e.g. lee wave generation, loss of balance resulting from Lighthill radiation or ageostrophic instabilities cause a damping of the eddies by exaggerating internal waves. In contrast, in regions where Ri is small (e.g. at the upper ocean), there might also be a downscale energy flux due ageostrophic effects that transports KE towards the smallest scales where it is dissipated by molecular processes. While the direction of the KE flux depends on whether ageostrophic processes are present, the APE flux is always downscale (see also Molemaker and McWilliams (2010) for a similar picture).

processes are present. In this case, energy is transported downscale until it enters the regime of isotropic turbulence. This regime is known to feature a downscale energy flux until the energy reaches the dissipation scale (Kolmogorov, 1941). It is not known so far, how important this ageostrophic route to dissipation is in comparison to the other possible dissipation mechanism.

Chapter 4, aims to obtain a detailed understanding of the downscale energy flux under ageostrophic conditions. As for Chapter 3, the ageostrophic processes investigated in Chapter 4 are predominantly due to stretching and tilting of relative vorticity (term V and VI in Eq. (1.1)). Although friction (term VII in Eq. (1.1)) plays an important role to dissipate energy, a damping is applied in the numerical model that only acts on the largest and smallest scales. It is assumed that the intermediate scales are not affected by friction or diffusion and that ageostrophic dynamics predominantly result from vortex stretching and tilting. In Chapter 4, numerical simulations are performed with varying dynamical conditions. This enables to investigate how the magnitude and direction of the energy flux

depends on the dynamical conditions and its ability to feature ageostrophic dynamics. The following specific question is addressed:

- How can a downscale energy flux and the resulting small-scale dissipation be related to the dynamical characteristics of a flow system?

1.5 Thesis Overview

As outlined in this chapter, this thesis aims at understanding the influence of ageostrophic dynamics on important aspects of the ocean circulation. Three different case studies form three research papers:

Chapter 2 consists of a research paper published in the *Journal of Physical Oceanography* (Brüggemann et al., 2011). It is entitled "A dynamically consistent closure for zonally averaged ocean models" and addresses the following specific research questions:

- Are zonally averaged ocean models that parameterize the zonally averaged meridional flow with the zonally averaged meridional pressure gradient dynamically inconsistent?
- If yes, how can geostrophic and ageostrophic dynamics be considered in order to obtain a dynamical consistent model of the zonally averaged meridional overturning circulation?

Chapter 3 consists of a research paper submitted to the *Journal of Physical Oceanography*. It is entitled "Validating different parameterizations for mixed layer eddy fluxes induced by baroclinic instability" and addresses the following specific research questions:

- What are the main differences between eddy flux parameterizations based on linear stability analysis and parameterizations based on scalings of the eddy potential energy release?
- How do parameterizations of mixed layer eddy fluxes perform under ageostrophic and geostrophic conditions?

Chapter 4 consists of a research paper that is in preparation to be submitted to the *Journal of Physical Oceanography*. It is entitled "Routes to dissipation under different dynamical conditions" and addresses the following specific research question:

- How can a downscale energy flux and the resulting small-scale dissipation be related to the dynamical characteristics of a flow system?

Chapter 5 provides a summary of the answers on these questions given within the three research papers. Furthermore an outlook is presented that discusses open or further questions arising from the investigation of each of the three case studies.

Chapter 2

A dynamically consistent closure for zonally averaged ocean models

This chapter is a reprint of the paper "A dynamically consistent closure for zonally averaged ocean models" published in the Journal of Physical Oceanography (©Copyright (November 2011) AMS)[1].

Citation: Brüggemann, Nils, Carsten Eden, Dirk Olbers, 2011: A dynamically consistent closure for zonally averaged ocean models. J. Phys. Oceanogr., 41, 2242-2258. doi: http://dx.doi.org/10.1175/JPO-D-11-021.1

Abstract

Simple idealized layered models and primitive equation models show that the meridional gradient of the zonally averaged pressure has no direct relation with the meridional flow. This demonstrates a contradiction in an often used parameterization in zonally averaged models. The failure of this parameterization reflects the inconsistency between the model of Stommel and Arons (1960) and the box-model of Stommel (1961), as previously pointed out by Straub (1996).

A new closure is proposed. The ocean is divided in two dynamically different regimes, a narrow western boundary layer and an interior ocean; zonally averaged quantities over these regions are considered. In the averaged equations three unknowns appear: The interior zonal pressure difference Δp_i, the zonal pressure difference Δp_b of the boundary layer, and the zonal velocity u_δ at the interface between the two regions. We parameterize Δp_i using a frictionless vorticity balance, Δp_b by the difference of the mean pressure in the interior and western boundary, and u_δ by the mean zonal velocity of the western boundary layer.

Zonally resolved models, a layer model and a primitive equation model, validate our parameterization by comparing with the respective zonally averaged counterparts. It turns out that the zonally averaged models reproduce well the buoyancy distribution and the meridional flow in the zonally resolved model versions with respect to the mean and time changes.

2.1 Introduction

It is a common assumption in physical oceanography, that the magnitude and sign of the zonally integrated meridional transport in the ocean, i.e. the meridional overturning circulation (MOC), is related to the meridional pressure or density gradient. This assumption originates in the discussion of a two-box model by Stommel (1961), in which the exchange flow between the two boxes is parameterized with the density difference between the boxes. The physical basis of this closure is a hypothetical dynamical balance between the pressure difference induced by the different densities of the boxes, and friction in a narrow pipe connecting the two parts of the ocean at depth.

A similar dynamical balance was also assumed by Marotzke et al. (1988) to close the momentum balance of the zonally averaged primitive equations. The Coriolis force is ignored, and a balance between the zonally averaged meridional pressure gradient and

some kind of interior friction (Marotzke et al. (1988) choose vertical friction) acting on the meridional velocity v is implemented in the meridional momentum balance, while momentum advection is assumed to be negligible. The last assumption is reasonable for scales larger than the internal Rossby radius. From this regime, a simple diagnostic relation

$$\bar{v} = -\gamma \partial_y \bar{p} \tag{2.1}$$

between the zonally averaged meridional transport $\bar{v}$ and the meridional gradient of the zonally averaged pressure $\bar{p}$ can readily be derived, where the positive parameter γ depends on the type for frictional parameterization (we will assume Rayleigh friction for simplicity but other forms are possible). Note that the wind stress forcing in Eq. (2.1) was ignored. It can be included in all closures discussed in the present study.

This relation for $\bar{v}$, together with the zonally averaged continuity equation to determine the vertical velocity $\bar{w}$, allows to calculate the zonally averaged tracer balances. Here zonal velocity/tracer correlations, which introduce standing-eddy contributions in the tracer balances, are ignored. Wright and Stocker (1991) diagnosed the relation between $-\partial_y \bar{p}$ and $\bar{v}$ in a zonally resolved general circulation model and found indeed a positive value for the constant γ, which, however, depends on latitude. However, their particular choice of this relation is void of any dynamical fundament. Wright et al. (1998) give dynamical arguments to motivate a modified version of the closure, which leads to a relation very similar to Eq. (2.1) (see Sec. 2.5 for details).

It is one purpose of this study to demonstrate that the closure Eq. (2.1) is physically inconsistent. Although this point was already discussed by Straub (1996) and Greatbatch and Lu (2003), it was apparently not well received by the scientific community: there are currently several coupled Earth system models of intermediate complexity with zonally averaged ocean model components relying on the closure given by Eq. (2.1) (Claussen et al., 2002). Because of their low computational costs, such models are often used for paleo climate simulations and long-term climate projections – several of them are included in the Fourth Assessment Report of the IPCC (Solomon et al., 2007). Ocean only versions are used e.g. for studies discussing the stability of the thermohaline circulation (e.g. Alexander and Monahan (2009)). Furthermore, scalings for the global meridional circulation including the Southern Ocean and its impact on the circulation in zonally bounded basins still rely on Eq. (2.1) (Gnanadesikan, 1999; Levermann and Fürst, 2010). We would like to point out that the closure by Wright et al. (1995) is an exception, it does not rely on Eq. (2.1) as we will discuss in the Sec. 2.6.

It is evident that the closures by Marotzke et al. (1988), Wright and Stocker (1991) and Wright et al. (1998) have in common that they call for a "downgradient" form of the meridional transport similar to what was assumed by Stommel (1961) for the viscous pipe flow in his two-box model, leading to a local relation between $\bar{v}$ and $\partial_y \bar{p}$. It was argued by Straub (1996) that this assumption is inconsistent with the model by Stommel and Arons (1960), describing the flow in a two-layer system. In that model, the zonal mean of the interface height between the layers, equivalent to the pressure in primitive equations, becomes independent of the location of the deepwater sources, i.e. independent of the sign and magnitude of the meridional transports, thus proving the closures based on Eq. (2.1) to be wrong. We call this contradiction between the two models by Stommel and Arons (1960) and Stommel (1961) "Straub's dilemma" and further detail this point in the following section.

The models by Stommel (1961) and Stommel and Arons (1960) have different conceptual backgrounds and were developed to focus on different aspects of ocean dynamics. Therefore it cannot be a priori expected that both models are consistent with each other. Evidently, both models had success in describing important phenomena of the ocean dynamics. However, applying the strongly simplified assumptions of the Stommel (1961) model to zonally averaged models of Marotzke et al. (1988), Wright and Stocker (1991) and Wright et al. (1998), "Straub's dilemma" cannot be ignored any more because it reveals dynamical inconsistencies of these models.

The central purpose of the present study, however, is to present and validate an alternative closure for zonally averaged models, which generalizes the concept of Wright et al. (1995). Their closure is based on a meridional integration of the vorticity balance in the interior and in the western boundary layer. In their closure the need of an integration constant emerges which is difficult to determine but which sets the size and sign of the meridional transports. We also divide the ocean into an interior and a western boundary current but instead of averaging the vorticity equation over these regions we work with the momentum and buoyancy (layer thickness) equations directly. This way we avoid the determination of an integration constant but need instead parameterizations for the interior pressure difference, for the pressure difference of the boundary layer and the zonal velocity at the interface between these regions. A detailed comparison of two types of circulation models (a two-layer model, referred to as LM, like the one by Stommel and Arons (1960) and a general primitive equation model, referred to as PEM, with many levels) with their zonally averaged counterparts demonstrates the feasibility of the closure.

2.2 Straub's dilemma

2.2.1 Dilemma in a simple layered model

We first consider the model by Stommel and Arons (1960) in a slightly extended form also used by Greatbatch and Lu (2003) which is further referred to as layer model or LM. The governing equations for this model are given by

$$\partial_t u - fv = -g'\partial_x h - r\,u \tag{2.2}$$

$$\partial_t v + fu = -g'\partial_y h - r\,v \tag{2.3}$$

$$\partial_t h + H(\partial_x u + \partial_y v) = Q - \lambda h \tag{2.4}$$

where H denotes the mean thickness of the lower layer of a two-layer ocean and its perturbation h, with a density difference $\delta\rho$, between the two layers represented by the reduced gravity $g' = g\delta\rho/\rho_0$. The velocities u and v are the differences between the upper and lower layer velocities. A prescribed deepwater source is denoted by Q and the interior upwelling is parameterized by the term $-\lambda h$ in the thickness balance Eq. (2.4). The momentum balance Eq. (2.2) and Eq. (2.3) is taken linear, friction induced by sub-grid-scale processes is represented by Rayleigh friction with coefficient r. For a detailed derivation of the model equations see e.g. Gill (1982), section 6.2, or Greatbatch and Lu (2003). There are two equations derived from Eq. (2.2) to Eq. (2.4) which we present for later use. The momentum balance yields the vorticity balance

$$(\partial_t + r)(\partial_x v - \partial_y u) = -f(\partial_x u + \partial_y v) - \beta v \tag{2.5}$$

and using this equation to eliminate the divergence from the thickness balance we find

$$(\partial_t + \lambda)h - (H/f)(\partial_t + r)(\partial_x v - \partial_y u) - (H\beta/f)v = Q \tag{2.6}$$

which is the potential vorticity balance. Implementing the geostrophic approximation of Eq. (2.2) and Eq. (2.3) to eliminated u and v, turns this into the familiar form of the quasi-geostrophic vorticity equation

$$\partial_t(\nabla^2 h - h/R^2) + \beta\partial_x h + r\nabla^2 h - (\lambda/R^2)h = -Q/R^2 \tag{2.7}$$

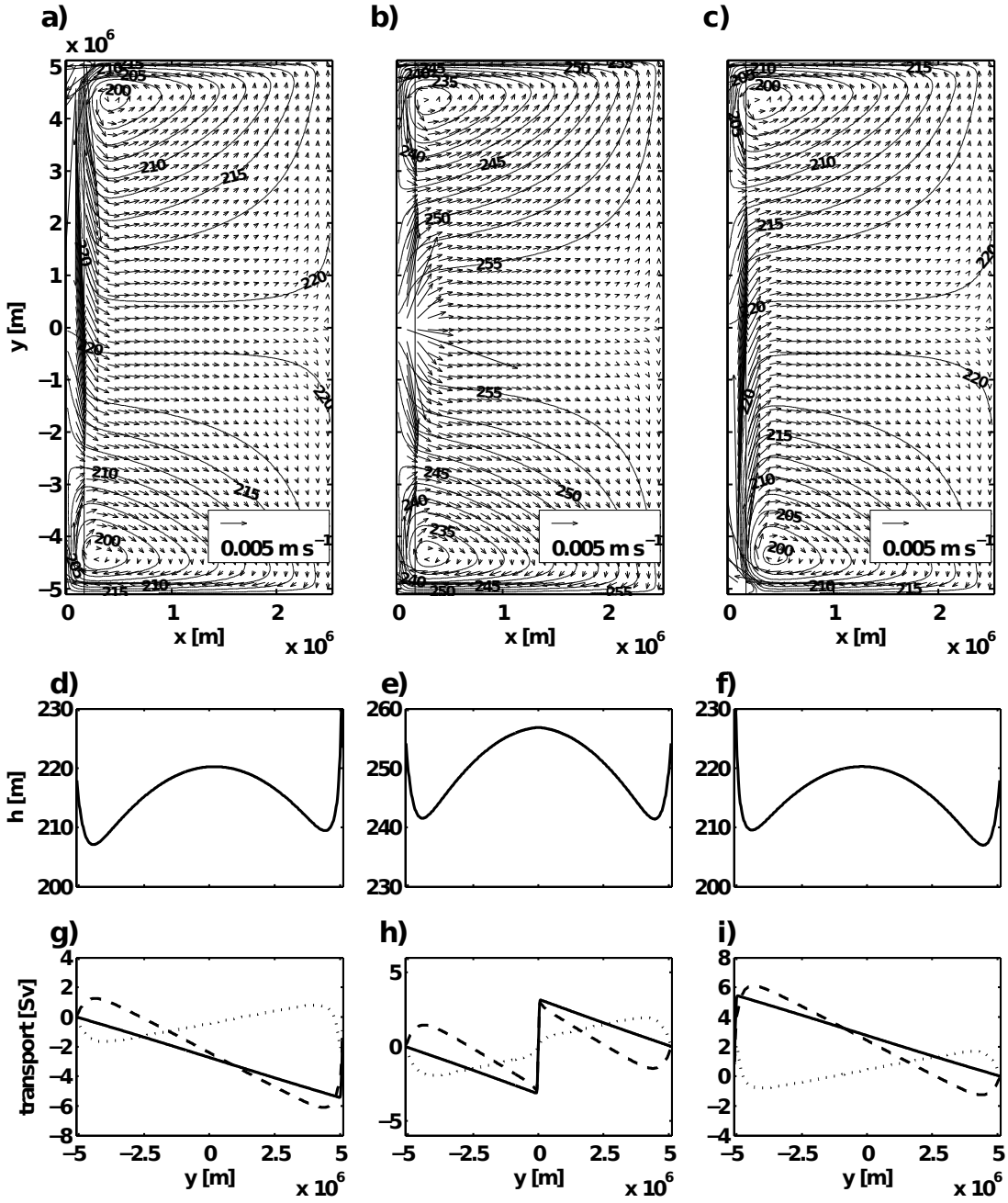

Figure 2.1: Numerical simulation of LM after 160 years of integration. (a) Layer thickness h in m (contours) and velocity (arrows) in $\mathrm{m\,s^{-1}}$ with deepwater source Q localized in the north-western corner. (b) Same as (a) but with deepwater source Q located at the equator $y = 0$ on the western side. (c) Same as (a) but with Q at the south-western corner. (d) Zonally averaged layer thickness $\bar{h}$ in m for the experiment shown in (a). (e) Same as (d) but for the equatorial source. (f) Same as (e) but for the southern source. (g) Total meridional transport in Sv (solid), transport in the western boundary layer (dashed) and transport in the interior (dotted) for the experiment shown in (a). (h) Same as (g), but for the equatorial source. (i) Same as (g), but for the southern source.

where $R = c/|f|$ is the baroclinic Rossby radius and $c = \sqrt{Hg'}$ the Kelvin wave speed. The equation determines the long-term adjustment of the circulation by Rossby waves. It also determines the steady state.

The potential vorticity equation reveals the existence of a western boundary layer of the Stommel type with the familiar width $\delta_W = r/\beta$, resulting from the dominant balance between advection of planetary vorticity and the torque by the Rayleigh friction, $\beta v = -r\partial_x v$ or $\beta\partial_x h = -r\partial_{xx} h$. In the interior the planetary term $\beta\partial_x h$ and the upwelling term $-\lambda h/R^2$ dominate. Approaching the northern (or southern) rim of the domain, with $h \to const, v \to 0$ and $Q \equiv 0$, upwelling and the Rayleigh friction term $r\partial_{yy} h$ must balance in the steady state. This implies a meridional scale, $\delta_{NS} = R\sqrt{(\delta h/h)r/\lambda}$ where $\delta h/h$ the relative variation of h. These consideration can be used to construct an approximate analytical solution of Eq. (2.7). Here, however, a numerical model will be used.

For the experiments with LM we have used the parameter values $r = 2 \times 10^{-6}\,\mathrm{s}^{-1}$, $\lambda = 1 \times 10^{-9}\,\mathrm{s}^{-1}$, $g' = 0.02\,\mathrm{m\,s}^{-2}, \beta = 2.3 \times 10^{-11}\,\mathrm{m}^{-1}\,\mathrm{s}^{-1}$ and $H = 400\,\mathrm{m}$ which yields $c = 2.8\,\mathrm{m\,s}^{-1}$, $R = 30\,\mathrm{km}$ (at $y = 4000\,\mathrm{km}$), $\delta_W = 100\,\mathrm{km}$ and $\delta_{NS} = 300\,\mathrm{km}$. For the latter $\delta h/h \sim 0.1$ is used. The system is integrated on an equatorial β-plane and the horizontal resolution is 20 km in the zonal and meridional directions. The zonal and meridional extend of the model domain is 2500 km and 10 000 km, respectively. To demonstrate the influence of the transport and pressure field on the location of the deepwater source, we choose three different locations for Q. The results of the three experiments are shown in Fig. 2.1. The location of the deep-water source is at the north western edge of the model domain for Fig. 2.1a, at the equator at the western boundary for Fig. 2.1b, and at the south western edge of the model domain for Fig. 2.1c. The lateral scale of Q is δ_W in both directions. In each experiment two dynamical different regimes exist: a narrow western boundary layer with a strong meridional flow, and a weak interior flow whose meridional component is always poleward. The widths of the boundary layers at the western, northern and southern rims confirm the above considerations.

In the interior the velocity field and the thickness contours are almost identical in all three cases. This is because the Sverdrup balance

$$\beta v = (f/H)\lambda h \tag{2.8}$$

obtained from Eq. (2.6) holds to a good approximation for steady conditions and $r/(\beta B) \ll 1$, where B is the zonal width of the basin. We also need to know that h is related to Q

only in an integral sense, i.e.

$$\lambda \int h dx dy = \int Q dx dy \tag{2.9}$$

in the integral over the whole model domain; however, the rhs of Eq. (2.9) has only contributions from the western boundary region. From Eq. (2.8) it is clear that the meridional interior transport is driven by the interior upwelling λh which is almost identical for the three cases, i.e. almost uniform and of similar magnitude. The major differences occur therefore only in the boundary current of the individual experiments which has to balance the interior flow and the upwelling in the interior and the different inflows of the localized deepwater source Q.

It is clear that the location and strength of the deepwater source Q in the thickness equation determines the total transport in the lower layer, i.e. when Q is located at the northern-western corner, the total meridional transport is southward in both hemispheres of the domain, Fig. 2.1g (solid line), and it is anywhere northward for a deepwater source Q located at the south-western corner of the domain, Fig. 2.1i, while the total transport is polewards in both hemispheres for an equatorial source, Fig. 2.1h. The source Q drives a total transport of about 5 Sv in the vicinity of the source in each case, which linearly reduces due to the interior upwelling into the upper layer with increasing distance from the source. Although the western boundary layer is much smaller than the total width of the basin, the transport in the western boundary layer is of similar magnitude as the total transport. It also has the same direction as the total transport, except for the region $y < -2500\,\mathrm{km}$, $|y| > 2500\,\mathrm{km}$ and $y > 2500\,\mathrm{km}$ for the experiment with northern, equatorial and southern source, respectively, where it opposes the total transport.

Since the zonal integral of h is dominated by the interior, the zonally integrated h becomes independent of the location of the deepwater source Q. Consequently, h and in particular the meridional gradient of h become independent of the location of Q, and thus the sign and strength of the meridional transport is neither related to the zonal average of h nor its meridional gradient. This statement is in contrast to the box model by Stommel (1961) where the flow between the two boxes is parameterized by the meridional density difference between the boxes, and also in contrast to the closures by Marotzke et al. (1988), Wright and Stocker (1991) and Wright et al. (1998) which all depend on Eq. (2.1). To summarize, the parameterization in the box model by Stommel (1961) and the closures based on Eq. (2.1) are not consistent with the dynamics of the model by Stommel and

Arons (1960). This inconsistency, "Straub's dilemma", was first noted by Straub (1996).

2.2.2 The dilemma in primitive equations

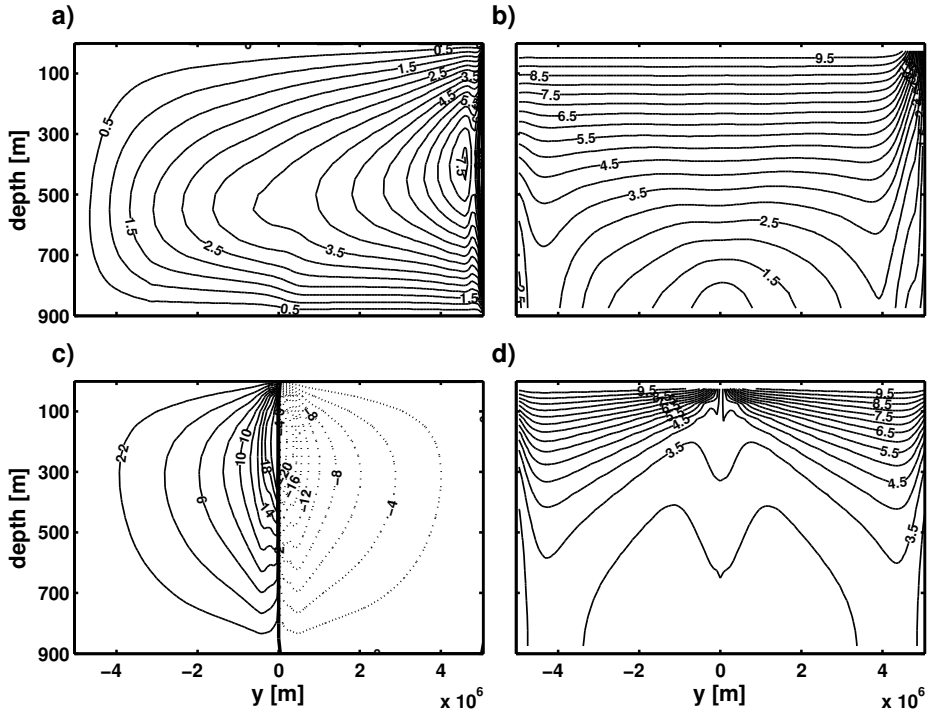

Figure 2.2: The upper row displays in (a) the meridional overturning streamfunction ψ (contour interval is 0.5 Sv) and in (b) the zonally averaged temperature (contour interval is 0.5^oC) of PEM with a deepwater formation region at the northern boundary. The meridional overturning streamfunction (contour interval is 2 Sv) and zonally averaged temperature (contour interval is 0.5^oC) for an equatorial deepwater formation region is shown in (c) and (d), respectively. The results are time averages over the last 100 years of a 200 years integration.

The independence of the meridional gradient of the zonally averaged thickness from the meridional transport is not specific to layered models but is also found in a primitive equation model (Viebahn and Eden (2010); `http://www.ifm.zmaw.de/mitarbeiter/prof-dr-carsten-eden/numerical-models/`), referred to as PEM, with a similar configuration as the layered model (LM). In PEM we have neglected momentum advection (as before), and, for simplicity, the only tracer is temperature. The model domain is identical to the layered model, but there are 20 vertical levels of 50 m thickness, such that the do-

main is 1000 m deep. PEM is forced by relaxation of temperature in the uppermost grid box towards a target temperature, which is zonally and meridionally uniform except for a small region of meridional width r/β (equivalent to the western boundary layer width) at the northern or equatorial region with a 3 K smaller target temperature. This way a northern or equatorial deepwater formation region is introduced as in the layered model. A case with southern source is just a mirror of the one with northern source and therefore not further discussed. The time scale of relaxation at the surface is 20 days. Convection in case of unstable stratification is parameterized by setting the vertical diffusivity to very large values. As in LM, there is no wind forcing, i.e. we focus here on the thermohaline circulation. Friction is identical to the LM, except that we introduce in addition lateral and vertical friction with viscosities of $3.2 \times 10^4\,\mathrm{m^2\,s^{-1}}$ and $1 \times 10^{-3}\,\mathrm{m^2\,s^{-1}}$, respectively, since otherwise unphysical oscillations on a short time scale develop. We use the Quicker advection scheme (Leonard, 1979) for tracers and vertical diffusivity of $1 \times 10^{-4}\,\mathrm{m^2\,s^{-1}}$ in addition.

The steady solution of PEM, shown in Fig. 2.2, indeed has much resemblance to LM. In the experiment with a northern source, there is a deep temperature minimum at the equator and isopycnals below about 500 m depth are symmetric with respect to the equator, bending towards the bottom and towards the poles (Fig. 2.2b). A similar "hill", symmetric around the equator, can be seen in the experiment with the equatorial source (Fig. 2.2d), although it is located more to the surface than at depth. Fig. 2.2 a and 2.2c also show the meridional transports for both experiments with PEM by the meridional streamfunction ψ with $\bar{v} = -\partial_z \psi$. The surface forcing drives a volume transport of a couple of Sv in both cases. In case of the northern source, there is southward flow at depth, almost uniform upwelling in the interior and northward return flow at the surface. Sign, magnitude and meridionally structure of the meridional transport is also very similar to LM in the experiment with equatorial source (see Fig. 2.2c and 2.2d).

As for LM, the meridional gradient of the zonally averaged density (i.e. temperature) or pressure (not shown) is similar in both experiments with PEM (compare Fig. 2.1d with Fig. 2.2b and Fig. 2.1e with Fig. 2.2d for the case with northern and equatorial deep water source, respectively) and is of opposite sign in both hemispheres. Their depth dependence differs. The meridional transport, on the other hand, does not show any direct dependency on $\partial_y \bar{p}$, with respect to the individual hemispheres or experiments, proving the downgradient closures based on Eq. (2.1) to be wrong in primitive equation models as well. The reason is of course the same as in LM, notably the zonally averaged pressure $\bar{p}$

is dominated by the interior zonal mean of p, which is in turn governed by the frictionless Sverdrup relation in the interior.

Greatbatch and Lu (2003) increased the vertical mixing to unrealistic values in LM and found that the zonally averaged thickness $\bar{h}$ becomes dominated by the values in the western boundary layer, such that $\bar{h}$ resembles more and more the meridional transports. We note here that introducing meso-scale eddy mixing results in a similar effect. However, again unrealistically large values of the isopycnal thickness diffusivity are needed.

2.3 A consistent closure

We regard the closure for a zonally averaged model proposed by Wright et al. (1995) as dynamically consistent. It is based on a meridionally integrated, zonally averaged balance of vorticity (see Sec. 2.6). However, integrating the vorticity balance requires integration constants to be specified in each hemisphere. Wright et al. (1995) locate these constants at the northern and southern boundary of the domain and relate them to the interior flow at the respective boundaries. The result is a non-local relation between the zonally averaged pressure $\bar{p}$ (or thickness $\bar{h}$) and the average meridional flow, as detailed in Eq. (2.45) of the Appendix. We have shown that the interior flow, and thus $\bar{p}$ (or $\bar{h}$), are nearly independent of the deepwater convection region and the direction and magnitude of the MOC. Since the choice of the integration constant determines the direction and magnitude of the MOC, it appears therefore problematic to use the interior flow for the choice. We therefore propose and evaluate a closure for zonally averaged models which avoids unknown integration constants. The closure is developed for the shallow water and the primitive equations.

2.3.1 Closure for the layer model

Instead of considering the vorticity balance in the interior and the western boundary layer we simply use separate thickness and momentum balances averaged over these domains and keep also all time derivatives. Zonal averages of variables over the whole basin are indicated with overbars without an index, zonal averages over the boundary layer or the interior carry an additional index b or i, respectively. The total meridional transport can be obtained by

$$B\bar{v} \;=\; B_b\bar{v}_b + B_i\bar{v}_i \tag{2.10}$$

and the zonally averaged height by

$$B\bar{h} = B_b\bar{h}_b + B_i\bar{h}_i \tag{2.11}$$

Here B, B_b and B_i denote the total basin width from the western to the eastern boundary, the width of the western boundary layer and the width of the interior, respectively. Note that the boundary layer width might be defined as a multiple of r/β. Obviously, $B_b \ll B_i$.

Motivation and evaluation of the closure

Averaging the system Eq. (2.2) to Eq. (2.4) over the western boundary at x_W to the offshore edge of the western boundary layer at x_δ yields

$$\begin{aligned}
\partial_t\bar{u}_b - f\bar{v}_b &= -g'\Delta h_b/B_b - r\bar{u}_b && (2.12)\\
\partial_t\bar{v}_b + f\bar{u}_b &= -g'\partial_y\bar{h}_b - r\bar{v}_b && (2.13)\\
\partial_t\bar{h}_b + H(\partial_y\bar{v}_b + u_\delta/B_b) &= \bar{Q}B/B_b - \lambda\bar{h}_b. && (2.14)
\end{aligned}$$

with $\Delta h_b = h(x = x_\delta) - h(x = x_W) = h_\delta - h_W$. In the thickness balance the zonal velocity $u_\delta = u(x = x_\delta)$ at the interface between the interior and the boundary layer appears. Furthermore, it was assumed in Eq. (2.14) that $u(x = x_W) = 0$ and the source Q was located entirely in the western boundary layer. Likewise the respectively averaged equations for the interior regime, extending from x_δ to x_E, are

$$\begin{aligned}
\partial_t\bar{u}_i - f\bar{v}_i &= -g'\Delta h_i/B_i - r\bar{u}_i && (2.15)\\
\partial_t\bar{v}_i + f\bar{u}_i &= -g'\partial_y\bar{h}_i - r\bar{v}_i && (2.16)\\
\partial_t\bar{h}_i + H(\partial_y\bar{v}_i - u_\delta/B_i) &= -\lambda\bar{h}_i. && (2.17)
\end{aligned}$$

with $\Delta h_i = h(x = x_E) - h(x = x_\delta) = h_E - h_\delta$. Here $u(x = x_E) = 0$ is used. To allow for the northern and southern boundary layers, described in section 2.2.1, the friction terms have been retained though they are negligible in the actual interior. The pressure differences over the respective domains, Δh_b and Δh_i, as well as the zonal velocity u_δ have to be parameterized. The resulting model will be referred to as ZALM (zonally averaged layer model).

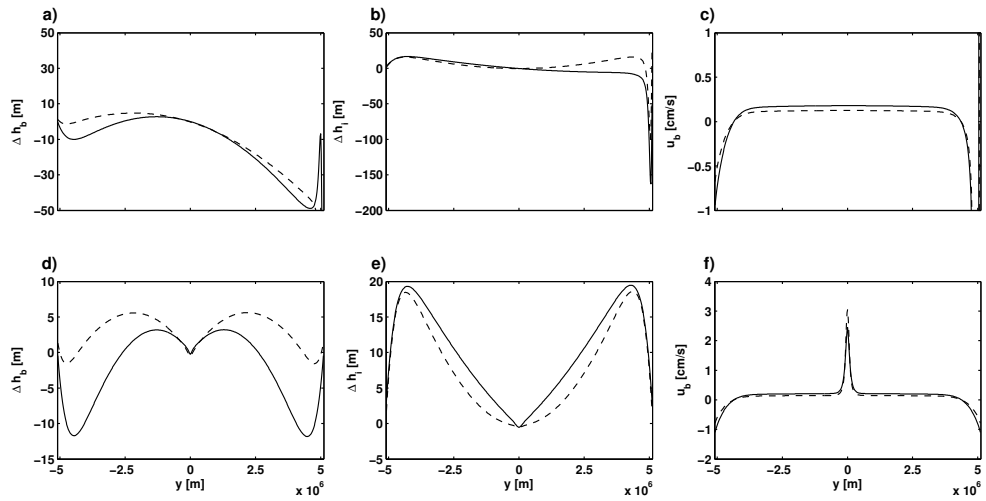

Figure 2.3: (a) Thickness difference (in m) over the western boundary layer Δh_b (solid) and its parameterization Eq. (2.23) (dashed) as function of y for the experiment with northern source. (b) Same for Δh_i and its parameterization Eq. (2.21). (c) Zonal velocity at the offshore edge of the boundary layer u_δ (solid) and its parameterization Eq. (2.18) (dashed). All tuning coefficients are set to one. Lower row (d), (e), and (f) Same but for experiments with equatorial source.

We start by assuming that u_δ must be close to $\bar{u}_b$, hence we put[2]

$$u_\delta \stackrel{!}{=} \gamma_1 \bar{u}_b \tag{2.18}$$

in the thickness balances Eq. (2.14) and Eq. (2.17). Note that a linear increase of u within the western boundary layer would yield $\gamma_1 = 2$. However, u is not increasing linearly over the western boundary layer (not shown) and we found that the best fit is obtained for $\gamma_1 = 1.7$ (see also Fig. 2.3c and Fig. 2.3f where l.h.s and r.h.s. of Eq. (2.18) are shown). Next we demand that the thickness balance for the interior regime yields the averaged form of the Sverdrup balance Eq. (2.8), assuming steady state and vanishing friction. To insert $\bar{v}_i$ from the momentum balance Eq. (2.15) into the thickness balance Eq. (2.17) we compute the meridional divergence of $\bar{v}_i$ from the zonal momentum balance Eq. (2.15), which becomes

$$f\partial_y \bar{v}_i = (g'/B_i)\partial_y \Delta h_i - \beta \bar{v}_i + r\partial_y \bar{u}_i + \partial_t \partial_y \bar{u}_i \tag{2.19}$$

[2]In this paper we denote by the "$\stackrel{!}{=}$"-sign that we introduce a parameterization.

We note that the choice

$$g'\partial_y \Delta h_i \stackrel{!}{=} f u_\delta \tag{2.20}$$

leads to an interior thickness budget in which only the βv-contribution, frictional and tendency terms remain, i.e. to an interior Sverdrup balance analogous to Eq. (2.8) (assuming that βv dominates $r\partial_y \bar{u}_i$ and $\partial_t \partial_y \bar{u}_i$ in Eq. (2.19)). Using Eq. (2.20) together with Eq. (2.18) as parameterization of Δh_i, the integrated form this relation reads

$$g'\Delta h_i \;\; = \;\; g'(\Delta h_i)|_{y=0} + \gamma_1 \int_0^y f \bar{u}_b dy' \tag{2.21}$$

The integration constant at $y = 0$ follows from the steady state zonal balance at the equator,

$$g'(\Delta h_i)|_{y=0} \stackrel{!}{=} -rB_i \bar{u}_i(y=0) \tag{2.22}$$

Note that the Rayleigh model has the deficit that the equatorial field $\bar{u}_i(y = 0)$ is completely decoupled from the rest. For this reason $\bar{u}_i(y = 0)$ in Eq. (2.22) is replaced by the mean over three grid points across the equator. Note that the l.h.s and r.h.s. of Eq. (2.21) are shown in Fig. 2.3b and Fig. 2.3e.

It remains to specify a parameterization for the pressure difference $\Delta h_b = h_\delta - h_W$ across the boundary layer. We have experimented with a variety of closures for Δh_b analogous to Eq. (2.20), i.e. motivated by the potential vorticity budget in the western boundary layer. However, many possible forms for the closure, which often yield an excellent fit to the respective variable in the zonally resolved model, turned out to lead to unstable numerical integrations. The simple ansatz

$$\Delta h_b \stackrel{!}{=} \gamma_2(\bar{h}_i - \bar{h}_b) \tag{2.23}$$

with another tuning parameter γ_2 of order one, on the other hand, yields stable integrations in all cases which we have considered, and also a reasonable fit to Δh_b from the zonally resolved model as discussed next (l.h.s and r.h.s. of Eq. (2.23) are shown in Fig. 2.3a and Fig. 2.3d). Further, the results of the integrations with the resulting zonally averaged model compare well with the zonally resolved counterparts, as discussed below, giving confidence to the parameterization Eq. (2.23).

Fig. 2.3 shows the western boundary thickness difference Δh_b and its parameterization $\bar{h}_i - \bar{h}_b$, both diagnosed from the experiments with the layered model LM, shown in Fig. 2.1. For the experiment with northern (southern) source, the parameterization fits well Δh_b except for the southernmost (northernmost) part of the domain in the experiment with northern (southern) source, where Δh_b becomes negative, while $\bar{h}_i - \bar{h}_b$ stays positive. A similar deviation in the sign of the parameterization can be seen in the experiment with the equatorial source for large distances from the source. However, the structure of the meridional changes in $\bar{h}_i - \bar{h}_b$ are in all cases similar to Δh_b. We also note that the quality of the parameterization depends on the exact definition of the width of the western boundary layer. Here, we have used $B_b = r/\beta$ with values for r and β as in the numerical experiments. The middle panels of Fig. 2.3 displays Δh_i from the zonally resolved model and its parameterization Eq. (2.21) which in fact agree very well. Fig. 2.3 also shows the outflow from the western boundary region, u_δ, from the zonally resolved model together with its parameterization $\bar{u}_b$. Our choice Eq. (2.18) fits u_δ well with respect to the meridional structure and sign, while the magnitude is underestimated, which might be resolved by tuning the parameter γ_1 to values greater than one.

Performance of the zonally averaged layer model

The complete ZALM consists of Eq. (2.12) to Eq. (2.14) for the boundary layer and Eq. (2.15) to Eq. (2.17) for the interior domain together with the parameterizations expressed in Eq. (2.18), Eq. (2.21) and Eq. (2.23). ZALM was programmed in Fortran 90 and the source code together with a detailed documentation of all numerical details can be downloaded from `http://www.ifm.zmaw.de/mitarbeiter/prof-dr-carsten-eden/numerical-models/`. The steady state of a numerical integration of ZALM is shown as dashed lines in Fig. 2.4 and compared with the correspondingly averaged quantities diagnosed from LM. Note that the configuration of ZALM is identical to LM in all respects (excepts for the zonal extent and the closure). Transports and thickness height are reasonably well reproduced by ZALM for the northern and equatorial sinking case using $\gamma_1 = \gamma_2 = 1$ and a boundary layer width of $B_b = r/\beta$. However, by changing the tuning parameters to $\gamma_1 = 1.7$, $\gamma_2 = 1.2$ and $B_b = 2r/\beta$, the broad central "hill' in $\bar{h}$ and the structure at the northern and southern boundaries are even better reproduced (dotted lines in Fig. 2.4). This improvement was found after some educated trials. Probably an even better improvement could be reached by using a parameter optimization procedure but this is not focus of this study.

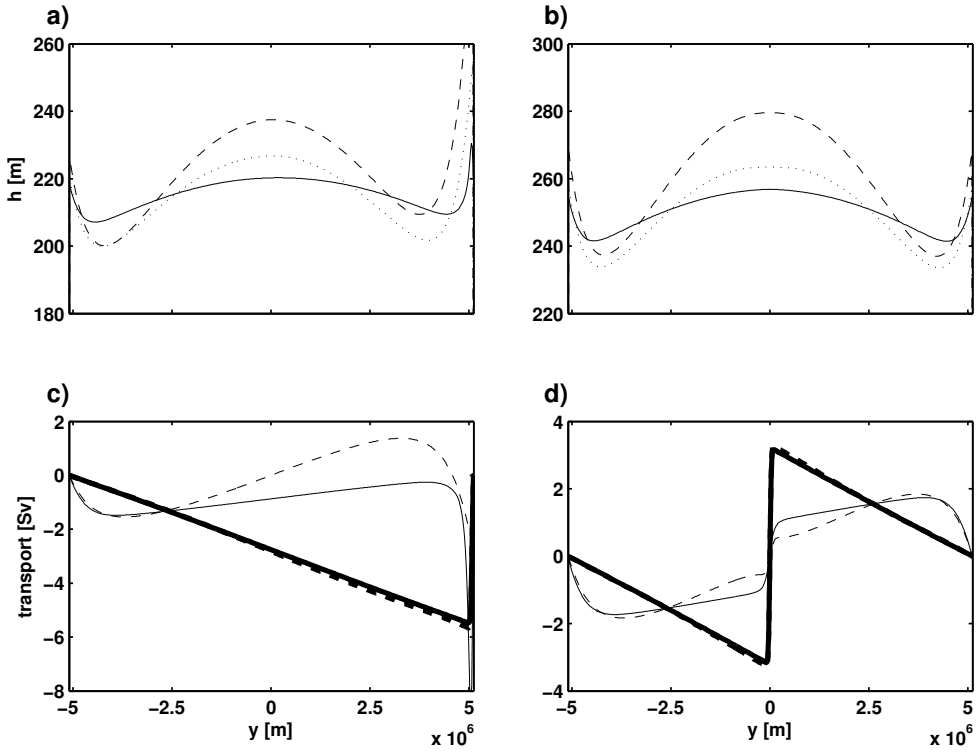

Figure 2.4: Comparison of results of LM and ZALM for the experiment with northern source in (a) and (c) and for the experiment with equatorial source in (b) and (d). Shown is the zonally averaged layer thickness $\bar{h}$ in m (a) and (b) and meridional transports $B\bar{v}$ in Sv (c) and (d). In (a) and (b) solid lines denote the results of LM , the dashed lines the results of ZALM with $\gamma_1 = \gamma_2 = 1$ and $B_b = r/\beta$ and the dotted lines the results of ZALM with $\gamma_1 = 1.7$, $\gamma_2 = 1.2$ and $B_b = 2r/\beta$. In (c) and (d) the thick lines are total transports ($B\bar{v}$) of LM (solid) and ZALM (dashed) and the thin lines are interior transports ($B_i\bar{v}_i$) of LM (solid) and ZALM (dashed). In (c) and (d) the result of ZALM with $\gamma_1 = \gamma_2 = 1$ and $B_b = r/\beta$ are shown; the results with the tuned parameter set look similar.

We take next a closer look at the physical processes which establish the circulation in ZALM. Kawase (1987) showed that the establishment of the deepwater circulation involves basin-wide propagating Kelvin and Rossby waves: A thickness anomaly generated at the northern boundary of the basin propagates along the western boundary southward in form of a Kelvin wave; at the equator, the Kelvin wave turns into an equatorial Kelvin wave and crosses the basin towards the east where it is again reflected and propagates at the eastern boundary north- and southward; westward propagating long Rossby waves, emanating from the eastern boundary, then transfer the signal into the interior of the ocean. These processes are of course realized in LM and a very similar adjustment process can be found in ZALM.

It is easily confirmed that the dynamics in the western boundary layer of ZALM allow for a Kelvin wave. With $\bar{u}_b \equiv 0$ and vanishing friction, diffusion and forcing, the equations become

$$\partial_t \bar{v}_b + g' \partial_y \bar{h}_b = 0 \qquad \partial_t \bar{h}_b + H \partial_y \bar{v}_b = 0 \tag{2.24}$$

which yields the familiar wave speed $c = \sqrt{g'H}$. The zonal velocity is in geostrophic balance. In a corresponding way, Kelvin waves exist for the interior regime of ZALM, which are, however, attached to the eastern boundary in the zonally resolved model . Both regimes also support meridionally propagating gravity waves which are coupled via the pressure terms and the u_δ-term in the thickness balances.

Because of the zonal averaging, equatorial waves and midlatitude Rossby waves appear in a quite hidden way in ZALM. The Rossby wave response in midlatitudes is governed by the potential vorticity equations for the boundary and interior regime derived from Eq. (2.12) to Eq. (2.14) and Eq. (2.15) to Eq. (2.17) together with the parameterizations expressed in Eq. (2.18), Eq. (2.21) and Eq. (2.23). We find, omitting again friction, diffusion and forcing

$$\partial_t(\bar{h}_i - R^2 \partial_{yy} \bar{h}_i) + (\beta R^2 / B_i) \bar{h}_b = 0 \tag{2.25}$$

$$\partial_t(\bar{h}_b - R^2 \partial_{yy} \bar{h}_b) - (f R^2 / B_b) \partial_y (\bar{h}_b - \bar{h}_i) - (\beta R^2 / B_b) \bar{h}_i = 0 \tag{2.26}$$

with the Rossby radius $R = \sqrt{g'H/f^2}$. Here all tuning parameters of the parameterizations are set to one. Note that $\tau_\alpha = B_\alpha/(\beta R^2)$ is the time that a baroclinic Rossby wave needs to cross the respective region $\alpha = i, b$. The corresponding time scale for the interior is roughly 10 years in the northern part; it decreases towards the equator to several days (7 days at $y = 300\,\mathrm{km}$). For the boundary layer, the time scale is considerably smaller (by the factor $B_b/B_i \simeq 25$). The Rossby wave communication between the two regimes is thus represented by an oscillation of the mean layer thicknesses $\bar{h}_i$ and $\bar{h}_b$ with a period proportional to $\sqrt{\tau_i \tau_b}$. In addition there is a meridional propagation of the perturbation with the correct Rossby wave speed, expressed by the meridional derivative terms in the tendency terms.

To assess the temporal behavior, Fig. 2.5 shows $\bar{h}_b$ and $\bar{h}_i$ for ZALM in comparison to LM from the start of both integrations. In the initial phase of both simulations the anomaly in the interface height produced by the deepwater source is distributed via a Kelvin wave propagating from the northern edge of the model domain along the western boundary

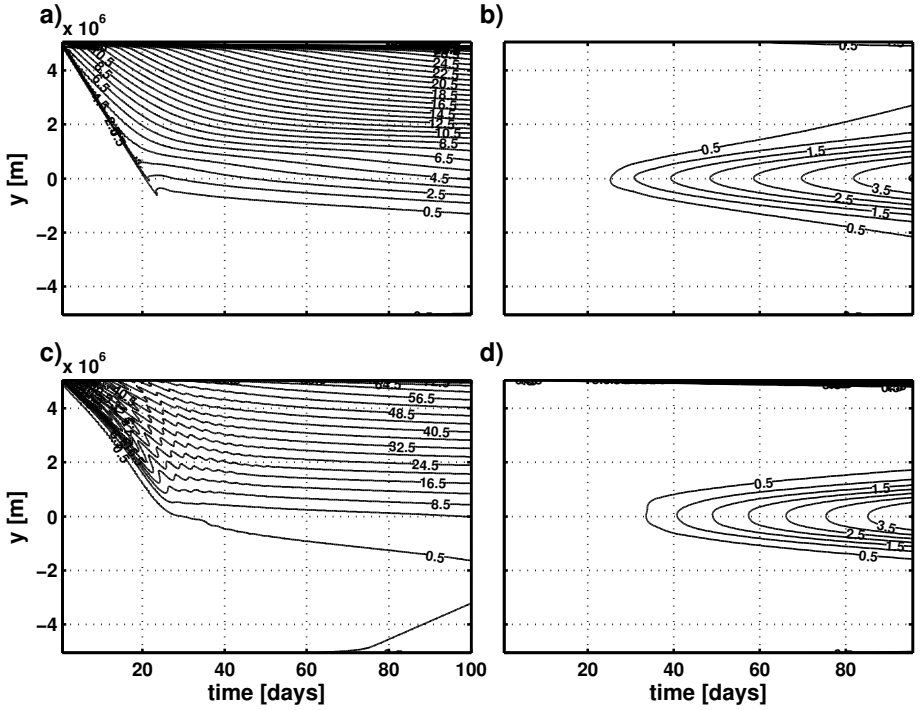

Figure 2.5: Establishment of the circulation for LM (upper row) and ZALM (lower row) for an experiment with a northern deep water source. (a) and (c) show $\bar{h}_b$ (in m) as a function of time and latitude for LM and ZALM, respectively. (b) and (d) show $\bar{h}_i$ (in m) as function of time and latitude for LM and ZALM, respectively.

towards the south. During this stage the interior is still quiet. The Kelvin wave reaches the equator after approximately 20 days (see Fig. 2.5a and 2.5c) in both ZALM and LM. We note that in ZALM the propagation speed of the wave response at the western boundary depends to some extent on the western boundary width B_b. Increasing (decreasing) B_b from r/β, the value used in Fig. 2.5, to larger (smaller) values, the southward propagation speed decreases (increases) slightly. The reason is the increasing (decreasing) importance of $\bar{u}_b$ for the dynamics, which should be zero for a pure Kelvin wave, but which is present in both numerical integrations, reducing the southward propagation (Kelvin wave) speed.

The signal is then transported from the boundary layer into the interior (see Fig. 2.5b and 2.5d). This is first achieved by the increasing imbalance of the Kelvin wave dynamics: Approaching the equator, the geostrophic relation for $\bar{v}_b$ cannot be sustained, and a zonal velocity $\bar{u}_b$ must increasingly develop. This disturbance thus couples into the interior

thickness balance and the resulting thickness perturbation spreads to the north and to the south, involving the northward propagating Kelvin wave response at the eastern boundary and zonally and meridionally propagating Rossby waves in the interior. The time scale of this subsequent adjustment is also very similar in LM and ZALM.

2.3.2 Application to primitive equations

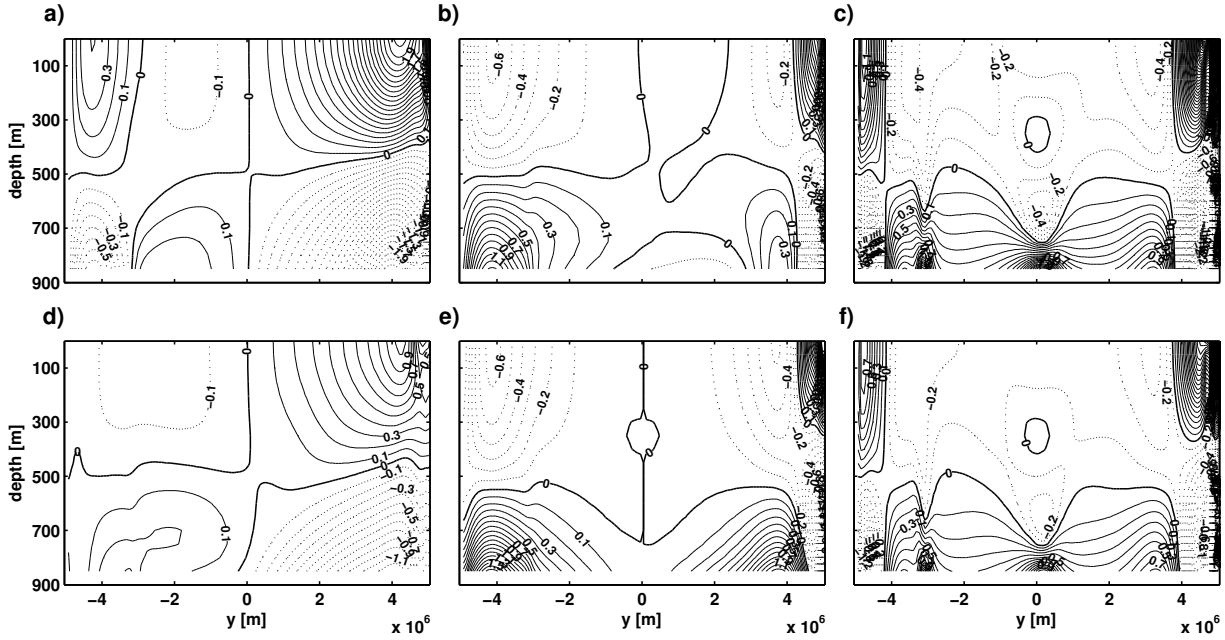

Figure 2.6: Comparison of parameterized variables with the model result for PEM in the experiment with a northern deep water source. The upper row shows Δp_b (a), Δp_i (b) and u_δ (c) in the zonally resolved model. The lower row shows the respective parameterizations: $\bar{p}_i - \bar{p}_b$ (d), $\int_0^y f u_\delta \, dy'$ (e), and $\bar{u}_b$ (f). The contour intervals are $0.1\,\mathrm{m^2\,s^{-2}}$ in (a), (b), (d) and (e) and $0.1\,\mathrm{cm\,s^{-1}}$ in (c) and (f).

The application of the closure, discussed so far for the layered model, to primitive equations is straightforward. Averaged separately over the western boundary layer and over the interior, the equations become

$$\partial_t \bar{u}_\alpha - f\bar{v}_\alpha = -\Delta p_\alpha / B_\alpha + \bar{F}^u_\alpha \tag{2.27}$$

$$\partial_t \bar{v}_\alpha + f\bar{u}_\alpha = -\partial_y \bar{p}_\alpha + \bar{F}^v_\alpha \tag{2.28}$$

$$\partial_t \bar{b}_\alpha + \partial_y \bar{b}_\alpha \bar{v}_\alpha + \partial_z \bar{w}_\alpha \bar{b}_\alpha = \partial_z K_\alpha \partial_z \bar{b}_\alpha - \epsilon_\alpha u_\delta \bar{b}_\alpha / B_\alpha \tag{2.29}$$

$$\partial_y \bar{v}_\alpha + \partial_z \bar{w}_\alpha = -\epsilon_\alpha u_\delta / B_\alpha \tag{2.30}$$

with $\alpha = b, i$ indicating the boundary or interior part, respectively, and $\epsilon_b = 1$ and $\epsilon_i = -1$. The (scaled) pressure $\bar{p}_\alpha$ is related to the buoyancy $\bar{b}_\alpha = -g\bar{\rho}_\alpha/\rho_0$ by the hydrostatic relation $\partial_z \bar{p}_\alpha = \bar{b}_\alpha$. Note that standing-eddy fluxes are neglected in Eq. (2.29). Friction is contained in F^u_α and F^v_α and is specified below. Momentum advection has been neglected as before for the layered model. Convection is parameterized by using large values of the vertical diffusivity K_α in case of unstable stratification.

The pressure differences over the western boundary layer and the interior, $\Delta p_b = p(x = x_\delta) - p(x = x_W)$ and $\Delta p_i = p(x = x_E) - p(x = x_\delta)$, respectively, and the zonal velocity u_δ at the offshore edge of the western boundary need parameterizations. Analogous to the closure in the layered model, we use

$$u_\delta \stackrel{!}{=} \gamma_1 \bar{u}_b \quad , \quad \Delta p_i \stackrel{!}{=} \Delta p_i(y = 0) + \gamma_1 \int_0^y f \bar{u}_b dy' \quad , \quad \Delta p_b \stackrel{!}{=} \gamma_2(\bar{p}_i - \bar{p}_b) \tag{2.31}$$

The interior pressure difference at the equator, $\Delta p_i(y = 0)$, is again set by the steady zonal momentum balance at the equator. The model includes a rigid lid surface boundary condition and a diagnostic relation to find the surface pressure as usual in ocean general circulation models. This zonally averaged primitive equation model will be denoted by ZAPEM.

Fig. 2.6 shows Δp_b, Δp_i and u_δ diagnosed in PEM and their parameterizations given by Eq. (2.31). There is a good agreement concerning sign and structure of the variables and their parameterizations. Only in the southernmost part the parameterization for Δp_b does not show the correct sign, similar to what we have seen for LM (see Fig. 2.3a). It turns out that an important parameter is the boundary layer width B_b, which we have chosen here as $B_b = 3.7r/\beta$ since this value seems to match best the boundary layer width in PEM. Note that the boundary layer is broader than expected from the Rayleigh friction term because we also have included harmonic friction in PEM, which leads to a wider boundary layer.

ZAPEM was programmed in Fortran 90 and the source code as well as a documentation of all important numerical details can be downloaded from `http://www.ifm.zmaw.de/mitarbeiter/prof-dr-carsten-eden/numerical-models/`. The results of ZAPEM after 200 years of integration for two different surface boundary conditions are shown in Fig. 2.7. The configuration and relevant parameters of ZAPEM are identical to the zonally resolved model version (PEM) shown in Fig. 2.2, except for the zonal extent, the closure and that we have omitted the harmonic zonal friction terms (meridional friction is kept) in

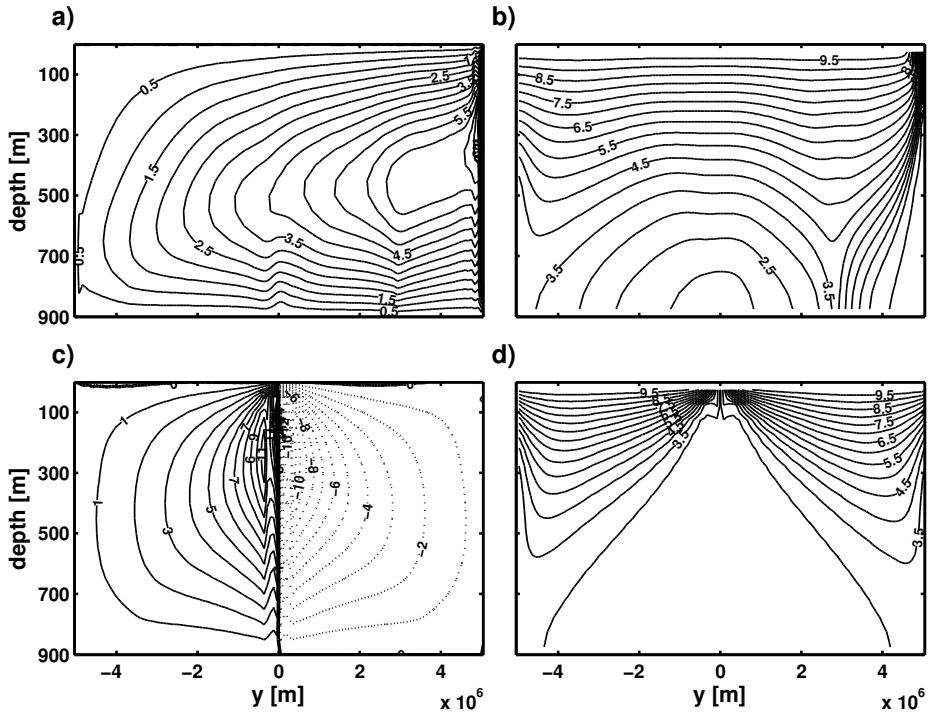

Figure 2.7: Meridional overturning streamfunction ψ ((a), contour interval is 0.5 Sv) and zonally averaged temperature $\bar{T}$ ((b), contour interval is 0.5 °C) in ZAPEM after 200 years of integration with a deepwater formation region at the northern boundary. (c) and (d) show ψ and $\bar{T}$ for the case of the equatorial deepwater source.

ZAPEM. Two different surface boundary conditions are implemented using the two different target surface temperatures, as described in section 2.2 2.2.2. We found without parameter optimization, i.e. for $\gamma_1 = \gamma_2 = 1$ and $B_b = 3.7r/\beta$ already good agreement between ZAPEM and PEM; we therefore made no further attempt of parameter tuning. However, for the polar sinking case (see Fig. 2.7a and 2.7b) the overturning rate in ZAPEM is slightly too strong while the vertical stratification is slightly too weak. For the equatorial sinking (see Fig. 2.7c and 2.7d) the reverse statement holds.

For comparison we also present a primitive equation simulation with the inconsistent closure of the form Eq. (2.1). We use the zonally averaged meridional momentum equation

$$\partial_t \bar{v} = -\partial_y \bar{p} - \gamma_{WS} r \bar{v} + A_h \partial_{yy} \bar{v} + A_v \partial_{zz} \bar{v} \tag{2.32}$$

which is the time-dependent case of Eq. (2.1) and similar to the closure proposed by

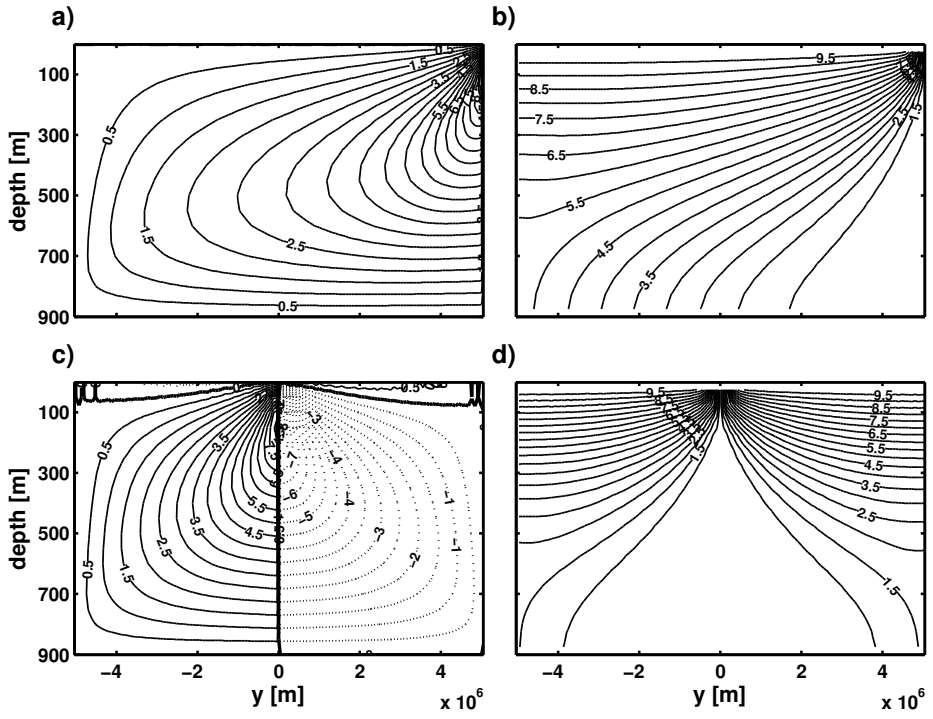

Figure 2.8: Effect of the inconsistent parameterization analogous to Eq. (2.1): Meridional overturning streamfunction ψ ((a), contour interval is 0.5 Sv) and zonally averaged temperature $\bar{T}$ ((b), contour interval is 0.5 °C) of the zonally averaged primitive equation model using the closure Eq. (2.32) after 200 years of integration. The deepwater formation region is located at the northern boundary in (a) and (b). The case of an equatorial deepwater formation region is shown in (c) and (d).

Marotzke et al. (1988) and Wright and Stocker (1991). Note that the Coriolis term is omitted in the meridional momentum balance Eq. (2.32) and replaced by a large Rayleigh damping term. Note also that horizontal and vertical friction is included here only for a consistent comparison with the other simulations; there is no qualitative difference in the results with and without these terms (not shown). The zonally averaged meridional velocity $\bar{v}$ from Eq. (2.32) is used in the budget for $\bar{b}$ for which no further closure is needed; $\bar{w}$ is calculated from the continuity equation.

Fig. 2.8 shows results of an integration using Eq. (2.32) as closure with $\gamma_{WS} = 40$. While the overturning circulation is similar to ZAPEM and PEM, the structure of the buoyancy field reveals a major disagreement for the case of a northern deepwater source (Fig. 2.8b). According to Eq. (2.1) the sign of the meridional buoyancy (pressure) gradient

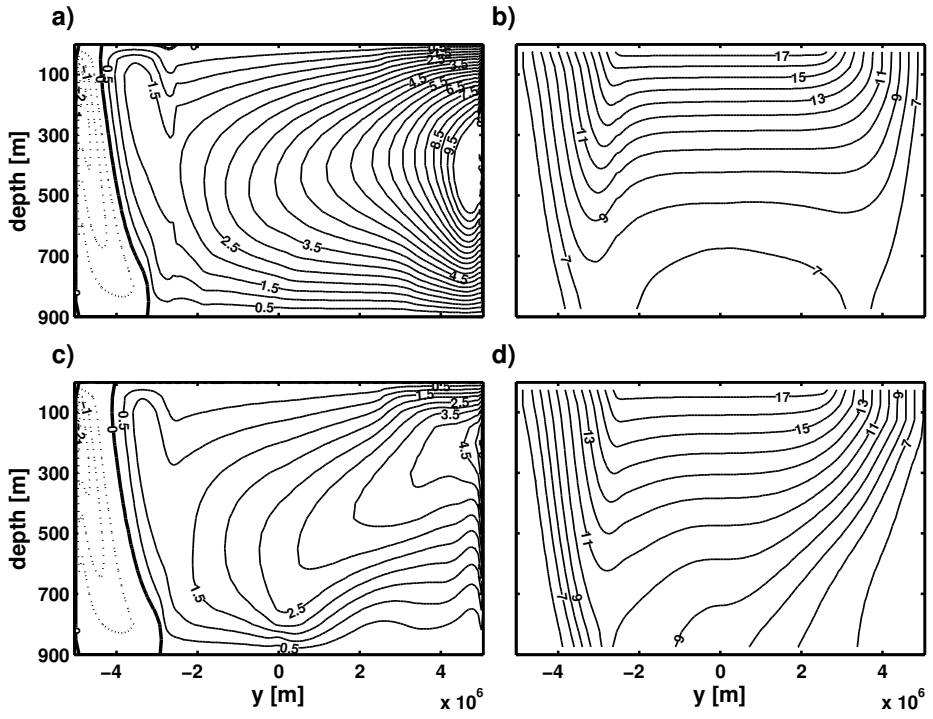

Figure 2.9: Model configuration with Southern Ocean included. Shown are the meridional streamfunction ψ in Sv (a) and (c) and zonally averaged temperature $\bar{T}$ in °C (b) and (d) in the primitive equation model (PEM in (a) and (b)) and the zonally averaged model (ZAPEM in (c) and (d)) after 200 years of integration.

cannot change if the streamfunction consists of one single overturning cell. This clearly contradicts the results of PEM and ZAPEM. Only for the case of the equatorial deepwater source, the buoyancy distribution (Fig. 2.8d) conforms better with that of ZAPEM and PEM, although the northern and southern boundary layers as observed in ZAPEM and PEM are not reproduced.

Fig. 2.9 illustrates the effect of wind forcing and a Southern Ocean part in simulations with ZAPEM and PEM. It is straightforward to include wind forcing and/or zonally periodic boundary conditions in the zonally averaged models ZALM and ZAPEM: The zonally averaged wind stress is used as upper boundary condition in the vertical stress divergences contained in $\bar{F}^u_\alpha$ and $\bar{F}^v_\alpha$. For the zonally unbounded periodic part of the domain, as found in the Southern Ocean, the zonal pressure differences are simply set to zero. Their dynamical role is replaced by the effect of meso-scale eddies, see e.g. Olbers and Visbeck

(2005). This process can be included by interpreting the momentum balance as a balance for the residual velocity, i.e. the sum of the Eulerian mean velocity and the eddy-driven (bolus) velocity (Andrews et al., 1987; Ferreira and Marshall, 2006; Viebahn and Eden, 2010). The effect of meso-scale eddy density mixing is then represented by vertical friction with viscosity $K_{gm}f^2/N^2$ where K_{gm} denotes the isopycnal thickness diffusivity according to the Gent and McWilliams (1990) parameterization. We simply take a constant value of $K_{gm} = 1000\,\mathrm{m^2\,s^{-1}}$.

For the simulations shown in Fig. 2.9, we have chosen the same model domain as before, but for the southern quarter of the basin we apply zonally periodic boundary conditions to represent the Southern Ocean. Note that the setup is similar to that used in Viebahn and Eden (2010): The wind stress over the Southern Ocean region is zonally constant and sinusoidal in the meridional coordinate with a maximum of $2 \times 10^{-4}\,\mathrm{m^2\,s^{-2}}$ located at the center of the periodic domain. The wind stress in the zonally bounded part of the domain is set to zero. The surface boundary condition for buoyancy is a relaxation towards a target buoyancy restoring function with a linear increase (with a rate of $10^{-9}\,\mathrm{s^{-2}}$) in the Southern Ocean region, a constant value from $y = -2560\,\mathrm{km}$ to $y = 2560\,\mathrm{km}$, and a linear decrease of the target buoyancy at the northern part (with the same rate), which generates an equivalent temperature difference of about 20 K between the equator and the polar boundaries. As before, the zonally averaged model (ZAPEM) with our new closure are compared with a simulation with PEM in an identical (but zonally resolved) setup (Fig. 2.9). ZAPEM again reproduce well PEM, although ZAPEM again slightly underestimates the overturning and overestimates the stratification in comparison with corresponding PEM experiment. We further note that temperature and salinity and further passive tracers can be added as variables to the zonally averaged model (not shown). Isopycnal mixing is also implemented as an additional mixing term in the tracer balances. It is also straightforward to include variations in the ocean depth.

2.4 Summary and discussion

The box model by Stommel (1961) and the model by Stommel and Arons (1960) both aim to describe the meridional overturning circulation of the ocean. Much of our knowledge about this important aspect of the ocean's circulation is based on these models. However, Straub (1996) pointed out an inconsistency between the box model and the Stommel and Arons (1960) model, which proofs the assumption Eq. (2.1) to be inconsistent, which

is an inherent assumption in the box model of Stommel (1961) and also in many zonally averaged ocean models (Claussen et al., 2002). We call this inconsistency Straub's dilemma, representing the fact that it appears not possible to infer the meridional transport from the meridional gradient of the zonally averaged pressure. This is because the zonally averaged pressure is dominated by the interior pressure which, on the other hand, is governed by frictionless and linear dynamics expressed by the Sverdrup relation Eq. (2.8). Since this vorticity balance is driven only by the interior upwelling, it is unrelated to the sign of the meridional flow.

In this study, we present and evaluate a new and consistent closure for zonally averaged models to replace the inconsistent closure given by Eq. (2.1), illustrated by numerical integrations with a layered model version and a version based on the full primitive equations. Following Wright et al. (1995), the model domain is divided into an interior part – governed by the Sverdrup relation Eq. (2.8) – and a boundary layer part, where friction plays an important role in the vorticity balance. In contrast to Wright et al. (1995), however, we do not use the vorticity balances of the interior and the boundary layer directly, but we use instead the zonally averaged, interior and boundary layer, momentum and thickness (or buoyancy) budgets. The reason for doing so is that using the meridionally integrated vorticity balances, as suggested by Wright et al. (1995), introduces the need to specify an unknown integration constant. We find the choice of this integration constant to be problematic, since it sets the sign of the meridional transport.

Therefore, we use the vorticity balance only to motivate the parameterization of the zonal pressure difference over the interior, which is needed for the zonally averaged interior zonal momentum balance. The zonal pressure difference across the boundary layer, on the other hand, is parameterized by the difference of the zonally averaged pressure in the interior and the pressure averaged over the boundary layer. The advective exchange between the boundary layer and interior is parameterized using the mean zonal velocity in the boundary layer. The standing eddy fluxes in the non-linear buoyancy budgets are simply neglected. Both in the layered model and the primitive equation model we find good agreement with respect to the evaluation of the parameterizations and model results in terms of the mean simulation of the transports and the thickness (buoyancy) and its time changes.

We advocate to replace the inconsistent closure Eq. (2.1) by the new closure discussed in this study in zonally averaged ocean models. However, we do not imply that the box model by Stommel (1961) is inconsistent as well. On the one hand, the interpretation of

the meridional flow in the ocean as driven by the pressure difference between two boxes and controlled by friction in a hypothetical pipe connecting the two boxes by Stommel (1961), is certainly an incorrect oversimplification of the real dynamics. On the other hand, many results and predictions of the box models can be reproduced by models including the correct dynamics. This agreement might give some confidence in the box model, although we know that its dynamics are incomplete and only a very rough analogue to the real dynamics. We hope that the new zonally averaged model presented here can contribute to further confirm and extend knowledge from the box model about the meridional flow in the ocean.

2.5 Appendix A: Some frequently used inconsistent closures

In this section and the next, we discuss some closures analogous to Eq. (2.1) using the layer equations for simplicity, but the results easily transfer to primitive equations. We also neglect wind forcing, which can, however, easily be incorporated. Marotzke et al. (1988) proposed a closure by abandoning the Coriolis force and implementing (unrealistical) large friction into the meridional momentum balance,

$$0 \;=\; -g'\partial_y \bar{h} - r\bar{v} \tag{2.33}$$

which leads directly to Eq. (2.1) with $\gamma = 1/r$. Here g' is the reduced gravity, h the layer thickness, v the meridional velocity component and $\bar{h}$ and $\bar{v}$ their zonal averages, respectively. Note that we use here Rayleigh friction with friction coefficient r to connect to the model by Stommel and Arons (1960) while Marotzke et al. (1988) originally used vertical diffusion of momentum. However, the specific choice of the friction does not change the fundamental relation Eq. (2.1).

A similar relation was proposed by Wright and Stocker (1991). They consider the zonal momentum balance in the zonally averaged form, where the east-west pressure difference $h_E - h_W$ over the basin width B needs a parameterization. They choose

$$(h_E - h_W)/B = -\gamma_{WS} \sin 2\phi \; \partial_y \bar{h} \tag{2.34}$$

where ϕ denotes latitude and γ_{WS} a constant of order 1. The zonal pressure difference is thus expressed in terms of the local meridional pressure gradient, which is also of the form

Eq. (2.1) assuming that the meridional flow is in geostrophic balance, with a parameter γ proportional to $\cos\phi$. This setting is supported by numerical experiments with a three-dimensional (but highly simplified) circulation model, but as argued by Greatbatch and Lu (2003), the support is because of the highly diffusive nature of the ocean model. Note that the closure is not based on any dynamical concepts.

Wright et al. (1998) avoid a direct closure for the pressure difference $h_E - h_W$. The zonal momentum balance is entirely abandoned. In fact, the zonally averaged meridional momentum balance is written as

$$f\bar{u} + g'\partial_y\bar{h} = f(\bar{u} - \bar{u}^{(g)}) = -r\bar{v} \tag{2.35}$$

with Coriolis parameter f, the zonally averaged zonal velocity $\bar{u}$ and its geostrophic component $\bar{u}^{(g)} = -(g'/f)\partial_y\bar{h}$. To determine the meridional velocity $\bar{v}$ from Eq. (2.35) the ageostrophic zonal velocity $\bar{u} - \bar{u}^{(g)}$ must be known and thus has to be parameterized. For this reason, Wright et al. (1998) divide the zonal extend B of the ocean again into a western frictional boundary layer part of width B_b and an interior part of width $B_i = B - B_b \gg B_b$. They write

$$B(\bar{u} - \bar{u}^{(g)}) = B_i(\bar{u}_i - \bar{u}_i^{(g)}) + B_b(\bar{u}_b - \bar{u}_b^{(g)}) \tag{2.36}$$

with the zonal velocities $\bar{u}_i$ and $\bar{u}_b$ averaged over the interior and western boundary layer, respectively and where the superscript (g) denotes the geostrophic component of the velocity. The interior flow is largely geostrophic and thus, Wright et al. (1998) assumed the product $B_i(\bar{u}_i - \bar{u}_i^{(g)})$ to be small. In the boundary layer, the flow has both a geostrophic and an ageostrophic component, but u vanishes on the continental side of the layer and should be largely governed by the geostrophic balance on the offshore edge of the western boundary layer. The interior geostrophic component continues only moderately changed into the boundary layer and to the actual boundary. Hence, the magnitudes of $\bar{u}_b - \bar{u}_b^{(g)}$ and $\bar{u}_b^{(g)}$ should be similar but of opposite signs in the boundary layer, and

$$B(\bar{u} - \bar{u}^{(g)}) \approx B_b(\bar{u}_b - \bar{u}_b^{(g)}) \approx -B_b\bar{u}_i^{(g)} \approx -B_b\bar{u}^{(g)} \tag{2.37}$$

should hold. Inserting the parameterized ageostrophic velocity into the meridional mo-

mentum balance then yields

$$\bar{v} = -\frac{g' B_b}{rB} \partial_y \bar{h} \tag{2.38}$$

which is identical to Eq. (2.1) with a suitable parameter $\gamma = B_b/(rB)$. Note that this closure is entirely of geometric nature: it uses the observed structure of a basin-wide circulation with a narrow western boundary current but not any further dynamics.

2.6 Appendix B: The consistent closure by Wright et al. (1995)

Wright et al. (1995) propose a dynamically consistent closure by splitting the ocean basin into a western boundary layer and an interior and considered the vorticity budgets averaged separately over both regions. Assuming a frictionless interior and using specific parameterizations for friction in the western boundary layer, they derive a non-local relation between the meridional transport and zonally averaged pressure. Because the original closure of Wright et al. (1995) needs the specification of integration constants which are difficult to determine, we have presented in section 2.3 a generalization of the concept by Wright et al. (1995), which does not need the specification of integration constants.

We found the derivation of the closure in Wright et al. (1995) unnecessarily complicated. Here we give an alternative simplified derivation with less assumptions to arrive at a similar equation. The analysis is again performed for the layer model and starts with the zonal momentum balance in the zonally averaged from

$$-f\bar{v}_b = -g'(h_\delta - h_W)/B_b - r\bar{u}_b \tag{2.39}$$

$$-f\bar{v}_i = -g'(h_E - h_\delta)/B_i - r\bar{u}_i \tag{2.40}$$

which are identical to Eq. (2.12) and Eq. (2.15) neglecting the time tendency terms. Again, indices W, E and δ denote that the values are taken at the western or eastern boundary or at the interface between interior ocean and boundary layer, respectively. The overbars denote zonal averages over the interior with additional index i or boundary layer with index b, and B_b and B_i denote the width of the boundary layer and the interior, respectively. Only a few approximations now lead to the closure by Wright et al. (1995). First, the friction

term in Eq. (2.40) will be neglected. Because of the kinematic boundary condition at the eastern boundary, $u_E = 0$, it follows from Eq. (2.3) that $\partial_y h_E = 0$ or $h_E = const.$ Second, the thickness perturbation h_W along the western boundary in Eq. (2.40) is eliminated by the meridional velocity v_W using the steady meridional momentum balance at x_W in the form

$$0 \;=\; -g'\partial_y h_W - r v_W \tag{2.41}$$

and v_W is parameterized by $\bar{v}_b$. Note that $u_W = 0$ was assumed. Next the friction coefficient r in Eq. (2.41) is replaced by βB_b using $B_b = r/\beta$ as the boundary layer width according to Stommel (1948). The meridional integral of Eq. (2.41) with starting point at y_0 can be used to eliminate h_W from Eq. (2.39) to end up with

$$f\bar{v}_b - \beta \int_{y_0}^{y} \bar{v}_b dy' \;=\; g'(h_\delta - h_W(y_0))/B_b + r\bar{u}_b \tag{2.42}$$

where integration limit y_0 is arbitrary. The meridional velocities $\bar{v}_i$ and $\bar{v}_b$ then follow from

$$f\bar{v}_b - \beta \int_{y_0}^{y} \bar{v}_b dy' = \int_{y_0}^{y} f\partial_y \bar{v}_b dy' \;=\; g'(h_\delta - h_W(y_0))/B_b + r\bar{u}_b \tag{2.43}$$

$$f\bar{v}_i \;=\; g'(h_E - h_\delta)/B_i \tag{2.44}$$

and are seen to be both determined by h_δ. Wright et al. (1995) propose the closure $h_\delta = \gamma\bar{h}$, where $\bar{h}$ denotes the zonally averaged thickness, and neglect the last term in Eq. (2.43) related to friction. Both are quite good assumptions for the layered model outside the northern and southern boundary layers (not shown). Note, however, that Eq. (2.43) only determines the derivative of $\bar{v}_b$ and thus it it is necessary to set an integration constant for $\bar{v}_b$. One may take here $\bar{v}_b(y_0)$ which by Eq. (2.43) is obviously related to the unknown $h_W(y_0)$. Note that the frictionless interior balance leads to $h_E = h_\delta(y = 0) = \gamma\bar{h}(y = 0)$.

To arrive at the central equation of the Wright et al. (1995) model, Eq. (2.43) is divided by f and integrated from y_0 to y (in the same hemisphere to avoid the singularity at $y = 0$) to give $\bar{v}_b$, involving now the unknown $\bar{v}_b(y_0)$. The total meridional flow is then governed by

$$B\bar{v} \;=\; B_b\bar{v}_b(y_0) + \gamma g' \int_{y_0}^{y} f^{-1}\partial_y \bar{h} dy' - \gamma(g'/f)(\bar{h} - \bar{h}(y = 0)) \tag{2.45}$$

Wright et al. (1995) use as integration constant the boundary transport at the northern and southern boundary, which they relate to the interior flow at the respective boundary (Eq. (2.45) is used twice to circumvent the singularity at the equator). It becomes clear that this closure implies that the information about the placement of the deepwater source — which is invisible to the interior flow — must be contained in $\bar{h}$ at the northern and southern boundary layers.

Fig. 2.1d to Fig. 2.1f show indeed that $\bar{h}$ at the northern (southern) boundary layer for the experiment with northern (southern) sinking is slightly higher and reaches a larger value at the northern (southern) end of the domain than in the experiment with equatorial and southern (northern) sinking. It is this small difference which has to determine the sign of the flow in the non-local relation between $\bar{v}$ and $\bar{h}$ of Wright et al. (1995). Consequently, an evaluation (not shown) of the closure based on Eq. (2.45) in the layered model shows that it is not able to predict $\bar{v}$ using only $\bar{h}$ from the model. The reason is that the assumption leading to the closure, i.e. a frictionless interior flow, breaks down in the northern and southern boundary layer. The unknown integration constant then determines the meridional flow. We propose in section 2.3 a more robust way to determine the meridional flow, which avoids Eq. (2.41) and thus the meridional integration and appearance of unknown integration constants.

Chapter 3

Validating different parameterizations for mixed layer eddy fluxes induced by baroclinic instability

This chapter is under review in the Journal of Physical Oceanography

Citation: Brüggemann, Nils, Carsten Eden, 2013: Validating different parameterizations for mixed layer eddy fluxes induced by baroclinic instability. submitted to J. Phys. Oceanogr.

Abstract

In this study, we discuss two different parameterizations for the effect of mixed layer eddies, one based on ageostrophic linear stability analysis (ALS) and the other one based on a scaling of the potential energy release by eddies (PER). Both parameterizations contradict each other in two aspects. First, they predict different functional relationships between the magnitude of the eddy fluxes and the Richardson number (Ri) related to the background state. Secondly, they also predict different vertical structure functions for the horizontal eddy fluxes.

Numerical simulations for two different configurations and for a large range of different background conditions are used to validate the parameterizations. It turns out that the mean deviation between both, ALS and PER, and the diagnosed eddy fluxes is less than a factor of two, varying Ri over three orders of magnitude. While ALS performs slightly better in an equilibrated forced-balanced flow scenario, we obtain a slightly better performance of PER for a spin-down scenario. In both scenarios, the vertical structure of the meridional eddy fluxes predicted by ALS is more accurate than that of PER while the vertical structure of the vertical eddy fluxes is well predicted by both parameterizations.

3.1 Introduction

High resolution satellite altimetry and numerical simulations of the near-surface ocean show variability on scales much smaller than the typical Rossby radius of the ocean interior (Munk et al., 2000; Klein et al., 2008). The dynamics on these scales are often called submesoscales and it is assumed that ageostrophic processes have to be taken into account to describe these phenomena. Submesoscale dynamics might predominantly occur within the ocean mixed layer, where the influence of the atmosphere by convective and wind-induced mixing leads to dynamic conditions which are not in quasi-geostrophic balance anymore, although out of balance dynamics might also be met under certain circumstances in the ocean interior. Haine and Marshall (1998) investigate different mechanisms which play a role for the upper ocean mixed layer dynamics. All these processes act to re-stratify the mixed layer and occur on length scales which are too small to be resolved by today's climate models. Consequently, Oschlies (2002) observed a bias in e.g. the mixed layer depth and the surface ocean heat flux in coarser but eddying ocean models, suggesting that these processes might also play an important role for e.g. biogeochemical cycles.

The discussion of ageostrophic instabilities by Stone (1966) shows that a key param-

eter to distinguish between different kinds of instabilities is the Richardson number, Ri – the ratio of the vertical buoyancy gradient divided by the square of the vertical shear of horizontal velocity. While baroclinic instabilities can occur for all Ri, symmetric instabilities are only met for $\mathrm{Ri} < 1$ and Kelvin-Helmholtz instability for $\mathrm{Ri} < 0.25$. In addition, the growth rate of baroclinic and symmetric instabilities also depends on Ri. In typical idealized model simulations of the spin-down of ocean fronts (e.g. Haine and Marshall (1998); Boccaletti et al. (2007); Fox-Kemper et al. (2008); Bachman and Fox-Kemper (2013)) symmetric instabilities start to re-stratify the ocean front if $\mathrm{Ri} < 1$ and lead to stable conditions with respect to symmetric instabilities ($\mathrm{Ri} \geq 1$). After this first phase of re-stratification and after the geostrophic adjustment, baroclinic instabilities set in and lead to a further spin-down of the front caused by baroclinic eddy buoyancy fluxes. Baroclinic instabilities occur in nearly every flow system with vertically sheared velocity and are therefore important to be parameterized if ocean models are not able to resolve them.

Stone (1966) and Molemaker et al. (2005) find that even for small Ri characteristic for the mixed layer, the dominating baroclinic instabilities are still geostrophically balanced to a large extent, although they might also come in concert with secondary unbalanced instabilities. This means that, if the mixed layer instabilities are predominantly in geostrophic balance, they might be well described by mesoscale eddy parameterizations designed for the interior of the ocean with large Ri (Green, 1970; Killworth, 1997; Eden and Greatbatch, 2008b; Eden, 2011). On the other hand, there are also parameterizations developed for small Ri and thus ageostrophic baroclinic instabilities (Stone, 1972a) and parameterizations especially developed for the mixed layer (Fox-Kemper et al., 2008). All these parameterizations need to somehow connect the magnitude of the eddy mixing to the mean state. Since the Richardson number Ri is an important measure for the characteristics of the mean state instabilities, it is not surprising that most parameterizations associate the magnitude of the eddy fluxes by some kind of functional relationship to Ri. Hence, these parameterizations can be distinguished by their dependency on Ri.

The parameterization of Fox-Kemper et al. (2008) is based on different physical arguments than that of Stone (1972a) (in the quasi-geostrophic limit the latter is in fact very similar to the one by Killworth (1997) and Eden (2011)) and thus suggests a different functional relationship between the Richardson number and the amplitude of the eddy fluxes. The aim of this study is to discuss differences in these two parameterizations for mixed layer eddies. By comparing the different Ri-dependencies of the parameterizations with the diagnosed dependency in a numerical model, we aim to clarify which Ri-dependency

is more appropriate to parameterize the eddy fluxes. Since both parameterizations differ also with respect to the vertical structure of the meridional eddy fluxes, we furthermore compare the vertical profiles of the eddy fluxes from the numerical simulations and that of the parameterizations. All these investigations are performed for two different scenarios, an equilibrated flow scenario and the spin-down of a temperature front, and over a wide range of values for Ri.

In the following, we will introduce the parameterizations of Fox-Kemper et al. (2008) and Stone (1972a) in Sec. 3.2. Numerical simulations for two different scenarios are considered to validate these parameterizations. The first one is a baroclinically unstable flow, where re-stratification is prevented by diabatic temperature restoring. A description of the setup and a discussion of the results can be found in Sec. 3.3. The second scenario is the spin-down of a baroclinically unstable temperature front. Section 3.4 provides a detailed description of the setup and the results. Finally, Sec. 3.5 provides a discussion of the obtained results and their implications for parameterizing mixed layer eddy fluxes in numerical ocean models.

3.2 Parameterizations for mixed layer eddy fluxes

To discuss the influence of mixed layer eddy fluxes on the mean buoyancy budget, we average the equation for buoyancy b

$$\partial_t \bar{b} + \nabla \cdot \bar{\boldsymbol{u}} \bar{b} + \nabla \cdot \overline{\boldsymbol{u}' b'} = \bar{D}. \tag{3.1}$$

For simplicity, we consider zonal averages, i.e. $\overline{()}$ denotes a zonal average and $()'$ the deviations to that average. In Eq. (3.1), the local change of mean buoyancy $\bar{b}$ is given by the advection of mean buoyancy by the mean velocity $\bar{\boldsymbol{u}}$, the divergence of the eddy fluxes $\overline{\boldsymbol{u}' b'}$ and diabatic processes denoted by D. While the mean flux $\bar{\boldsymbol{u}} \bar{b}$ can directly be determined in a numerical ocean model, the eddy flux $\overline{\boldsymbol{u}' b'}$ needs to be parameterized.

As described in the following, the structure and strength of the eddy fluxes depends on the background state of the flow. A non-dimensionalization of the Navier-Stokes equations shows that basically three parameters determine the inviscid adiabatic equations, namely the Richardson number Ri, the Rossby number Ro and the aspect ratio δ (see Sec. 3.6). Therefore, it is convenient to derive parameterizations for the eddy fluxes in dependency on these parameters.

3.2.1 A parameterization based on linear stability analysis

The concept of using linear stability analysis to determine eddy fluxes is based on the following ideas (see e.g. Green (1970), Stone (1972a), Killworth (1997) and Eden (2011)): As long as perturbations to a mean state are small, all perturbation variables can be obtained by solving a linearized set of equations for waves. From the solution for these perturbation variables the eddy fluxes can be calculated from the correlations between velocity and buoyancy perturbation. If the frequency for certain wave modes becomes complex, there is an exponential increase or decay of these waves. The fastest growing mode is expected to dominate over the others and therefore, this fastest growing mode is assumed to be responsible for the eddy mixing.

As soon as the exponentially growing perturbations reach the same magnitude as the background state, the linearization of the equation is certainly no longer a good approximation and non-linear effects become important. However, as long as there is no significant energy cascade transporting energy to different scales, it is reasonable to assume that the eddies retain their initial scales and structure and that it is possible to infer on the eddy fluxes by the linear solutions. Nevertheless, it remains to find a proper scaling for the magnitude of the eddy fluxes at the end of their exponential growth in the fully turbulent regime.

Stone (1972a) argues that the exponential growth of the wave is stopped as soon as non-linear effects become important. Thus, the perturbation velocity v' takes the same order of magnitude as the background velocity and $v' \propto M^2 H/f$ yields the scaling for the eigenvectors. A different idea to scale the amplitude of the eigenvectors is suggested by Killworth (1997) who suggests to use the time and length scale of the fastest growing mode to scale the meridional velocity component v'. For quasi-geostrophic conditions (i.e. large Ri), constant meridional and vertical buoyancy gradients M^2 and N^2, respectively, and vanishing planetary vorticity gradient, the growth rate $\sigma_{\max}$ of the fastest growing mode and the corresponding wave number $k_{\max}$ can be derived as follows (Eady, 1949):

$$k_{\max} \approx 1.6 L_r^{-1}, \qquad \sigma_{\max} \approx 0.3 \frac{f}{\sqrt{\mathrm{Ri}}} \tag{3.2}$$

where $L_r = NH/f$ denotes the Rossby radius and $\mathrm{Ri} = N^2 f^2 / M^4$ the Richardson number for a flow in geostrophic balance with depth H. Applying the scaling of Killworth (1997) then yields $v' = \sigma_{\max}/k_{\max} \approx 0.25 M^2 H/f$ and therefore, basically the same scaling as suggested by Stone (1972a).

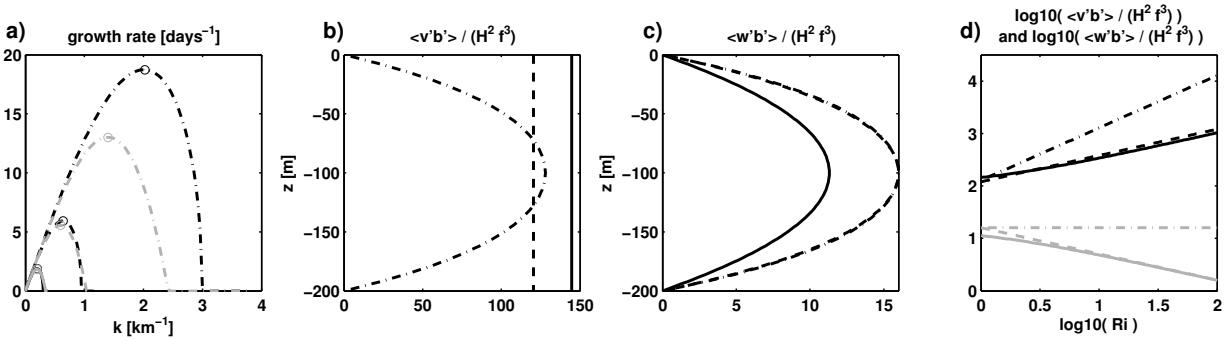

Figure 3.1: (a) Growth rate inferred from linear stability analysis as a function of the along-stream wave number k for the solution by Eady (black) and Stone (grey) for $\mathrm{Ri} = 1$ (dashed-dotted), $\mathrm{Ri} = 10$ (dashed) and $\mathrm{Ri} = 100$ (solid). Maximum growth rates $\sigma_{\max}$ at wave numbers $k_{\max}$ are indicated by circles. (b) and (c) denote the vertical profiles of $\overline{v'b'}$ and $\overline{w'b'}$, respectively as determined by Eq. (3.3) (dashed), Eq. (3.6) (solid) and Eq. (3.9) (dashed-dotted) for $\mathrm{Ri} = 1$ (dashed line in (c) is nearly indistinguishable similar to the dashed-dotted line). (d) Maximum of the eddy fluxes $\overline{v'b'}$ (black) and $\overline{w'b'}$ (grey) as a function of Ri (line styles are the same as in (b) and (c)).

Following the ideas of Stone (1972a) and Killworth (1997), it is possible to calculate exact expressions for the eddy fluxes of the Eady (1949) model as detailed in Sec. 3.7:

$$\frac{\overline{v'b'}}{H^2 f^3} = -1.9 C_{\mathrm{E}} \sqrt{\mathrm{Ri}} \alpha^3, \qquad \frac{\overline{w'b'}}{H^2 f^3} = C_{\mathrm{E}} \frac{1}{\sqrt{\mathrm{Ri}}} \mu_{\mathrm{E}}(z) \alpha^2 \tag{3.3}$$

where C_{E} denotes a tuning constant of order one and $\alpha = \mathrm{Ro}/\delta$ is the ratio between the Rossby number $\mathrm{Ro} = U/(fL)$ and the aspect ratio $\delta = H/L$ for a flow with velocity scale U and horizontal and vertical length scales L and H, respectively. While $\overline{v'b'}$ is vertically constant, the vertical dependency of $\overline{w'b'}$ is denoted by $\mu_{\mathrm{E}}(z)$ which has a maximum of one at $z = -H/2$ and is given by

$$\mu_{\mathrm{E}}(z) = \frac{\cosh\left(k_{\max} L_r \left(\frac{2z}{H} + 1\right)\right) - \cosh\left(k_{\max} L_r\right)}{1 - \cosh\left(k_{\max} L_r\right)}. \tag{3.4}$$

This kind of closure was already successfully implemented and validated in numerical ocean models in Killworth (1997), Eden (2011) and Eden (2012) for general profiles of N^2 and M^2 and including also the planetary vorticity gradient.

Within the mixed layer, especially at fronts, strong vertical shears and weak stratifications are likely to occur such that Ri becomes small and ageostrophic processes have to be taken into account. For the ageostrophic equations, it is no longer possible to find analyti-

cal solutions as for the quasi-geostrophic Eady problem even for constant N^2 and M^2 and vanishing planetary vorticity gradient. Stone (1966) derives approximative solutions for the ageostrophic linearized equations and finds quite similar solutions to the ones of Eady (1949) for Ri ≥ 1. For the fastest growth rate $\sigma_{\max}$ and the corresponding wave length $k_{\max}$, Stone (1966) obtains

$$k_{\max} = \sqrt{\frac{\mathrm{Ri}}{1+\mathrm{Ri}}}\sqrt{\frac{5}{2}}L_r^{-1}, \qquad \sigma_{\max} = \sqrt{\frac{\mathrm{Ri}}{1+\mathrm{Ri}}}\sqrt{\frac{5}{54}}\frac{f}{\sqrt{\mathrm{Ri}}}. \tag{3.5}$$

The only difference between these results and the ones from Eady (1949) is an additional factor $\sqrt{\mathrm{Ri}/(1+\mathrm{Ri})}$ which approaches one for large Ri. Fig. 3.1a indicates that there is hardly any disagreement between the solutions of Eady (1949) and Stone (1966) for large Ri, while for smaller Ri the factor $\sqrt{\mathrm{Ri}/(1+\mathrm{Ri})}$ becomes more and more important (see e.g. dashed dotted lines in Fig. 3.1a for Ri = 1).

As before, it is possible to derive the eddy fluxes by linear stability analysis up to a proportionality constant from the correlations of the eigenvectors for v', w' and b'. If we use the same scaling as suggested by Killworth (1997), namely assuming $\sqrt{\overline{v'v'}} \propto \sigma_{\max}/k_{\max}$, we obtain

$$\frac{\overline{v'b'}}{H^2 f^3} = -\frac{8}{5}C_S\sqrt{1+\mathrm{Ri}}\alpha^3, \qquad \frac{\overline{w'b'}}{H^2 f^3} = C_S\frac{1}{\sqrt{1+\mathrm{Ri}}}\mu_S(z)\alpha^2, \tag{3.6}$$

where C_S denotes another tuning parameter of order one. Formally, these equations are valid only in the long wave limit as noted by Stone (1972b). We use this approximative form and compare the eddy fluxes obtained by Eq. (3.6) with numerical solutions of the eigenvalue problem below and find good agreement. As in Eady's solution and depicted in Fig. 3.1b, there is no vertical dependency of $\overline{v'b'}$ in Stone's solution. The vertical structure of $\overline{w'b'}$ denoted by $\mu_S(z)$ is derived by Stone (1972b) as

$$\mu_S(z) = -4\frac{z}{H_0}\left(\frac{z}{H_0}+1\right) \tag{3.7}$$

and therefore only marginally deviates from the hyperbolic structure of $\overline{w'b'}$ obtained for the Eady problem (see Fig. 3.1c).

Although the solution of Stone (1972a) accounts for ageostrophic effects, it is quite similar to the one obtained by Eady (1949) for the quasi-geostrophic limit of large Ri. Fig. 3.1d shows the maximum of the eddy fluxes $\overline{v'b'}$ (solid curves) and $\overline{w'b'}$ (dashed curves)

for both parameterizations over a large range of values for Ri. There are only differences for $\mathrm{Ri} = \mathcal{O}(1)$ between Eady's and Stone's solution due to the additional factor $\sqrt{\mathrm{Ri}/(1+\mathrm{Ri})}$ in Stone's solution. For large Ri this factor approaches one and Stone's solution becomes identical to the one of Eady (1949).

3.2.2 The parameterization of Fox-Kemper et al. (2008)

Fox-Kemper et al. (2008) derive a parameterization for the spin-down of a baroclinic density front with typical mixed layer conditions by scaling the magnitude of the potential energy release. Their key assumption is that the potential energy release ($\Delta\mathrm{PE} = g/\rho_0 \Delta\rho \Delta z$) is achieved by the vertical eddy flux. Thus, they assume $\Delta\mathrm{PE}/\Delta t \propto -\Delta z(\Delta y M^2 + \Delta z N^2)/\Delta t = -\overline{w'b'}$, where Δz and Δy denote the vertical and horizontal eddy length scales, respectively, and Δt the eddy time scale. To infer these eddy length and time scales, the following assumptions are made:

1. The eddy time scale is an advective time scale $\Delta t \propto \Delta y/U_e$, where U_e denotes the eddy velocity.

2. The eddy velocity is set to be proportional to the thermal wind velocity $U_e \propto \frac{M^2}{f} H$.

3. The eddy depth scale Δz is assumed to be proportional to the mixed layer depth H.

4. The eddy fluxes are along surfaces inclined by half of the isopycnal slope, i.e. $\frac{\Delta z}{\Delta y} = -\frac{1}{2}\frac{M^2}{N^2}$ as can be inferred from parcel theory (Haine and Marshall, 1998).

The second assumption is also made by Stone (1972a) and the assumptions three and four do not contradict the results of the linear stability analysis. Therefore, the parameterizations of Stone (1972a) and Fox-Kemper et al. (2008) differ only with respect to the first assumption[1]: While this assumption of Fox-Kemper et al. (2008) leads to a time scale $T_e = \mathrm{Ri}/f$, the scaling by Stone (1972a) as well as that by Killworth (1997) suggest $T_e = \sqrt{1+\mathrm{Ri}}/f$.

The assumptions discussed so far yield only the magnitude of the eddy fluxes and Fox-Kemper et al. (2008) use the vertical structure $\mu(z)$ obtained from the linear stability

[1]Note that assumption four only corresponds to Stone (1972a) at the steering level.

analysis for $\overline{w'b'}^2$. To obtain $\overline{v'b'}$, Fox-Kemper et al. (2008) assume in correspondence to assumption four $\overline{v'b'} = -2\overline{w'b'}N^2/M^2$ and thus obtain

$$\frac{\overline{v'b'}}{H^2 f^3} = -2C_F \mu_F(z) \mathrm{Ri} \alpha^3, \qquad \frac{\overline{w'b'}}{H^2 f^3} = C_F \mu_F(z) \alpha^2, \tag{3.9}$$

where C_F is another tuning parameter of order one.

3.2.3 Comparison of the parameterizations

There are two principal differences between the parameterization of Fox-Kemper et al. (2008) Eq. (3.9) and the one based on linear stability analysis given by Eq. (3.6). The first one is a different dependency of the eddy fluxes on Ri resulting from assumption one of the last section. This means that even if both solutions are accurately tuned for a certain Ri, there might be a difference in the magnitude of the eddy fluxes for different Ri. Fig. 3.1d shows the maxima of the eddy fluxes $\overline{v'b'}$ and $\overline{w'b'}$ from Eq. (3.9) together with the eddy fluxes of the quasi-geostrophic linear stability problem Eq. (3.3) and the ageostrophic problem Eq. (3.6). Here, the tuning constants are chosen in the way that both parameterizations agree best for Ri = 1. For Ri = 100, however the difference between both parameterizations is roughly one order of magnitude. Choosing different tuning coefficients will shift the curves parallel to the vertical axis in the double logarithmic plot, but there will always remain a large difference for certain Ri.

The second difference concerns the vertical structure of the horizontal eddy flux $\overline{v'b'}$. Because Fox-Kemper et al. (2008) assume $\overline{w'b'}/\overline{v'b'} = 0.5M^2/N^2$ everywhere and not only at the steering level, they end up with a parabolic structure function for $\overline{v'b'}$ that vanishes at the surface and the mixed layer base. Contrary, linear stability analysis suggests a constant horizontal flux throughout the whole mixed layer (see Fig. 3.1b).

The differences between both parameterizations become more illustrative if we consider a down-gradient closure for the horizontal eddy fluxes and the ratio of the horizontal and

[2] In fact Fox-Kemper et al. (2008) use a higher order solution in the zonal wave number for the linear stability analysis than that of Stone (1972b) and apply to this solution the large Ri limit:

$$\mu_F(z) = -4\frac{z}{H_0}\left(\frac{z}{H_0}+1\right)\left(1+\frac{5}{21}\left(\frac{2z}{H_0}+1\right)^2\right). \tag{3.8}$$

the vertical eddy fluxes

$$\overline{v'b'} = -K\partial_y\bar{b}, \qquad \overline{w'b'} = \gamma\overline{v'b'} \tag{3.10}$$

with the lateral diffusivity $K = -\overline{v'b'}/\partial_y\bar{b}$ and the eddy flux ratio $\gamma = \overline{w'b'}/\overline{v'b'}$. In order to parameterize K, it is common to use mixing length theory and to express K as the product of a typical eddy velocity U_e and a length scale L_e

$$K \propto U_e L_e. \tag{3.11}$$

Both, the parameterization of Fox-Kemper et al. (2008) and the parameterization based on linear stability analysis assume that the eddy velocity scale is proportional to the thermal wind velocity and that the eddy fluxes are along surfaces inclined by $s/2$ at the steering level, where $s = -M^2/N^2$ denotes the isopycnal slope. Thus, the difference between both parameterizations concerning the amplitude of the eddy fluxes can be identified from a different choice of the eddy length scale. Linear stability analysis predicts $L_e = \sqrt{(\mathrm{Ri}+1)/\mathrm{Ri}}L_r$ and therefore, a length scale essentially given by the Rossby radius L_r with only small deviations for $\mathrm{Ri} = \mathcal{O}(1)$. In contrast, Fox-Kemper et al. (2008) use $L_e = H_0 N_0^2/|M_0^2| = \sqrt{\mathrm{Ri}}L_r$ as a characteristic eddy length scale, i.e. a length scale that deviates from the parameterization based on linear stability analysis.

One might now construct the amplitude of the eddy fluxes $\overline{v'b'}$ and $\overline{w'b'}$ with Eq. (3.10) and Eq. (3.11). By assuming $U_e = M^2H/f$, $\gamma \approx 1/2s$ and $L_0 = \sqrt{\mathrm{Ri}}L_r$ or $L_0 = \sqrt{(\mathrm{Ri}+1)/\mathrm{Ri}}L_r$, we obtain either the parameterizations of Fox-Kemper et al. (2008) or the one based on linear stability analysis, respectively. Instead of composing the lateral diffusivity by a velocity and a length scale, it would also be possible to compose it by a length and a time scale T_e. If we assume the latter to be $T_e = L_e/U_e$, we obtain $T_e = \sqrt{\mathrm{Ri}+1}/f_0$ for the parameterization based on linear stability analysis and $T_e = \mathrm{Ri}/f_0$ for the parameterization of Fox-Kemper et al. (2008). Both time scales as well as the length scales differ.

In an adiabatic steady state, the diapycnal component of the eddy fluxes will vanish (except for a possible rotational component) and γ will be equal to the isopycnal slope as assumed by e.g. Gent et al. (1995), Killworth (1997) and Eden (2011). In the presence of small scale diabatic processes, however, there will be a net diapycnal transport of the eddies (Tandon and Garrett, 1996; Eden and Greatbatch, 2008a). Because the mixed layer is predestinated to those diabatic processes, it is reasonable to expect non-vanishing

diapycnal eddy fluxes and diapycnal diffusivities also in equilibrated scenarios for the mixed layer. In fact, we explicitly apply diabatic conditions to prevent the buoyancy front from slumping down in our equilibrated scenarios. Therefore, it seems more promising to assume $\gamma < s$ than $\gamma = s$ for our spin-down scenario but probably also for the real mixed layer.

If the system is not steady, as it is the case for a re-stratifying density front, γ is likely to be smaller than the isopycnal slope even if the flow is completely adiabatic. Green (1970) and Stone (1972a) suggest that γ takes values at the steering level close to $1/2s$. Similarly, Fox-Kemper et al. (2008) suggests $\gamma = 1/2s$ for the whole vertical profiles of $\overline{v'b'}$ and $\overline{w'b'}$ and not only at the steering level. As detailed below, we also expect diabatic effects to occur in our spin-down scenario due to numerical diffusion. Therefore, we cannot expect a completely adiabatic re-stratification process in the spin-down scenario. However, as mentioned above, this scenario is probably not unrealistic with respect to the ocean mixed layer, where diabatic processes will certainly accompany the re-stratification by baroclinic instabilities.

These considerations bring us to the following questions, which we aim to answer by the diagnosis of numerical model results:

1. Which dependency of $\overline{v'b'}$ and $\overline{w'b'}$ on Ri is more appropriate, the one by Eq. (3.9) or the one based on linear stability analysis given by Eq. (3.6)?

2. What is the vertical structure of the horizontal eddy fluxes $\overline{v'b'}$? A constant profile as suggested by the linear stability analysis or a parabolic shaped structure as suggested by Fox-Kemper et al. (2008)?

3. Are there qualitative differences of the parameter dependency of the eddy fluxes in a spin-down scenario in comparison to an equilibrated scenario?

3.3 Baroclinic instabilities in a forced-dissipative scenario

3.3.1 Numerical simulations

To simulate mixed layer instabilities, we use the MIT General Circulation Model (MITgcm, Marshall et al. (1997)). The configuration resembles that of Eady (1949) and Stone (1966). Our model domain consists of a reentrant channel with periodic boundary conditions at zonal boundaries and solid walls at meridional boundaries. For simplicity, we use

Symbol	meaning	value
(nx, ny, nz)	number of grid points in x, y and z direction	(120, 120, 40)
H_0	depth of the basin	$200\,\mathrm{m}$
f_0	Coriolis parameter	$7 \times 10^{-5}\,\mathrm{s}^{-1}$
U_0	zonal velocity	$\alpha_0 H_0 f_0$
M_0	meridional buoyancy gradient	$\sqrt{\alpha_0} f_0$
N_0	vertical buoyancy gradient	$\alpha_0 \sqrt{\mathrm{Ri}_0} f_0$
$k_{\max}$	wavenumber of fastest growing wave	$\sqrt{5/2}/(\sqrt{1+\mathrm{Ri}_0}\alpha_0 H_0)$
$\sigma_{\max}$	growth rate of fastest growing wave	$\sqrt{5/54}/\sqrt{1+\mathrm{Ri}_0} f_0$
Δx	horizontal resolution	$8\pi/k_{\max}/nx$
A_4	biharmonic horizontal viscosity	$U_0 dx^3/20$
A_v	harmonic vertical viscosity	$U_0 dz/200$
λ_u	linear drag coefficient	$0.5\sigma_{\max}$
λ_T	inverse restoring timescale	$2\sigma_{\max}$

Table 3.1: Overview of model parameters.

temperature as the only active tracer and a linear equation of state, thus, temperature and buoyancy are equivalent. In order to test the parameterization for different Ri and α, we vary vertical and meridional buoyancy gradients N_0^2 and M_0^2 to obtain specific values for Ri_0 and α_0 in accordance to

$$\mathrm{Ri}_0 = \frac{N_0^2 f_0^2}{M_0^4}, \qquad \alpha_0 = \frac{M_0^2}{f_0^2}. \tag{3.12}$$

N_0^2 and M_0^2 are used to initialize the temperature field T_0. The initial velocity is chosen to be in thermal wind balance with the initial temperature. A uniform depth of $H_0 = 200\,\mathrm{m}$ and Coriolis parameter of $f_0 = 7 \times 10^{-5}\,\mathrm{s}^{-1}$ are applied throughout all simulations. The domain width is chosen equal in zonal and meridional direction and allows for four wave lengths of the most unstable wave to fit in the domain. Since we use a resolution of 120 grid points in the horizontal, the horizontal resolution varies in dependency on Ri_0 and α_0 (see Tab. 3.1). In contrast, we use a constant vertical resolution of 40 layers and 5 m depth for each experiment.

The described setup is baroclinically unstable and small perturbations that we add to T_0 exponentially grow to eddies which drain their kinetic energy out of the mean state by relaxing the temperature front. In order to obtain an equilibrated scenario, we apply a temperature forcing that counteracts the re-stratification effect. This forcing is achieved by a restoring of the zonal mean temperature $\bar{T}$ to the target temperature T_0 which is identical

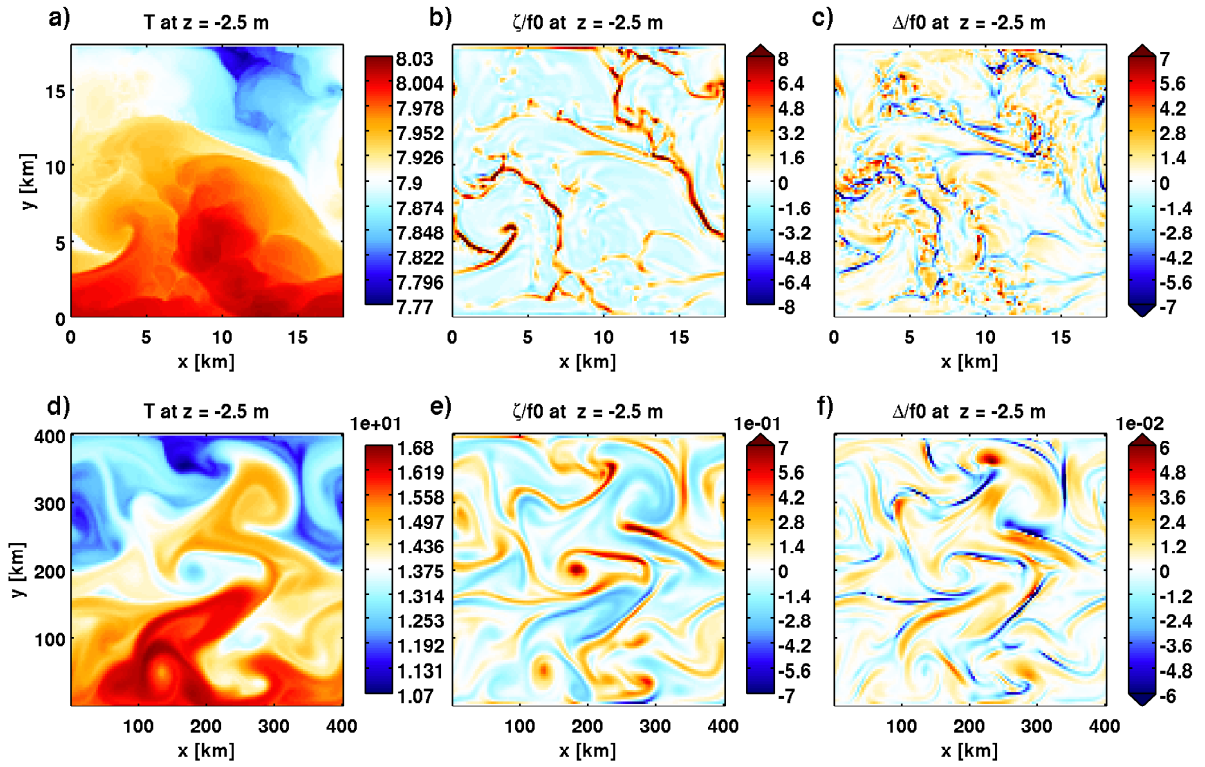

Figure 3.2: Instantaneous horizontal sections of temperature (a, d), vorticity $\zeta = \partial_x v - \partial_y u$ (b, e) and horizontal velocity divergence $\Delta = \partial_x u + \partial_y v$ (c, f), both normalized by f_0, at $t = 160\sigma_{\max}^{-1}$ for an experiment with $\mathrm{Ri}_0 = 1$ and $\alpha_0 = 4$ in (a) - (c) and an experiment with $\mathrm{Ri}_0 = 1000$ and $\alpha_0 = 4$ in (d) - (f).

to the initial condition with an inverse time scale $\lambda_T = 2\sigma_{\max}$, where $\sigma_{\max}$ is the growth rate determined by Eq. (3.5) with Ri_0 and α_0. This means we add a tendency term $\lambda_T(T_0 - \bar{T})$ to the temperature conservation equation in the model. Such kind of restoring has the advantage that the zonal mean front is preserved without damping zonal deviations. In this sense the method is similar to the spectral nudging of Thompson et al. (2006). The restoring is diabatic and yields diapycnal fluxes of buoyancy which are certainly present within the ocean mixed layer, and we consider the zonal restoring as a surrogate for more realistic diabatic processes that would retain a surface buoyancy front in the real ocean.

The instability of the flow yields a conversion of potential energy into eddy kinetic energy. Due to the restoring, there is a permanent source of energy which has to be balanced by dissipation to obtain an equilibrated energy budget. Here, we use a Rayleigh damping of zonal and meridional momentum to extract kinetic energy and to damp the inverse energy cascade at the largest scales. The applied time scale is chosen to be proportional to

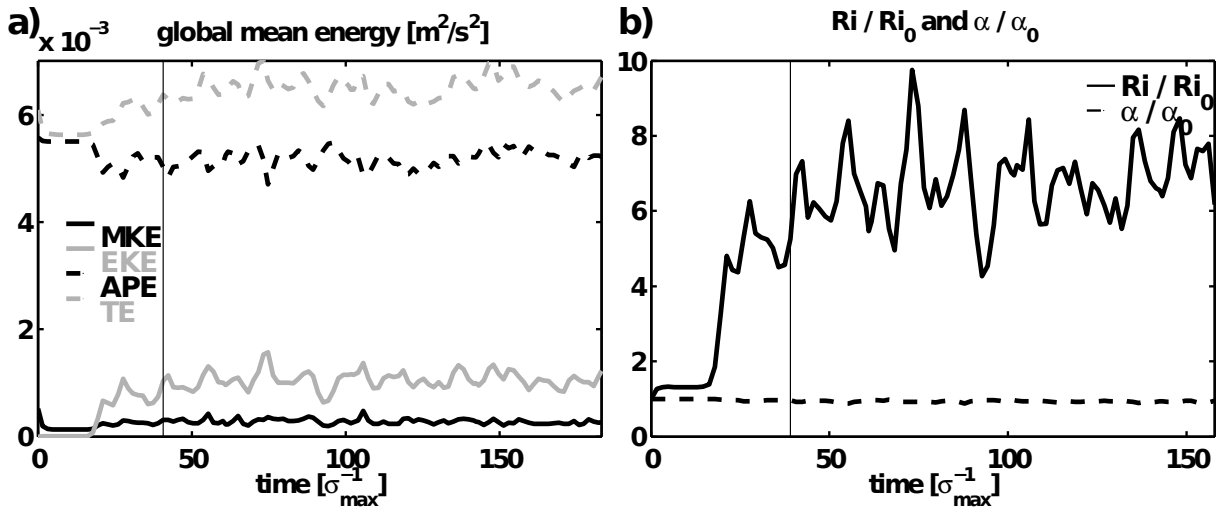

Figure 3.3: (a) Global mean total energy (grey dashed), mean kinetic energy (black solid), eddy kinetic energy (grey solid) and available potential energy (black dashed) as a function of time for an experiment with $\mathrm{Ri}_0 = 1$ and $\alpha_0 = 4$. (b) diagnosed Ri (solid) and α (dashed) normalized by their initial values Ri_0 and α_0 as a function of time. Time is scaled by the initial growth rate $\sigma_{\max}$. Vertical black lines indicate the time point from which time averages are applied (see text).

the maximum growth rate, i.e. the drag coefficient is set to $\lambda_u = 0.5\sigma_{\max}$. In addition to the linear drag, we use biharmonic horizontal and harmonic vertical friction with no-slip boundary conditions at the side walls and free-slip at the bottom (viscosities can be found in Tab. 3.1). Temperature is advected by a third order upwind advection scheme. No explicit diffusion is used, except in statically unstable conditions ($N^2 < 0$), where an implicit vertical diffusion with diffusivity of $1 \times 10^{-2}\,\mathrm{m^2\,s^{-1}}$ parameterizes convection. Since we do not expect hydrostatic effects to become relevant for the parameter range chosen in this study, we use the hydrostatic version of the MITgcm (tests with the non-hydrostatic version do not yield different results).

Snapshots of the equilibrated flow are shown in Fig. 3.2a - c for one simulation dominated by ageostrophic dynamics ($\mathrm{Ri}_0 = 1$ and $\alpha_0 = 4$) and in Fig. 3.2d - f for one with predominantly quasi-geostrophic balanced dynamics ($\mathrm{Ri}_0 = 1000$ and $\alpha_0 = 0.25$). The snapshots of temperature in Fig. 3.2a and d indicate large eddy activity. Typical for ageostrophic dynamics, the simulation with $\mathrm{Ri}_0 = 1$ and $\alpha_0 = 4$ features a relative vorticity $\zeta = \partial_x v - \partial_y u$ shown in Fig. 3.2b which is much larger than f_0 within the spiral-like structured eddies indicating large local Rossby numbers. Within these regions of large relative vorticity, values of the horizontal velocity divergence $\Delta = \partial_x u + \partial_y v$ are of the same order

as ζ (Fig. 3.2c). In the simulation with $\mathrm{Ri}_0 = 1000$ and $\alpha_0 = 0.25$, smaller values of ζ occur and Δ is much smaller than the vorticity (Fig. 3.2e and f), which is typical for a flow in quasi-geostrophic balance.

Fig. 3.3a shows a time series of globally averaged available potential energy APE, eddy kinetic energy EKE, mean kinetic energy MKE and total energy TE = APE+EKE+MKE for $\mathrm{Ri}_0 = 1$ and $\alpha_0 = 4$. APE is defined as the difference between the globally integrated potential energy zb and a minimum potential energy state. For the latter, we adiabatically rearrange the water parcels such that all horizontal gradients vanish and calculate the global mean potential energy of this state. Mean kinetic energy is calculated by $\mathrm{MKE} = 1/2(\bar{u}^2 + \bar{v}^2)$ where $\bar{u}$ and $\bar{v}$ denote zonal averages of the zonal and meridional velocity components u and v, respectively. Eddy kinetic energy is determined by $\mathrm{EKE} = 1/2(u'^2 + v'^2)$, with $u' = \bar{u} - u$ and $v' = \bar{v} - v$.

After a period of approximately $20\sigma_{\mathrm{max}}^{-1}$, the simulation has reached a statistical equilibrium in which the global mean potential and kinetic energy are fluctuating around their time mean value without showing a systematic trend. In Fig. 3.3b, time series of global mean Ri and α are shown, both parameters are scaled by their initial value $\mathrm{Ri}_0 = 1$ and $\alpha_0 = 4$. While there is hardly any change in α, Ri increases by a factor of seven after baroclinic instability sets in. A time average from $t = 40\sigma_{\mathrm{max}}^{-1}$ to $t = 160\sigma_{\mathrm{max}}^{-1}$ (indicated by the vertical black lines in Fig. 3.3) is applied for each simulation to obtain diagnosed values for Ri and α which are used to identify the parameter dependency of the eddy fluxes. For the experiment shown in Fig. 3.3 this yields Ri = 6.9 and $\alpha = 3.7$. Note that the ratio $\mathrm{Ri}/\mathrm{Ri}_0$ becomes smaller in experiments with larger Ri (not shown).

3.3.2 Validating the parameterizations

To investigate the dependency of the eddy fluxes on Ri and α, we perform different experiments by varying the initial and restoring temperature T_0. All other parameters are chosen as detailed in Tab. 3.1. Each experiment is integrated over a time period of more than $150\sigma_{\mathrm{max}}^{-1}$. Time mean values of Ri and α are derived as described in the previous section where we use global and time averages of M^2 and N^2. This time average is performed over a period of more than $100\sigma_{\mathrm{max}}^{-1}$ as indicated in Fig. 3.3 by the vertical black lines and the meridional mean is limited to regions with $y > 0.1L_y$ and $y < 0.9L_y$, where L_y denotes the basin width in order to exclude boundary effects. Eddy fluxes are determined by considering a zonal and time mean of v, w and b and the corresponding deviations to determine $\overline{v'b'}$ and $\overline{w'b'}$. An eddy streamfunction Ψ_{ed} and a diapycnal diffusivity K_{dia} are

calculated from the diagnosed $\overline{v'b'}$ and $\overline{w'b'}$ as

$$\Psi_{\mathrm{ed}} = \frac{\overline{v'b'}\partial_z\bar{b} - \overline{w'b'}\partial_y\bar{b}}{\left|\nabla\bar{b}\right|^2}, \qquad K_{\mathrm{dia}} = -\frac{\overline{v'b'}\partial_y\bar{b} + \overline{w'b'}\partial_z\bar{b}}{\left|\nabla\bar{b}\right|^2}. \tag{3.13}$$

To compare the diagnosed $\overline{v'b'}$, $\overline{w'b'}$, Ψ_{ed} and K_{dia} with the vertical profiles of the parameterizations, we take an additional meridional average of the respective quantities where we again exclude the meridional boundaries as mentioned above.

The parameterizations for $\overline{v'b'}$ and $\overline{w'b'}$ based on the analytic solution of the linear stability problem (ALS) by Stone (1972a) and that of Fox-Kemper et al. (2008) (FFH) are given by Eq. (3.6) and Eq. (3.9), respectively. In addition, we parameterize the eddy fluxes by a third method very similar to ALS, namely a numerical solution of the linearized eigenvalue problem (NLS) for a given background state instead of using the approximative solution by Stone (1972a). In NLS, M^2 and N^2 are allowed to vary vertically. Details on the method can be found in Thomsen et al. (2014). As before for ALS, we scale the eigenvectors by assuming $v' = C_N\sigma_{\max}/k_{\max}$ where $\sigma_{\max}$ and $k_{\max}$ are now determined numerically and C_N is a tuning factor. Since the computational costs of this method are very high it is probably not appropriate to be implemented in a numerical ocean model. Nevertheless, a consideration of NLS enables us to differentiate if differences between diagnosed eddy fluxes and ALS are due to approximations made in Stone (1972a) and how much improvement could be achieved with more accurate eigenfunctions.

We determine C_S and C_F by a least square fit between diagnosed and parameterized eddy fluxes. Since we are aiming to achieve a variation of the eddy fluxes over several orders of magnitude, we apply a logarithmic weighting and therefore minimize $\sum_i(\log_{10}(y_i) - \log_{10}(x_i) - \log_{10}(C))^2$ to obtain the fitting constant $C = C_S$ or $C = C_F$ where y_i denotes the diagnosed $\overline{v'b'}$ and $\overline{w'b'}$ and x_i the parameterized counterpart of ALS or FFH, respectively, for an experiment i characterized by a certain Ri_0 and α_0. With this, we obtain $C_S = 1.1$ and $C_F = 0.15$ for the corresponding parameterizations. Note that Fox-Kemper et al. (2008) find $C_F = 0.06$ for their spin-down simulations, thus a significantly smaller value. In Fig. 3.4, we show the scaled parameterizations for $\overline{v'b'}$ and $\overline{w'b'}$ for the three parameterizations as a function of the diagnosed $\overline{v'b'}$ and $\overline{w'b'}$. The closer the points are to the black diagonal line the better the diagnosed eddy fluxes match their parameterized counterparts. Note that different tuning coefficients would mean a shift parallel to the vertical axis of the points in Fig. 3.4.

In principle, the quality of the single parameterizations might be inferred from the

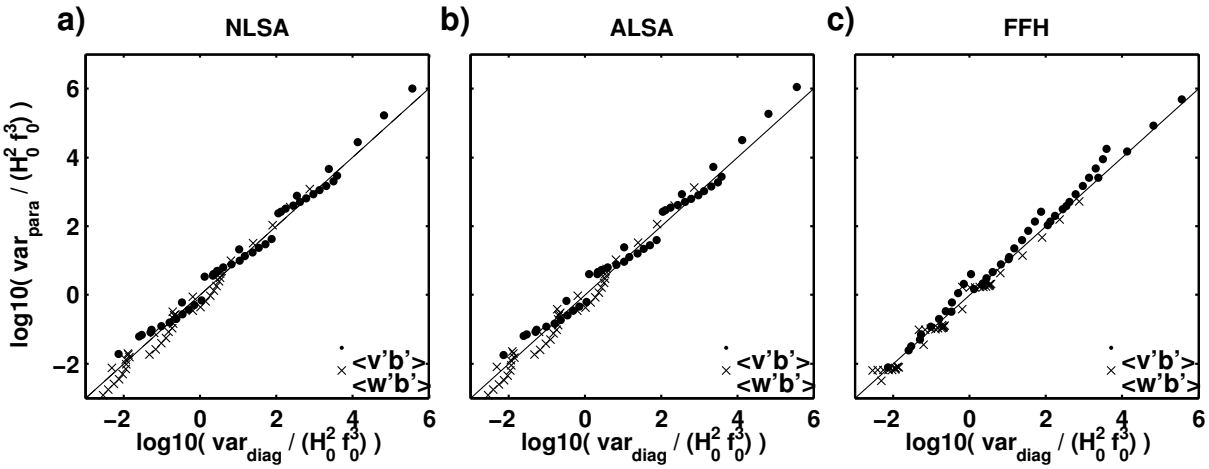

Figure 3.4: (a)-(c) Fitting of the different parameterizations for $\overline{v'b'}$ (dots) and $\overline{w'b'}$ (crosses). Tuning parameters are obtained by a least square fit as $C_S = 1.1$ in (b) and $C_F = 0.15$ in (c).

scatter of the points in Fig. 3.4, but for a more detailed analysis we want to consider the Ri- and α-dependency separately. Plotting the maximum values of the profiles of $\overline{v'b'}$, $\overline{w'b'}$, Ψ_{ed} and K_{dia} against Ri in Fig. 3.5a - d for experiments with $\alpha_0 = 4$ shows the dependency of the eddy fluxes on Ri. A linear regression in these double logarithmic plots yields the exponents κ of the leading order Ri^{κ}-dependency of the eddy fluxes. Similarly, we obtain the leading order α^{λ}-dependency from a set of experiments with $\text{Ri}_0 = 1$ by a linear regression of the eddy fluxes against α in the double logarithmic plots shown in Fig. 3.5e - h. It turns out that there is no qualitative change of the Ri-dependency for experiments with $\alpha_0 = 1$ and $\alpha_0 = 0.25$, and vice versa there is no change of the α dependency for different Ri (not shown).

The slopes determined by the linear regressions for Fig. 3.5 are given in Tab. 3.2. Note that in some cases, the slopes for ALS and FFH do not perfectly agree with Eq. (3.6) and Eq. (3.9), respectively. The reason for that is, that α stays not strictly constant throughout the experiments shown in Fig. 3.5a - d and also Ri slightly varies within the experiments for different α shown in Fig. 3.5e - h. Thus, the eddy fluxes do not only vary due to a change of Ri in Fig. 3.5a - d but also due to slight changes of α, causing the slopes of ALS and FFH to differ from what would be expected for $\alpha = \text{const.}$. The same is true for the slopes determined by the experiments shown in Fig. 3.5e - h. Equation (3.6) suggests for ALS and large Ri a slope of $\kappa = 0.5$ and $\lambda = 3$ for $\overline{v'b'}$ and $\kappa = -0.5$ and $\lambda = 2$ for $\overline{w'b'}$ while Eq. (3.9) suggests for FFH $\kappa = 1$ and $\lambda = 3$ for $\overline{v'b'}$ and $\kappa = 0$ and $\lambda = 2$ for

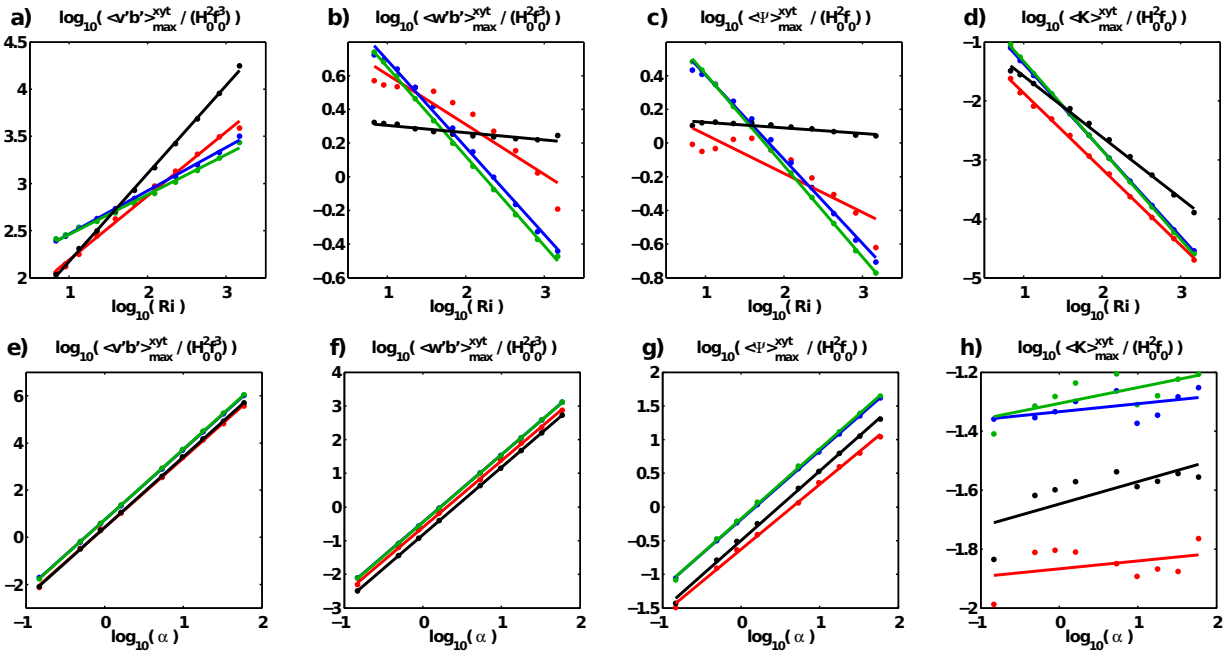

Figure 3.5: Meridional (a, e) and vertical (b, f) eddy fluxes $\overline{v'b'}$ and $\overline{w'b'}$, eddy streamfunction Ψ_{ed} (c, g) and diapycnal diffusivity K_{dia} (d, g) are plotted in (a)-(d) against Ri for simulations with $\alpha_0 = 4$ and in (e)-(h) against α for simulations with $\text{Ri}_0 = 1$. Red dots indicate diagnosed results and blue, green and black dots the corresponding NLS, ALS and FFH parameterizations. Colored lines denote respective linear least square fits. The slopes of these fits in the double logarithmic plots indicate the leading order dependency on Ri in (a)-(d) and the dependency on α in (d)-(h) (slopes are given in Tab. 3.2).

$\overline{w'b'}$. However, as can be inferred by Tab. 3.2, the resulting deviations from the determined slopes to these theoretical slopes for ALS and FFH are rather small.

Despite these issues, it can be noted that the Ri-dependency of the diagnosed eddy fluxes $\overline{v'b'}$ and $\overline{w'b'}$ is not perfectly matched by any parameterization and that the estimated exponents κ for the diagnosed eddy fluxes are in between the FFH and the NLS and ALS parameterizations. Furthermore, the numerical simulations indicate a strong decay of $\overline{w'b'}$ for larger Ri which is in contradiction to FFH. Although the tendency for decreasing $\overline{w'b'}$ with larger Ri is correctly described by the NLS and ALS, the decrease in the numerical model is not as strong as suggested by these parameterizations. For the eddy streamfunction Ψ_{ed} and the diapycnal diffusivity K_{dia}, we obtain similar findings since Ψ_{ed} and K_{dia} are functions of $\overline{v'b'}$ and $\overline{w'b'}$.

Fig. 3.6 shows the vertical structure of the eddy fluxes for $\alpha_0 = 4$ and different Ri. Because there are large variations of the magnitude of the eddy fluxes between the param-

	κ_{diag}	κ_{FFH}	κ_{NLS}	κ_{ALS}	λ_{diag}	λ_{FFH}	λ_{NLS}	λ_{ALS}
$\overline{v'b'}$	0.7	0.9	0.5	0.4	2.9	3.0	3.0	3.0
$\overline{w'b'}$	-0.3	-0.0	-0.5	-0.5	2.0	2.0	2.0	2.0
Ψ_{ed}	-0.2	-0.0	-0.5	-0.5	1.0	1.0	1.0	1.0
K_{dia}	-1.3	-1.0	-1.5	-1.5	0.0	0.1	0.0	0.1

Table 3.2: Estimated dependency of the respective variable on Ri^{κ} and α^{λ}.

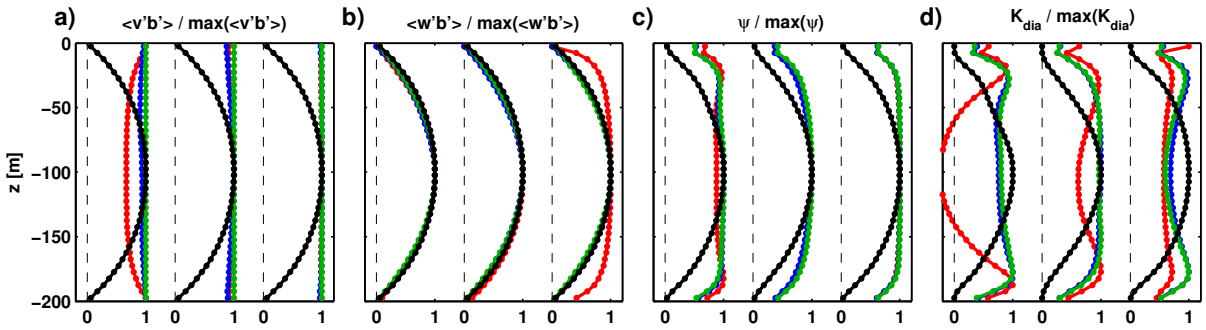

Figure 3.6: Vertical profiles for $\overline{v'b'}$ (a), $\overline{w'b'}$ (b), Ψ_{ed} (c) and K_{dia} (d) for the diagnosed eddy fluxes in red and the FFH, NLS and ALS parameterizations in black, blue and green, respectively. All profiles are normalized by their maximum value and shifted for each experiment while the dashed black lines indicate the respective zero lines. The three experiments are with $\alpha_0 = 4$ but with Ri varying from left to right as $\text{Ri} = 3.2$, $\text{Ri} = 46$ and $\text{Ri} = 1200$.

eterizations, Fig. 3.6 shows all profiles normalized by their maximum values. The diagnosed profiles resemble what we expect from linear stability analysis. While $\overline{v'b'}$ is almost constant in the vertical, $\overline{w'b'}$ has a parabolic vertical dependency with a maximum at mid depth (red lines in Fig. 3.6a and b). The structure of $\overline{v'b'}$ is quite well matched by ALS but does not share the same vertical dependency as predicted by FFH. All parameterizations capture quite well the diagnosed profile of $\overline{w'b'}$. Note that the meridional averaged profiles instead of constant means of M^2 and N^2 are used in NLS.

The profiles of Ψ_{ed} and K_{dia} depend not only on $\overline{v'b'}$ and $\overline{w'b'}$ but also on the vertical structure of M^2 and N^2. While M^2 has nearly no vertical structure, N^2 increases at the top and the bottom (not shown) and therefore influences the structure of Ψ_{ed} and K_{dia}. The resulting profiles are shown in Fig. 3.6c and d. The vertical structure of Ψ_{ed} (red line) is quite well captured by NLS and ALS (blue and green lines) in contrast, the profile of the FFH parameterization decays too strong at the top and at the bottom.

While the structure of K_{dia} is not matched at all by FFH, it is also only partly matched

by ALS and NLS. At top and bottom ALS and NLS closely follow the diagnosed profile but at mid-depth they underestimate the minimum of K_{dia}. Note that K_{dia} becomes negative for small Ri which is probably due to the influence of rotational eddy fluxes. It might also be that the strong mid-depth minimum decreases if the rotational eddy fluxes are subtracted from the total eddy fluxes, such that the profiles of NLS and ALS match better the diagnosed profiles of K_{dia}, but we have made no attempt to do so.

Since the energy conversion between potential and kinetic energy is influenced by the temperature restoring and the linear damping, we test the sensitivity of the Ri-dependency of the eddy fluxes for different restoring time scales λ_T and drag coefficients λ_u. These experiments indicate that these parameters have minor influence on the determined Ri-dependency (not shown). While the effects of variations in λ_T from $\lambda_T = 1.5\sigma_{\max}$ to $\lambda_T = 2.5\sigma_{\max}$ seem negligible with respect to the Ri-dependency, variations of λ_u within the range of $\lambda_u = 0.25\sigma_{\max}$ to $\lambda_u = 0.75\sigma_{\max}$ yield slight variations of the exponents from $\kappa = 0.6$ to $\kappa = 0.7$ for $\overline{v'b'}$ and from $\kappa = 0.2$ to $\kappa = 0.4$ for $\overline{w'b'}$.

3.4 Baroclinic instabilities in a spin-down scenario

3.4.1 Numerical simulations

To simulate mixed layer instabilities at a re-stratifying density front, we choose a setup similar to that used in Fox-Kemper et al. (2008) and Bachman and Fox-Kemper (2013). While Fox-Kemper et al. (2008) directly diagnose the eddy buoyancy fluxes in the spin-down scenario, Bachman and Fox-Kemper (2013) use the eddy fluxes of several passive tracers to estimate a mixing tensor common to all passive tracers, which is assumed to be also representative for buoyancy. This allows the authors to infer the eddy buoyancy fluxes from the diagnosed tensor elements. Here, however, we diagnose the eddy buoyancy fluxes directly as done by Fox-Kemper et al. (2008).

Like in the setup of Sec. 3.3, the model domain consists of a reentrant zonal channel with solid walls at meridional boundaries. To prevent effects from the solid meridional boundaries, we limit the zonal jet and thereby the location where the instabilities grow to a region of width L_f at the center of the channel. This is done by choosing $b_0 = N_0^2(z+H_0) + \frac{L_f M_0^2}{2} \tanh\left(2\frac{y-\frac{L_y}{2}}{L_f}\right)$ where L_y denotes the width of the channel in meridional direction. This initial condition deviates slightly from that considered by Eady (1949) and Stone (1966) who assumed $\partial_{yy} b_0 = 0$ and $\partial_y b_0 = M_0^2$, but we will focus our analysis on

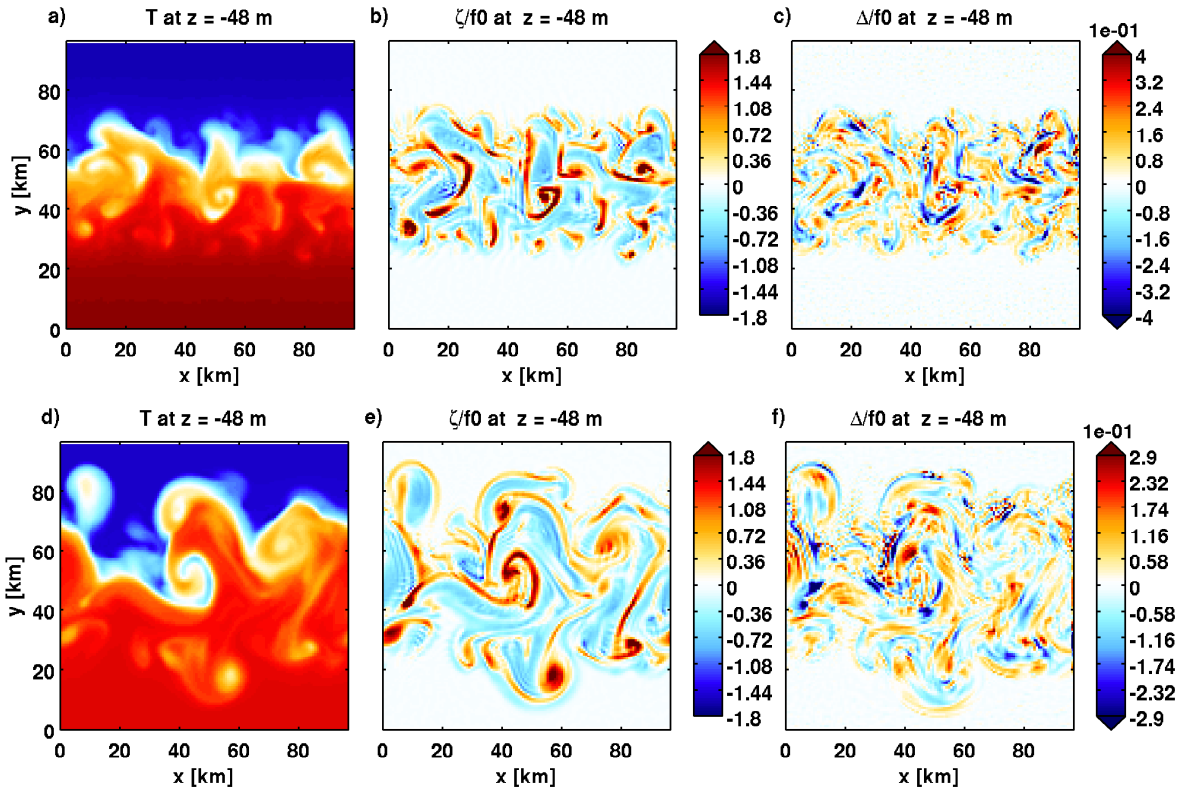

Figure 3.7: (a) Horizontal and (b) vertical snapshots of temperature, (c) vorticity $\zeta = \partial_x v - \partial_y u$ and (d) velocity divergence $\Delta = \partial_x u + \partial_y v$ both normalized by f_0 for an experiment of the spin-down scenario with initial $\mathrm{Ri}_0 = 1$ and $\alpha_0 = 4$ at $t = 17\sigma_{\max}^{-1}$, at the beginning of the averaging period. (e)-(f) Same as in (a)-(d) but at $t = 28\sigma_{\max}^{-1}$, at the end of the averaging period.

the center of the front where these conditions are fullfilled. To dissipate momentum, we use harmonic friction with a viscosity depending on the resolved motion after Smagorinsky (1963) with a "Smagorinsky coefficient" of one which was also used by Fox-Kemper et al. (2008). No-slip conditions are applied at the side walls but free slip at the bottom. No other boundary conditions are used for momentum or density. As before, we use temperature as the only active tracer and a linear equation of state. Due to the numerical dissipation of the applied third order upwind advection scheme, we do not use any explicit diffusion. All simulations for the spin-down experiments are performed with the non-hydrostatic version of the MITgcm although we do not expect non-hydrostatic effects to be relevant for the parameter range considered in this study.

We vary the initial stratification to obtain $\mathrm{Ri}_0 = 1$ to $\mathrm{Ri}_0 = 160$ and $\alpha_0 = 4$ in a first set of experiments. Correspondingly, in a second set of experiments with $\mathrm{Ri}_0 = 1$, we vary

α_0 from $\alpha_0 = 0.2$ to $\alpha_0 = 10$. The horizontal resolution is set to $\Delta x = \pi/(5k_{\max})$ (128 points in x and y) and the vertical resolutions to $\Delta z = 5\,\mathrm{m}$ (60 levels). The basin depth of $H = 300\,\mathrm{m}$ and the Coriolis parameter of $f_0 = 7.29 \times 10^{-5}\,\mathrm{s}^{-1}$ are not varied.

Small white-noise perturbations of $\mathcal{O}(1 \times 10^{-3}\,\mathrm{K})$ in the initial conditions lead to exponentially growing baroclinic instabilities. In contrast to the simulations in the equilibrated scenario, there is no source of potential energy and baroclinic instability induces a slumping of the temperature front by converting all available potential energy (APE) into eddy kinetic energy (EKE). Fig. 3.7 shows that this re-stratification process takes place on a time scale of about $10\sigma_{\max}^{-1}$ which corresponds to a few days for the chosen parameters. As in the equilibrated scenario for $\mathrm{Ri} = \mathcal{O}(1)$, the flow features local Rossby numbers $\zeta/f_0 = (\partial_x v - \partial_y u)/f_0 > 1$ and a normalized velocity divergence $\Delta = (\partial_x u + \partial_y v)/f_0$ of the same order of magnitude. Both indicate ageostrophic dynamics. For larger Ri and therefore quasi-geostrophic conditions, ζ/f_0 is smaller than one and $\Delta \ll \zeta$ (not shown).

Fig. 3.7 shows that the flow field is dominated by large individual eddies and the same is true for the magnitude of the eddy fluxes (not shown). Since the occurrence of single eddy events is a random process, it is necessary to average over these events. In the equilibrated scenario, a temporal mean over some eddy time scales is sufficient to exclude single eddy events but the strong time dependencies in the spin-down scenario rules out this possibility here. Instead, we perform ten ensemble simulations for each experiment characterized by its initial Ri_0 and α_0. Each ensemble member only differs in the small random perturbations added to the initial temperature.

In Fig. 3.8a, we show an ensemble averaged time series of the conversion of APE into EKE by baroclinic instability for an experiment with $\mathrm{Ri}_0 = 1$ and $\alpha_0 = 4$. During the re-stratification phase, the mean kinetic energy (MKE) stays constant until boundary effects become important, suggesting that there is no significant interaction between the eddies and the mean current. Total mechanical energy (TE) is dissipated due to the applied viscous damping. Fig. 3.8b and c show time series of Ri and α, respectively, averaged over the domain. In accordance to the rather small changes in MKE, α, or equivalently the meridional buoyancy gradient, hardly changes. The large increase in Ri soon after the onset of the re-stratification is mainly caused by changes in the vertical stratification.

3.4.2 Validating the parameterizations

In contrast to a quasi-stationary system as considered in Sec. 3.3, a time-dependent system requires slight changes in our analysis to determine the diagnosed and parameterized eddy

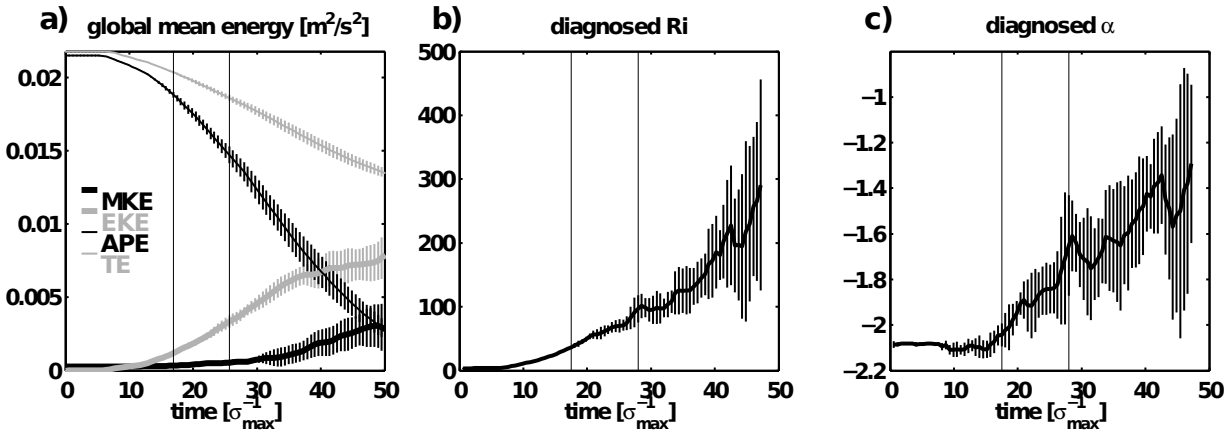

Figure 3.8: Time dependency of global mean total mechanical energy (grey thin line), mean kinetic energy (black thick line), eddy kinetic energy (grey thick line) and available potential energy (black thin line) for an experiment in the spin-down scenario with $\mathrm{Ri}_0 = 1$ and $\alpha_0 = 4$ (a) and time dependency of Ri (b) and α (c). Small vertical lines denote the standard deviation of the ensemble spread. Time is scaled by the initial growth rate $\sigma_{\max}$. Vertical black lines indicate the period over which the time average is taken to diagnose the eddy fluxes (see text for details).

fluxes. Most of the diagnostics described in the following are performed similar as in Fox-Kemper et al. (2008) to allow for a comparison between their and our results. We use a zonal average to estimate mean quantities. By doing so, we obtain eddy fluxes which are two-dimensional and change in time. We furthermore average $\overline{v'b'}$ and $\overline{w'b'}$ over y within the active area of the eddies, because we are interested in the mean effect of the eddies. Thus, the meridional averaging is restricted to the center of the front (all points for which $\overline{M^2} < 0.1 \max(\overline{M^2})$). Finally, we perform an average over ten ensemble simulations.

Such averages over the frontal width of M^2 and N^2 are also performed to diagnose Ri and α given by Eq. (3.12). The diagnosed Ri and α enter Eq. (3.6) and Eq. (3.9) to determine $\overline{v'b'}$ and $\overline{w'b'}$ for ALS and FFH, respectively. For NLS, we calculate $\overline{v'b'}$ and $\overline{w'b'}$ with the use of the horizontally (over the frontal width) averaged vertical profiles of M^2 and N^2. Finally, we calculate the ensemble mean of the diagnosed and parameterized eddy fluxes to eliminate the effect of single eddy events as described above.

Fig. 3.9 shows the time evolution of the vertical maximum of the eddy fluxes for a specific set of ensemble experiments. In the initial phase $\overline{v'b'}$ and $\overline{w'b'}$ are zero as long as the eddies have not reached finite amplitude yet. After a time of roughly $5\sigma_{\max}^{-1}$, $\overline{v'b'}$ and $\overline{w'b'}$ start to increase. While $\overline{w'b'}$ saturates after approximately $15\sigma_{\max}^{-1}$, $\overline{v'b'}$ further

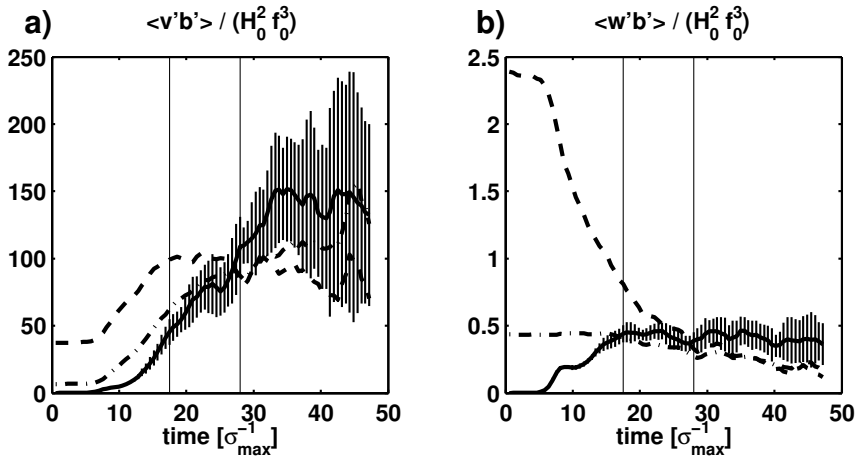

Figure 3.9: Vertical maximum of the eddy fluxes $\overline{v'b'}$ (a) and $\overline{w'b'}$ (b) for an experiment with $\mathrm{Ri}_0 = 1$ and $\alpha_0 = 4$ as a function of time. Solid lines denote the ensemble mean and mean over the re-stratification region (see text for details) while the ensemble means of ALS and FFH are denoted by dashed and dashed-dotted lines, respectively. The small vertical lines indicate the standard deviation over ten ensemble simulations. Time is scaled by the initial growth rate $\sigma_{\max}$ for ALS and FFH, respectively. The period of the re-stratification phase determined as detailed in the text is indicated by vertical black lines.

increases until $30\sigma_{\max}^{-1}$.

Fox-Kemper et al. (2008) restrict their analysis on the re-stratification phase of the eddies. Therefore, they define a time period that starts as soon as the eddies have reached finite amplitude and ends when the eddies reach the meridional boundaries. We also only consider times for which $\overline{v^2} > 0.1U_0$ for half of the mixed layer grid points and where $\frac{\Delta T(t)-\Delta T(t_0)}{\Delta T(t_0)} < 0.03$ with $\Delta T =< T(y = 0.08L_y) - T(y = 0.92L_y) >^{xz}$, denoting the zonally and depth averaged temperature difference near the boundaries and t_0 the initial time. This period is indicated in Fig. 3.8 and Fig. 3.9 by vertical black lines. In the following, we apply time averages over this period to consider the effect of the eddy re-stratification.

To scale the eddy fluxes, we proceed similar as in the equilibrated scenario. As before, we minimize $\sum_i(\log_{10}(y_i) - \log_{10}(x_i) - \log_{10}(C))^2$ with respect to the tuning constant C for each parameterization where y_i denotes the diagnosed $\overline{v'b'}$ or $\overline{w'b'}$ and x_i the parameterized counterpart for an experiment i. We obtain $C_S = 1.2$ and $C_F = 0.1$. Hence C_S is quite similar to the value we obtain for the equilibrated scenario for ALS. In contrast, C_F is slightly smaller than the value we find for the equilibrated scenario but still roughly a factor of two larger in comparison to the value determined by Fox-Kemper et al. (2008) (note that Fox-Kemper et al. (2008) determined C_F by only considering $\overline{w'b'}$ instead of

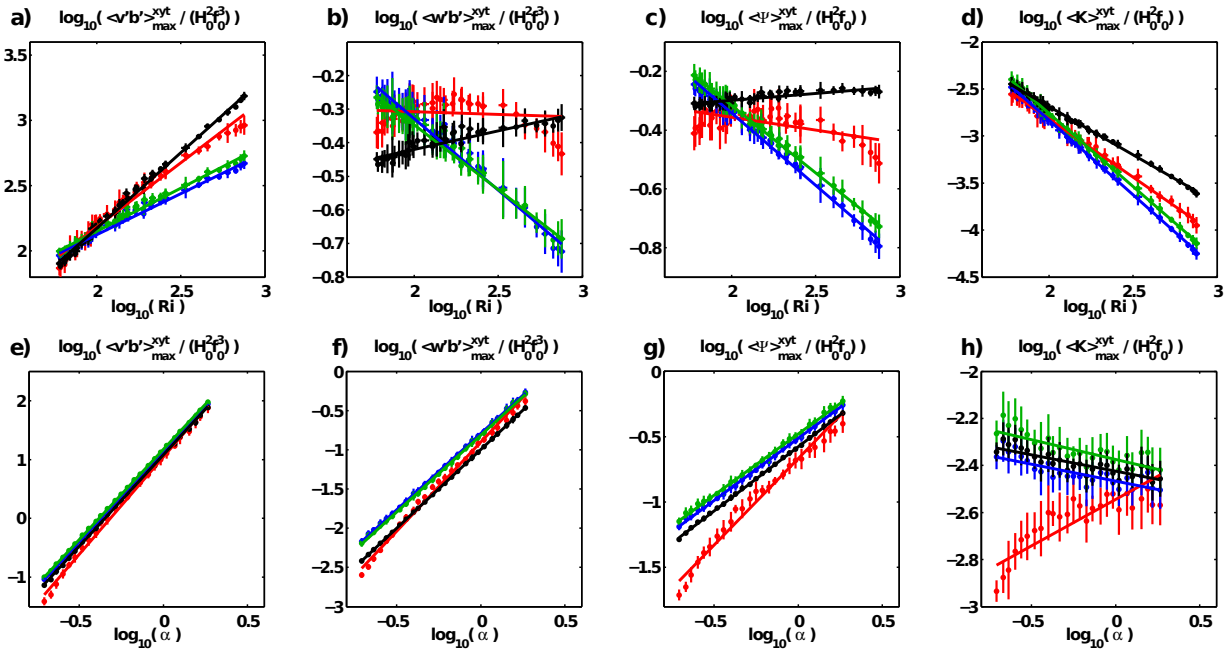

Figure 3.10: Dependency of the horizontal and vertical eddy fluxes $\overline{v'b'}$ (a, d) and $\overline{w'b'}$ (b, e), eddy streamfunction Ψ_{ed} (c, f) and diapycnal diffusivity K_{dia} (d, g) on Ri for $\alpha_0 = 4$ in (a) - (d) and on α for $\text{Ri}_0 = 1$ in (e)-(g) in the spin-down scenario. Red dots denote the ensemble mean of the diagnosed variables, blue of the NLS, green of the ALS and black of the FFH parameterization and crosses indicate the standard deviation of the ensemble spread. Each ensemble consists of ten simulations which deviate only in small random initial perturbations. Straight lines are a least square linear fit as detailed in the text. The slopes of these fits in the double logarithmic plots indicate the leading order dependency on Ri for (a) - (d) and on α for (e) - (h) (values are given in Tab. 3.2).

considering both $\overline{v'b'}$ and $\overline{w'b'}$ as done here).

Fig. 3.10a - d shows the Ri-dependency of the eddy fluxes in the spin-down scenario. The ensemble averaged maxima of the eddy fluxes are shown as a function of Ri for experiments with $\alpha_0 = 4$ and varying Ri_0 from $\text{Ri}_0 = 1$ to $\text{Ri}_0 = 160$. Similar to that, Fig. 3.10e - h shows the dependency of the eddy fluxes on α for a second set of experiments with $\text{Ri}_0 = 1$ and α_0 varying from $\alpha_0 = 0.4$ to $\alpha_0 = 4$. We obtain the exponents κ and λ of the leading order Ri^{κ} and α^{λ} dependency by a least square fit and show them in Tab. 3.3. Note that as before in the equilibrated scenario, the estimated slopes for ALS and FFH slightly differ from what would be expected by Eq. (3.6) and Eq. (3.9), respectively. The reason for this are again slight deviations in α throughout the experiments shown in 3.10a - d and slight variations in Ri within the experiments shown in 3.10e - h.

	κ_{diag}	κ_{FFH}	κ_{NLS}	κ_{ALS}	λ_{diag}	λ_{FFH}	λ_{NLS}	λ_{ALS}
$\overline{v'b'}$	1.0	1.2	0.6	0.7	3.3	3.1	3.1	3.1
$\overline{w'b'}$	-0.0	0.1	-0.4	-0.4	2.3	2.0	2.0	2.0
Ψ_{ed}	-0.1	0.0	-0.5	-0.4	1.3	1.0	0.9	1.0
K_{dia}	-1.2	-1.0	-1.6	-1.5	0.4	-0.1	-0.2	-0.1

Table 3.3: Estimated dependency of the respective variable on Ri^{κ} and α^{λ}.

In the spin-down scenario, FFH tends to better describe the diagnosed eddy fluxes in comparison to NLS and ALS (see Tab. 3.3 for the Ri and α-dependencies and Tab. 3.4 for the mean and maximum deviations). For instance, $\overline{v'b'}$ determined by FFH matches quite well with the diagnosed $\overline{v'b'}$ for the experiments with varying Ri_0 (Fig. 3.10a). However, the decrease of $\overline{w'b'}$ and Ψ_{ed} for larger Ri in Fig. 3.10b and c, respectively, is not captured by FFH. On the other hand, it is too strong in ALS and NLS. Although Fig. 3.10d suggests that K_{dia} is better represented by ALS and NLS, the diagnosed slope of the Ri-dependency is better matched by FFH. As in the equilibrated scenario, the simulations with fixed Ri_0 and varying α_0 shown in Fig. 3.10e - h indicate that both parameterizations predict the correct dependency on α for $\overline{v'b'}$ and $\overline{w'b'}$. Deviations occur only between parameterized and diagnosed Ψ_{ed} and K_{dia}, since all parameterizations seem to overestimate Ψ_{ed} and K_{dia}.

In Fig. 3.11, we show the vertical structure of $\overline{v'b'}$, $\overline{w'b'}$, Ψ_{ed} and K_{dia} normalized by the corresponding maximum value of each profile. Note that again only the global mean values of M^2 and N^2 enter the calculations of $\overline{v'b'}$ and $\overline{w'b'}$ for the FFH and ALS parameterization while the zonally and meridionally averaged profiles of M^2 and N^2 enter the calculations of Ψ_{ed} and K_{dia} and also the calculation of $\overline{v'b'}$ and $\overline{w'b'}$ for NLS. The meridional eddy flux $\overline{v'b'}$ decreases slightly at the top and at the bottom but the decrease is not as strong as suggested by the parabolic structure function for $\overline{v'b'}$ by FFH. There is a better agreement between the constant profile suggested by NLS and ALS and the diagnosed profile in the spin-down scenario, especially for larger Ri. On the other hand, the diagnosed profile for $\overline{w'b'}$ is again well matched by all parameterizations. The diagnosed profiles of Ψ_{ed} and K_{dia} are slightly better matched by NLS and ALS than by FFH.

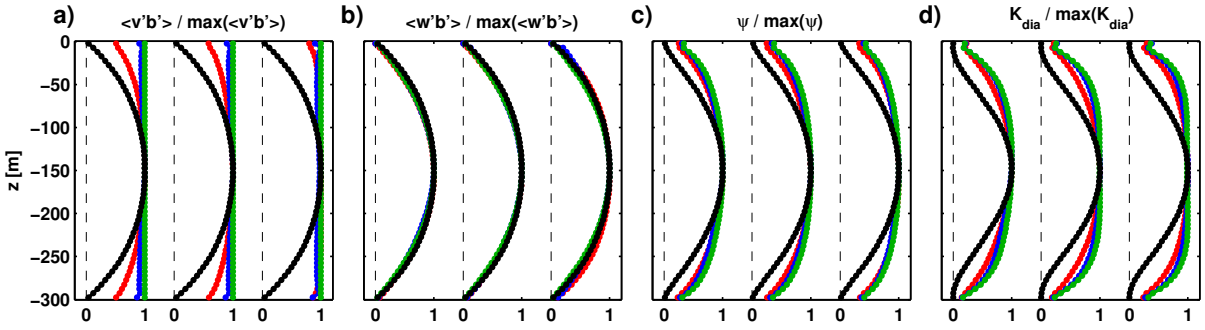

Figure 3.11: Vertical profiles for $\overline{v'b'}$ (a), $\overline{w'b'}$ (b), Ψ_{ed} (c) and K_{dia} (d) for the diagnosed eddy fluxes in red and the FFH, NLS and ALS parameterizations in black, blue and green, respectively. All profiles are normalized by their maximum value while the dashed black lines indicate the respective zero lines. The three experiments are all performed with $\alpha_0 = 4$ but with Ri_0 varying from left to right as $\mathrm{Ri}_0 = 1$, $\mathrm{Ri}_0 = 10$ and $\mathrm{Ri}_0 = 160$.

3.5 Summary and discussion

Mixed layer eddies play an important role in influencing e.g. air-sea gas exchange, surface heat and freshwater fluxes, mixed layer depth and thus biogeochemical cycles. The spatial scales of these eddies and the related mixing processes range from 100 m to 10 km and thus are too small to be resolved by current ocean models. Without accurate parameterization for mixed layer eddies, these models might therefore show a bias. Large velocity shear and low stratification are typical of the dynamics within the mixed layer featuring Richardson and Rossby numbers of order one. Therefore, the flow is not in quasi-geostrophic balance anymore and parameterizations developed for interior quasi-geostrophic dynamics have to be modified.

Stone (1972a), Killworth (1997) and Eden (2011) suggest a parameterization for baroclinic instabilities based on linear stability analysis. Fox-Kemper et al. (2008), however, suggest a competing approach based on a scaling of potential energy release by eddies. The main contradiction between the two approaches lies in a different dependency of the eddy fluxes on background conditions characterized by the Richardson number Ri. Since large variations of Ri occur within the mixed layer, this contradiction can lead to large differences of the predicted eddy fluxes between the two parameterizations. Another difference between both parameterizations is the vertical structure of the meridional eddy flux. While Fox-Kemper et al. (2008) assume a parabolic profile, linear stability analysis suggests a constant vertical profile (Stone, 1972b).

This study aims to clarify to which extent the parameterizations of Fox-Kemper et al.

	equilibrated			spin-down		
	NLS	ALS	FFH	NLS	ALS	FFH
$\overline{v'b'}$	150 (220)	160 (230)	190 (460)	140 (200)	130 (180)	110 (170)
$\overline{w'b'}$	160 (220)	180 (250)	160 (270)	140 (210)	140 (190)	120 (140)
Ψ_{ed}	170 (290)	180 (310)	200 (460)	130 (200)	130 (170)	120 (180)
K_{dia}	230 (350)	240 (400)	370 (630)	130 (210)	120 (160)	150 (220)

Table 3.4: Mean deviations (in %) of maximum amplitudes between parameterized and diagnosed eddy fluxes (maximum devations are given in brackets) for the equilibrated scenario discussed in Sec. 3.3 and the spin-down scenario discussed in Sec. 3.4.

(2008) (FFH) and parameterizations based on linear stability analysis (ALS) are appropriate to predict eddy fluxes within the mixed layer using idealized simulations for a large range of different background conditions and two different configurations. Diagnosing the eddy fluxes for each experiment enables us to examine the functional relationship between the magnitude of the eddy fluxes and Ri and to compare it with the predicted functional relationship of ALS and FFH. Two likely mixed layer scenarios are investigated: an equilibrated flow system with constant shear and stratification and the spin-down of a buoyancy front.

We find that the magnitudes of the parameterized eddy fluxes $\overline{v'b'}$ and $\overline{w'b'}$ and the eddy streamfunction Ψ_{ed} do not deviate from the diagnosed ones by more than a factor of two in the mean and at maximum by a factor of five for Ri varying over three orders of magnitude. Slightly larger deviations can be found for the diapycnal diffusivities in the spin-down scenario but also here the mean deviation is less than a factor of four (see Tab. 3.4 for an overview of the deviations). We conclude that both parameterizations are more or less equally successful in parameterizing the magnitude of mixed layer eddy fluxes. More precisely, we find that the diagnosed eddy fluxes are in between the predictions of both parameterizations for the equilibrated scenario. Likewise in the spin-down scenario, the magnitude of the diagnosed eddy fluxes is somewhere in between the magnitude suggested by FFH and ALS although perhaps slightly better matched by FFH. In any case, FFH does not predict the correct vertical structure of the horizontal eddy fluxes $\overline{v'b'}$. The diagnosed profiles of $\overline{v'b'}$ in both scenarios suggest a constant profile rather than a parabolic shaped one predicted by FFH. This bias in $\overline{v'b'}$ translates to a similar bias in Ψ_{ed} for FFH.

Within this study, we make some assumptions to simplify the diagnostics. There is no consideration of a change of planetary vorticity (β-effect, where β denotes the meridional gradient of the Coriolis parameter f). An influence of β on meso-scale eddies can be ex-

pected as soon as the Rhines scale $L_\beta = \sqrt{2U_{\mathrm{rms}}/\beta}$ becomes smaller than the Rossby radius $L_r = NH/f$ (e.g. Eden, 2007). If we approximate the root mean square velocity U_{rms} by the thermal wind, the ratio between Rhines scale and Rossby radius can be expressed as $L_r/L_\beta = \sqrt{\alpha \mathrm{Ri} H\beta/f}$. Even for the largest Ri and α considered here, this ratio is small for mid-latitude values of f and β and for a water depth H appropriate for the mixed layer. Therefore, we do not expect changes in the planetary vorticity to be relevant for eddy fluxes in the mixed layer at mid-latitudes. For interior dynamics, with large H and probably larger Ri, however, it is reasonable to assume that effects by the planetary vorticity gradient become important and we refer to Eden (2011) and Eden (2012) where linear stability analysis was successfully used to parameterize eddy fluxes for quasi-geostrophic flows including the β-effect.

Another simplification we make in this study is to consider the mixed layer isolated from the abyssal ocean and to apply a solid bottom at the mixed layer base. However, we do not expect large influences of the abyssal circulation on the mixed layer eddy fluxes as long as the increase of N^2 within the pycnocline is large and changes in the vertical shear of the horizontal velocity are small. In these cases, the mixed layer and the interior ocean can be considered as separated regimes. Thomsen et al. (2014) show for a typical situation of a boundary current that NLS suggests two maxima of the growth rate, one corresponding to an interior mode and the other one to the mixed layer mode considered within this study. The eddy fluxes of the mixed layer mode quickly vanish below the mixed layer base as also observed in numerical model studies of Fox-Kemper and Ferrari (2008). However, Badin et al. (2011) show that there can be an influence of mixed layer eddies on lateral tracer mixing within the pycnocline. To account for interactions between the mixed layer and the pycnocline, both parameterizations considered in this study have to be modified. For the parameterization based on linear stability analysis this would mean to derive analytical approximations for more complicated profiles of N^2 and M^2 as in Killworth (1997) and Eden (2012).

Neither of the parameterizations accounts for horizontal changes of N^2 and M^2. As long as these variations occur on scales larger than the mixed layer Rossby radius, the eddy fluxes might be calculated with the varying N^2 and M^2 in a WKB-sense. For variations of N^2 and M^2 on scales at or below the mixed layer Rossby radius, it is not clear whether the parameterizations yield reasonable results, since lateral shear instabilities might have other characteristics than baroclinic instability. Furthermore, we have not accounted for non-hydrostatic effects. Guidance of how these effects might be implemented in ALS can

be drawn from Stone (1971). According to Mahadevan (2006) who does not find major differences between a non-hydrostatic and hydrostatic spin-down simulation for parameters similar to those applied here and in accordance to Stone (1971) who reports that non-hydrostatic effects become relevant only for $\alpha \ll 1$, we do not expect these effects to play an important role for the parameter range considered in this study. Since the thermal wind relation is a basic ingredient to determine the eddy velocity scale, both parameterizations are also not likely to make accurate predictions at the equator.

The fact that we find an acceptable performance of all parameterizations also for large Ri suggests to use the parameterizations also in the ocean interior as a closure for mesoscale eddies. Since some aspects of the simulations performed within this study are quite untypical for quasi-geostrophic mesoscale dynamics, like e.g. large diapycnal eddy fluxes or no change in the planetary vorticity gradient, the results of this study cannot directly be transferred to the deeper ocean. Thus, it remains unclear to which extent the FFH parameterization is able to predict also interior eddy fluxes. The successful implementation and validation of the ALS parameterization for mesoscale eddy fluxes by Killworth (1997) and Eden (2012) and for mixed layer eddy fluxes within this study yields the conclusion that the parameterization based on linear stability analysis is successful to parameterize both, mixed layer and interior eddy fluxes.

3.6 Appendix A: Nondimensionalized equations of motion

We nondimensionalize the inviscid adiabatic Navier-Stokes equations in Boussinesq approximation to identify important characteristic parameters. By using the following scales as in e.g. Stone (1970):

$$t = \frac{L_0}{U_0}\hat{t}, \qquad f = f_0, \tag{3.14}$$

$$(x, y) = L_0(\hat{x}, \hat{y}), \qquad z = H_0\hat{z}, \tag{3.15}$$

$$\partial_z b = N_0^2 \partial_z \hat{b}, \qquad \partial_y b = M_0^2 \partial_y \hat{b} \tag{3.16}$$

$$p = N_0^2 H_0^2 \hat{p}, \qquad b = N_0^2 H_0 \hat{b}, \tag{3.17}$$

$$(u, v) = U_0(\hat{u}, \hat{v}), \qquad w = H_0 f_0 \hat{w}, \tag{3.18}$$

we obtain

$$\mathrm{Ro}D_t u - v' = -\mathrm{RoRi}\partial_x p', \tag{3.19}$$

$$\mathrm{Ro}D_t v + u' = -\mathrm{RoRi}\partial_y p', \tag{3.20}$$

$$\delta^2 D_t w' = -\mathrm{Ri}(\partial_z p' - b'), \tag{3.21}$$

$$\partial_x u' + \partial_y v' + \partial_z w' = 0, \tag{3.22}$$

$$D_t b = 0. \tag{3.23}$$

This set of equations contains three parameters, namely the aspect ratio $\delta = H_0/L_0$, the Rossby number $\mathrm{Ro} = U_0/(L_0 f_0)$ and the Richardson number $\mathrm{Ri} = N_0^2 H_0^2/U_0^2$. While the magnitude of δ determines if non-hydrostatic effects are important, the magnitude of Ri and Ro determines to which extent ageostrophic effects have to be considered.

Note that a slightly different scaling $w = f_0 U_0^2/(N_0^2 H_0)\hat{w}$ and $p = f U_0 L_0 \hat{p}$ was proposed by McWilliams (1985b) and Molemaker et al. (2005). Although this scaling yields a different weighting between the single terms in the Navier-Stokes equations, the resulting set of equations is still sufficiently described by Ri, Ro and δ.

The background flow determines only two parameters Ri and $\alpha = \mathrm{Ro}/\delta$. In order to evaluate the magnitude of the single terms in Eq. (3.19) - Eq. (3.23), an additional assumption on e.g. the length scale L_0 is necessary. Three different assumptions for L_0 are made by different authors:

1. $L_0 = \frac{N_0 H_0}{f_0} = \sqrt{\mathrm{Ri}}\frac{\mathrm{Ro}}{\delta}H_0$, i.e. L_0 is chosen to be the Rossby radius (Molemaker et al., 2005), leading to:

$$\delta = \frac{f_0}{N_0}, \qquad \mathrm{Ro} = \frac{M_0^2}{f_0 N_0}, \qquad \mathrm{Ro}^2\mathrm{Ri} = 1. \tag{3.24}$$

2. $L_0 = \frac{U_0}{f_0} = \frac{\mathrm{Ro}}{\delta}H_0$ (Stone, 1970), leading to:

$$\delta = \frac{f_0^2}{M_0^2}, \qquad \mathrm{Ro} = 1. \tag{3.25}$$

3. $L_0 = \frac{N_0^2}{M_0^2}H_0 = \mathrm{Ri}\frac{\mathrm{Ro}}{\delta}H_0$ (Fox-Kemper et al., 2008), leading to:

$$\delta = \frac{M_0^2}{N_0^2}, \qquad \mathrm{Ro} = \frac{M_0^4}{N_0^2 f_0^2}, \qquad \mathrm{RiRo} = 1. \tag{3.26}$$

Each of these assumptions relates the aspect ratio to the characteristic properties of the background flow N_0^2, M_0^2 and f_0 and it reduces the number of the characteristic parameters of the problem. Since we only consider $\alpha = \mathrm{Ro}/\delta$, these different scalings have no direct influence on the parameterizations Eq. (3.6) and Eq. (3.9) or the prescribed initial conditions of our numerical simulations. However, for identifying which terms in Eq. (3.19) - Eq. (3.23) are relevant for a certain background state, one of the above choices for L_0 has to be made in order to relate Ro and δ separately to this background state.

3.7 Appendix B: Eddy fluxes in the Eady problem

We linearize the quasi geostrophic potential vorticity equation to obtain

$$(\partial_t + U\partial_x)(\nabla_h^2\psi' + \frac{f^2}{N^2}\partial_{zz}\psi') = 0, \tag{3.27}$$

where $\psi' = \bar{\psi} - \psi$ is the perturbation of the horizontal streamfunction ψ with respect to the streamfunction of the background flow, which is given by $\bar{\psi} = -U_0\,(z/H + 1)\,y$ for a zonal flow in thermal wind balance $U = U_0(z/H + 1)$ with amplitude $U_0 = -M^2H/f$, where M^2 denotes a constant meridional buoyancy gradient, H the water depth and f the Coriolis parameter. Using a wave ansatz $\psi' = \phi(z)e^{i(\omega t - kx - ly)}$, we obtain a differential equation for $\phi(z)$:

$$\phi - \frac{H^2}{L_r^2 k_h^2}\partial_{zz}\phi = 0, \tag{3.28}$$

where $k_h = (k^2 + l^2)^{-1/2}$ denotes the horizontal wave number. Equation (3.28) has the solution $\phi = A\cosh(L_r k_h z/H) + B\sinh(L_r k_h z/H)$. The vertical velocity w is derived from ψ by $w = -f/N^2 D_t\partial_z\psi$ which reads in the linearized form:

$$w = -\frac{f}{N^2}[(i\omega - iUk)\partial_z\phi + i\frac{U_0}{H}k\phi]. \tag{3.29}$$

Rigid lid boundary conditions $w = 0$ at $z = 0$ and $z = -H$ yield

$$A = \frac{U_0 k - \omega}{U_0 k}\kappa B, \tag{3.30}$$

$$\frac{\omega}{U_0 k} = \frac{1}{2} \pm i\frac{F(\kappa)}{\kappa}, \tag{3.31}$$

with $F(\kappa) = \sqrt{\kappa \coth(\kappa) - \kappa^2/4 - 1}$ and $\kappa = L_r k_h$. Exponential growth and therefore instability can be expected if $\omega_i = \mathrm{Im}\{\omega\} < 0$, especially the maximum exponential growth rate $\sigma_{\max} = \max(-\omega_i)$ is obtained for $k = \kappa_1/L_r$ and $l = 0$ with $\kappa_1 \approx 1.6$ and $F(\kappa_1) \approx 0.3$ (Eady, 1949).

As soon as the perturbations reach finite amplitude, the exponential growth is inhibited. We assume that this happens if $v' \propto \sigma_{\max}/k_{\max}$ (Killworth, 1997). Therefore, we obtain $B = C\sigma_{\max}/k_{\max}^2$ with a tuning constant C of order one. Hence, we can calculate the meridional eddy fluxes $\overline{v'b'}$:

$$\overline{v'b'} = \frac{1}{2}\mathrm{Re}\left\{-ifk\phi\partial_z\phi^*\right\} = \frac{C^2}{2}\frac{F(\kappa)^3}{\kappa^2}\frac{M^4H^2N}{f^2}, \tag{3.32}$$

and the vertical eddy fluxes $\overline{w'b'}$:

$$\overline{w'b'} = \frac{f^2}{2N^2}\mathrm{Re}\left\{-i\left[(\omega - Uk)|\partial_z\phi|^2 + \frac{kU_0}{H}\phi\partial_z\phi^*\right]\right\} = -\frac{C^2}{4}\frac{F(\kappa)^3}{\kappa}\tanh(\frac{\kappa}{2})\frac{M^6H^2}{N^3f^2}\mu_E(z), \tag{3.33}$$

with the structure function $\mu_E(z)$ that peaks at one and for which we obtain

$$\mu_E(z) = \frac{\cosh\left(\kappa\left(\frac{2z}{H}+1\right)\right) - \cosh(\kappa)}{1 - \cosh(\kappa)}. \tag{3.34}$$

Note that for $z = -H/2$ and for the maximum growth rate with $\kappa = \kappa_1 \approx 1.6$ the eddy flux ratio is $\overline{w'b'}/\overline{v'b'} = -(\kappa_1/2)\tanh(\kappa_1/2)M^2/N^2 \approx -0.53M^2/N^2$.

Chapter 4

Routes to dissipation under different dynamical conditions

This chapter is in preparation for submission

Abstract

In this study, we investigate how ageostrophic dynamics generate an energy flux towards smaller scales. We use numerical simulations of baroclinic instability with varying dynamical conditions ranging from quasi-geostrophic balance to ageostrophic flows. We find that dissipation at smaller scales by viscous friction is much more efficient if the flow is dominated by ageostrophic dynamics than in quasi-geostrophic conditions. In the presence of ageostrophic dynamics, we also observe an energy flux towards smaller scales while energy is transferred towards larger scales for quasi-geostrophic dynamics. Decomposing the velocity field into its rotational and divergent components shows that only the divergent velocity component, which becomes stronger for ageostrophic flows, features a downscale flux. Variation of the dynamical conditions from ageostrophic dynamics to quasi-geostrophic balanced flows shows that the forward energy flux and therefore the small-scale dissipation decreases as soon as the horizontal divergent velocity component decreases. A power law of the dependency of the small-scale dissipation on the Richardson number is estimated for use in future parameterizations.

4.1 Introduction

Turbulent flows in quasi-geostrophic balance show a kinetic energy transfer from smaller to larger scales (Charney, 1971; Rhines, 1977). In contrast, turbulent flows on much smaller scales feature a kinetic energy flux in the opposite direction, i.e. from larger towards smaller scales, where the energy is finally dissipated on molecular scales (Kolmogorov, 1941). On the other hand, most of the energy input into the ocean occurs on scales characteristic for quasi-geostrophic balance, which are much larger than the small-scale regime that features a downscale energy flux. Due to the inverse energy flux on these larger scales, the energy has to be dissipated at the basin scale e.g. by lee wave generation (Bell, 1975; Nikurashin and Ferrari, 2011), a loss of balance resulting from Lighthill radiation of gravity waves (Ford et al., 2000) or by the direct generation of unbalanced ageostrophic instabilities (Molemaker et al., 2005). So far, it is unknown whether such an indirect route to dissipation is efficient enough to balance the energy input into the ocean by wind and tides (Ferrari and Wunsch, 2009). However, numerical model studies from Capet et al. (2008c) and Molemaker et al. (2010) suggest that there is a direct route to dissipation for the energy of the large-scale circulation, since they observe a downscale energy flux for dynamics that are out of geostrophic balance but still have a small aspect ratio. If this downscale energy

flux can be related to the described mechanisms that cause a loss of balance (Ford et al., 2000; Molemaker et al., 2005) is not entirely clear.

The aim of this study is to investigate which dynamical conditions are necessary to generate a downscale kinetic energy flux. Furthermore, we examine if there is a dependency between the strength of this downscale kinetic energy flux and the dynamical characteristics of the flow system. Molemaker et al. (2010) find that a model based on the full Boussinesq equations dissipates substantially more energy at smaller scales than a quasi-geostrophic model does for the same dynamical conditions. They also observe a downscale energy flux featured by the Boussinesq model while in the quasi-geostrophic model, the energy is transferred in the opposite direction towards larger scales as described by Charney (1971). Thus, the occurrence of ageostrophic dynamics seems to play a crucial role for the establishment of a forward energy flux.

To which extent a flow system develops ageostrophic dynamics, strongly depends on its inherent dynamics. A suitable characterization can be given by the Richardson number Ri, which is the ratio of the vertical density stratification and the vertical shear of the horizontal velocity. While a flow with $\mathrm{Ri} < 1$ is unstable with respect to symmetric instabilities and for $\mathrm{Ri} < 0.25$ also to Kelvin-Helmholtz instabilities, instabilities that arise for $\mathrm{Ri} \gg 1$ are mainly in quasi-geostrophic balance (see e.g. Stone (1966)). For $\mathrm{Ri} = \mathcal{O}(1)$, Molemaker et al. (2005) find the dominant unstable mode to be unbalanced to approximately 10% while also additional modes occur which are unbalanced to an even higher degree.

Values of $\mathrm{Ri} = \mathcal{O}(1)$ can be found at the ocean surface with weak stratification or within strong boundary currents with large velocity shears. Simulations of an idealized subtropical, eastern boundary current system by Capet et al. (2008a) and Capet et al. (2008b) reveal sub-mesoscale eddies and filaments out of geostrophic balance in the upper 100 m. Furthermore, Capet et al. (2008c) observe that these unbalanced motions are accompanied by a forward energy flux at spatial scales smaller than the mesoscales (defined by the length scale of the first baroclinic Rossby radius). In contrast, the energy flux is negative at the mesoscales as expected from the theory of geostrophic turbulence (Charney, 1971).

The different directions of the energy fluxes are interpreted by Waite and Bartello (2006) and Lindborg (2006) as a competition between quasi-geostrophic and stratified turbulence. The former features an upscale energy transfer and a characteristic dependency of the kinetic energy spectrum on the horizontal wavenumber of k^{-3} (Charney, 1971). Observations of the atmospheric kinetic energy spectrum from Nastrom and Gage (1985)

indeed show the predicted spectral dependency of k^{-3} at global scales. However, at smaller scales, the energy spectrum flattens and converges to a spectral slope of $k^{-5/3}$. Observations and theoretical studies (see e.g. Lindborg (2006) and references therein) give support to the hypothesis that the $k^{-5/3}$-dependency can be explained by a forward cascade due to nonlinearly interacting gravity waves (Dewan, 1997). Idealized simulations for stratified turbulence indeed feature a downscale energy flux and a $k^{-5/3}$-dependency of the spectral kinetic energy density (e.g. Waite and Bartello, 2004; Lindborg, 2006). In between the regimes of quasi-geostrophic turbulence and stratified turbulence, it is not a priori clear whether the upscale energy flux of the quasi-geostrophic turbulence or the downscale energy flux of the stratified turbulence dominates. Lindborg (2005) finds that a dominant upscale energy transport occurs as soon as the Rossby number of the flow is smaller than 0.1.

A competing approach to explain the different characteristics of the energy spectrum results from surface quasi-geostrophic dynamics (SQG) (Blumen, 1978; Tulloch and Smith, 2009). Numerical simulations with a primitive equation model by Klein et al. (2008) point to a strong resemblance between the surface kinetic energy spectrum and the spectrum of the density variance at the surface as suggested by SQG. On the other hand, Klein et al. (2008) find a strong deviation of the interior dynamics from the surface dynamics. Especially, they observe different characteristics of the interior kinetic energy spectrum than predicted from SQG. Therefore, it is arguable whether SQG dynamics can be used to explain interior flow characteristics (LaCasce, 2012).

In this study, we perform simulations of baroclinic instability in a channel. By varying dynamical conditions of this flow from $\mathrm{Ri} = \mathcal{O}(10^3)$ to $\mathrm{Ri} = \mathcal{O}(1)$, we aim to observe the transition between an upscale energy flux for quasi-geostrophic dynamics to a downscale energy flux for ageostrophic dynamics. An equilibrium in the simulation is achieved by counter-balancing the eddy re-stratification with a restoring of the zonal mean buoyancy towards a target buoyancy. This permanent source of available potential energy parameterizes forcing in the ocean acting on large scales and balances the conversion of available potential energy into kinetic energy by baroclinic production. To achieve an equilibrium, the kinetic energy injected by baroclinic production has to be balanced by some kind of dissipation and we apply two different kinds of kinetic energy dissipation. Momentum dissipation by a linear drag of the zonal mean velocity field acts predominantly on the largest scales. This kind of dissipation is a surrogate of e.g. lee wave generation (Bell, 1975; Nikurashin and Ferrari, 2011), Lighthill radiation of gravity waves (Ford et al., 2000) or ageostrophic instability (Molemaker et al., 2005). On the other hand, dissipation by vis-

cous friction extracts energy predominantly on the smallest resolved scales and is intended to be a parameterization for processes which generate downscale energy fluxes towards molecular scales. The energy dissipation rates due to the large- and small-scale dissipation as well as the spectral energy flux for different Ri are compared to observe differences in the magnitude and direction of the energy flux for quasi-geostrophic and ageostrophic dynamics.

Capet et al. (2008c) find an increase in the forward energy flux for an increasing horizontal resolution of their model and emphasize that it is of major importance to adequately resolve ageostrophic processes. In order to achieve a similar accuracy of the resolution for all dynamical conditions, we choose the horizontal basin scale in dependency on the spatial scale of the dominant baroclinically unstable modes following Stone (1966). Thus, we do not need to increase the number of grid points in the model and always use adequate grid resolution. Another difference of our approach in comparison to Capet et al. (2008c) is that we are able to directly investigate different dynamical regimes isolated from any interference between these dynamics and influences from other processes inherent in any more complex model like that one used in Capet et al. (2008c).

Molemaker et al. (2010) compare the dynamics of the quasi-geostrophic model with that of a Boussinesq model. The present study is an alternative approach to that. Instead of a priori excluding any ageostrophic effects, we allow ageostrophic dynamics in all applied simulations but rather change the dynamical conditions of the investigated flow. In our simulations, it depends on these conditions if ageostrophic processes develop or if quasi-geostrophic dynamics dominate. We are also able to investigate intermediate regimes in between the extrema of ageostrophic flows and flows in quasi-geostrophic balance.

Waite and Bartello (2006); Lindborg (2006) and Deusebio et al. (2013) investigate the transition between stratified and quasi-geostrophic turbulence for the meteorologic context. In all those studies, however, the spatial scale and strength of the kinetic energy source is prescribed. The approach of this study is complementary. We aim to investigate baroclinic instability as one of the main sources of turbulence in the ocean. Therefore, the strength and scale of the kinetic energy source is directly related to the dynamics. By varying Ri throughout different simulations, we examine a wide range of dynamical conditions typical for the ocean meso- and sub-mesoscale regime.

This paper is organized as follows: In Sec. 4.2, we introduce the numerical model and analyze the energy budget in physical and spectral space. An investigation of the energy fluxes under different dynamical conditions can be found in Sec. 4.3. The influence of

these different dynamical conditions on the dissipation is discussed in Sec. 4.4. In Sec. 4.5, we discuss the sensitivity of our results before we end with a summary and conclusion in Sec. 4.6.

4.2 Diagnosing the energy cycle

4.2.1 The numerical model

We use a configuration of the hydrostatic version of the MITgcm (Marshall et al., 1997). The model domain consists of a reentrant channel with periodic boundary conditions in zonal direction and solid walls at the meridional boundaries. Baroclinically unstable conditions are provided by a vertically sheared and stratified background flow that is in thermal wind balance with a constant meridional buoyancy gradient M_0^2 and a constant stratification N_0^2. The parameters N_0^2 and M_0^2 determine the Richardson number Ri_0 as follows:

$$\mathrm{Ri}_0 = \frac{N_0^2 f^2}{M_0^4}, \tag{4.1}$$

where f is the Coriolis parameter. We achieve different Ri_0 and thus different dynamical conditions by varying N_0 for a constant Coriolis parameter $f = 7 \times 10^{-5}\,\mathrm{s}^{-1}$ and a constant meridional stratification $M_0^2 = 4f^2$. Since we use a linear equation of state and only temperature as an active tracer, temperature and buoyancy are equivalent.

Following Stone (1966), the fastest exponential growth rate $\sigma_{\max}$ with respect to the Richardson number for a background state with constant vertical and meridional stratification are given for perturbations with a characteristic length scale L_0. The length scale and growth rate of this fastest growing mode are approximately given by

$$L_0 = 2\pi\sqrt{\frac{2}{5}}\sqrt{1+\mathrm{Ri}_0}\frac{M_0^2}{f^2}H, \qquad \sigma_{\max} = \sqrt{\frac{5}{54}}\frac{1}{\sqrt{1+\mathrm{Ri}_0}}f, \tag{4.2}$$

where H denotes the basin depth that we choose to be $H = 200\,\mathrm{m}$ throughout all simulations. To achieve an adequate resolution for different flow scenarios, we choose the basin width to be $8L_0$ in zonal and meridional direction. Therefore, eight wavelengths of the most unstable baroclinic waves fit in the domain for every chosen Ri_0. We use a resolution of (120 x 120 x 40) grid points in zonal, meridional and vertical direction in each model configuration.

Ri_0	Ri	$\mathrm{Fr}_u/10^{-3}$	$\mathrm{Fr}_\zeta/10^{-3}$	Ro_u	Ro_ζ	Ro_ϵ	N/f	$\mathrm{Re}_4/10^6$
1	20	8.4	84	0.13	1.3	0.064	25	0.87
2	27	6.9	68	0.12	1.2	0.056	28	0.96
4	45	5.2	51	0.11	1.1	0.047	32	1.3
8	64	3.8	37	0.093	0.92	0.038	37	1.4
16	113	2.6	26	0.081	0.79	0.03	44	1.8
32	184	1.8	18	0.068	0.67	0.024	51	2.3
63	325	1.2	11	0.056	0.55	0.018	61	2.7
126	560	0.75	7.2	0.046	0.44	0.014	73	3.1
251	1100	0.45	4.3	0.036	0.34	0.011	89	3.6

Table 4.1: Overview of characteristic parameters: $\mathrm{Ri}_0 = N_0^2 f^2/M_0^4$, $\mathrm{Ri} = N^2 f^2/M^4$, $\mathrm{Fr} = U_{\mathrm{rms}}/(N L_{\mathrm{ke}})$, $\mathrm{Fr}_\zeta = \zeta_{\mathrm{rms}}/N$, $\mathrm{Ro}_u = U_{\mathrm{rms}}/(f L_{\mathrm{ke}})$, $\mathrm{Ro}_\zeta = \zeta_{\mathrm{rms}}/f$, $\mathrm{Ro}_\epsilon = P^{1/3}/(L_B^{2/3} f)$ and $\mathrm{Re}_4 = U_{\mathrm{rms}} L_{\mathrm{ke}}^3/A_4$ where N^2 and M^2 denote time mean values fo the vertical and meridional stratification, U_{rms} and ζ_{rms} the root mean square of the horizontal velocity and vertical vorticity component, respectively, $L_{\mathrm{ke}} = 2\pi \int_0^\infty k^{-1} E_{\mathrm{KE}}\,\mathrm{d}k / \left(\int_0^\infty E_{\mathrm{KE}}\,\mathrm{d}k\right)$ a characteristic length scale, P the energy injection at the basin scale L_B and A_4 the biharmonic viscosity.

The baroclinic eddy field will re-stratify the ocean front. We aim to prevent this frontal collapse by applying a restoring of the zonal mean buoyancy to the initial buoyancy. Therefore, we add the term $\lambda_b(b_0 - \bar{b})$ to the buoyancy tendency where λ_b denotes an inverse time scale of $\lambda_b = 2\sigma_{\max}$, $\bar{b}$ denotes the zonally averaged buoyancy in the model and b_0 a target buoyancy specifying the desired Ri_0 and M_0^2. This zonal mean buoyancy restoring yields a permanent source of potential energy which on the one hand is dissipated by numerical diffusion of the applied third order upwind advection scheme for temperature, and which is transformed into kinetic energy by baroclinic eddies on the other hand. We do not apply any explicit diffusion. However, we increase the diffusivities in case of statically unstable conditions as a parameterization for convection in the hydrostatic simulations.

To achieve a balanced state, the kinetic energy injected by the baroclinic production has to be balanced by an energy sink. Therefore, we choose two sources of dissipation. The first is due to biharmonic horizontal and harmonic vertical friction which are most active close to the grid scale. The second is realized by a linear drag of the zonal mean horizontal velocities which in contrast is most active at the basin scale. The latter is achieved by adding the term $-\lambda_u \overline{\boldsymbol{u_h}}$ to the horizontal momentum equations where λ_u denotes an inverse time scale and $\overline{\boldsymbol{u_h}}$ the zonally averaged horizontal velocity. Since we use free-slip conditions at the side walls and at the bottom, the biharmonic dissipation and the zonal drag are the only sinks of kinetic energy. The magnitude of the dissipation

is adjusted to a certain Ri_0 by choosing the inverse restoring time scale $\lambda_u = 0.5\sigma_{\max}$, the biharmonic viscosity $A_4 = 1.5 \times 10^{-4} M_0^2 H L_0^3 / f$ and the harmonic vertical viscosity $A_v = 1.25 \times 10^{-4} M_0^2 H^2 / f$.

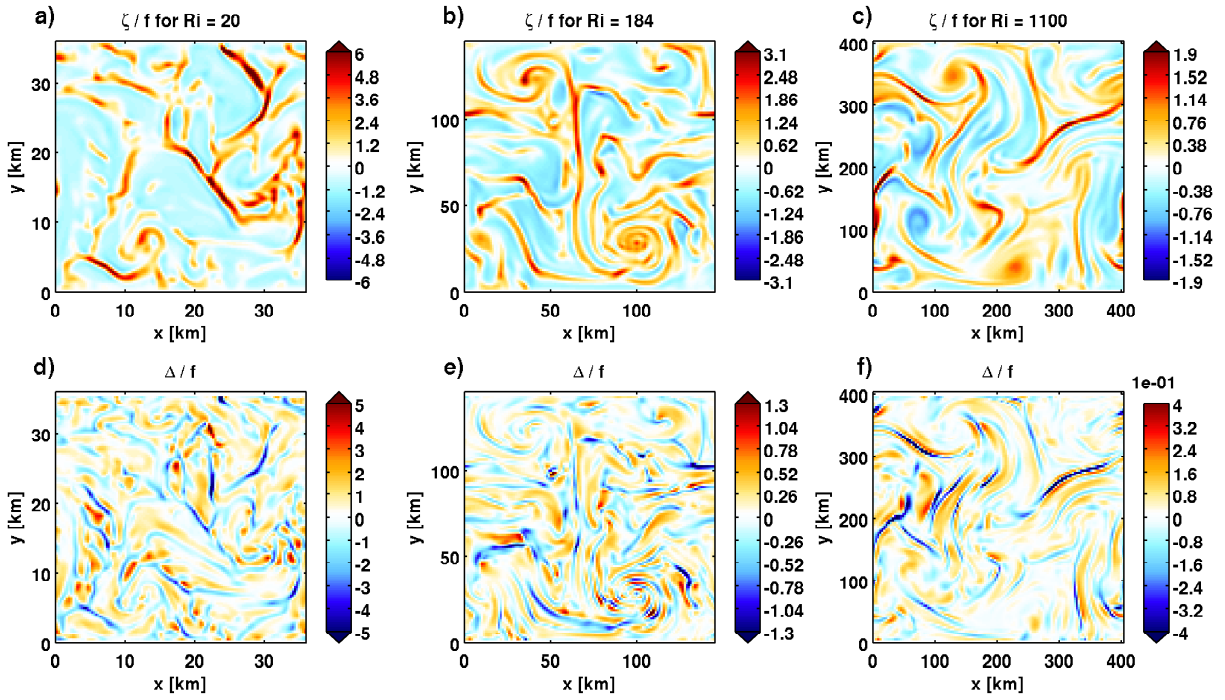

Figure 4.1: Snapshots of surface vorticity (a) - (c) and horizontal divergence (d) - (f), both normalized by f and shown for times after the flow has equilibrated. (a) and (d) show an experiment with Ri = 20, (b) and (e) with Ri = 184 and (c) and (f) with Ri = 1100.

Although we relax zonal mean buoyancy, we observe that the equilibrium stratification differs from the initial stratification and therefore also the mean Richardson number Ri differs from its initial counterpart Ri_0. To take this into account for further diagnostics, we determine the global and time mean values of N^2 and M^2 (see Fig. 4.2 to infer the time averaging period) to calculate a mean Ri and L from Eq. (4.1) and Eq. (4.2), respectively. In Tab. 4.1, we give an overview of important parameters that characterize the flow in the different simulations. We also determine parameters used by e.g. Waite and Bartello (2006) and Lindborg (2005) to characterize their flow dynamics. Considering the criteria of Lindborg (2005) (stratified turbulence occurs above $\mathrm{Ro}_\epsilon \approx 0.1$) or that of Waite and Bartello (2006) (stratified turbulence occurs above $\mathrm{Ro}_u \approx 0.4$ or $\mathrm{Ro}_\zeta \approx 3$), we find that all simulations in Tab. 4.1 are still outside the regime of stratified turbulence. However, the experimental design of this study is not intended to necessarily enter this regime but

rather to investigate the energy flux for baroclinically unstable flow systems typical for the ocean. Since we observe ageostrophic dynamics for our low-Ri experiments that have a major influence on the energy flux (see below), we consider our configuration as adequate.

Snapshots of the vorticity $\zeta = \partial_x v - \partial_y u$ and the horizontal divergence $\Delta = \partial_x u + \partial_y v$ of the equilibrated flow system are shown in Fig. 4.1 for three experiments with different Ri. The experiment with Ri = 20 features large local Rossby numbers ζ/f, especially in the cyclonic spiral shaped eddies (Fig. 4.1a). In addition, large values of Δ indicate strong up- and downwelling that is characteristic for ageostrophic dynamics (Fig. 4.1d). In contrast, the experiment with Ri = 1100 shows lower values of both ζ and Δ indicating dynamics which are close to quasi-geostrophic balance. While the experiments with small Ri might be representative for the ocean mixed layer with weak stratification, or for strong boundary currents[1], larger Ri might be found in weakly sheared near-surface conditions during summer or within the ocean interior.

4.2.2 The energy cycle in physical space

In this section, we analyze differences in the energy dissipation between experiments with ageostrophic dynamics (small Ri) and quasi-geostrophic dynamics (large Ri). For a dominant downscale energy flux for ageostrophic dynamics, we expect the dissipation by the viscous friction to be larger in comparison to experiments with quasi-geostrophic dynamics. The momentum equation in our model is given by

$$\partial_t \boldsymbol{u_h} = -\nabla \cdot \boldsymbol{u u_h} - \boldsymbol{f} \times \boldsymbol{u_h} - \nabla_h p - \lambda_u \overline{\boldsymbol{u_h}} + \boldsymbol{D}_\mathrm{u}, \tag{4.3}$$

where $\boldsymbol{u} = (u, v, w)^T$ denotes the full and $\boldsymbol{u_h}$ the horizontal velocity, $\nabla_h p$ the horizontal pressure gradient divided by a reference density, $\overline{\boldsymbol{u_h}}$ the zonal mean velocity and $\boldsymbol{D}_\mathrm{u}$ the dissipation by the horizontal biharmonic and vertical harmonic dissipation. A kinetic energy (KE) equation is obtained by multiplying Eq. (4.3) with $\boldsymbol{u_h}$, which yields for $K = \boldsymbol{u_h}^2/2$

$$\partial_t K = -\nabla \cdot \boldsymbol{u} K - \nabla \cdot \boldsymbol{u} p + w b' - \boldsymbol{u_h} \cdot \lambda_u \bar{\boldsymbol{u}}_{\boldsymbol{h}} + \boldsymbol{u_h} \cdot \boldsymbol{D}_\mathrm{u}, \tag{4.4}$$

[1]For Ri < 1 different kinds of instability next to baroclinic instability are possible like e.g. symmetric instability, Kelvin-Helmholtz instability (for Ri $< 1/4$) or convective instability for $N_0^2 < 0$. Since these instabilities act to increase Ri up to Ri $= 1$ on very short time and length scales, we restrict our analysis to cases where Ri > 1.

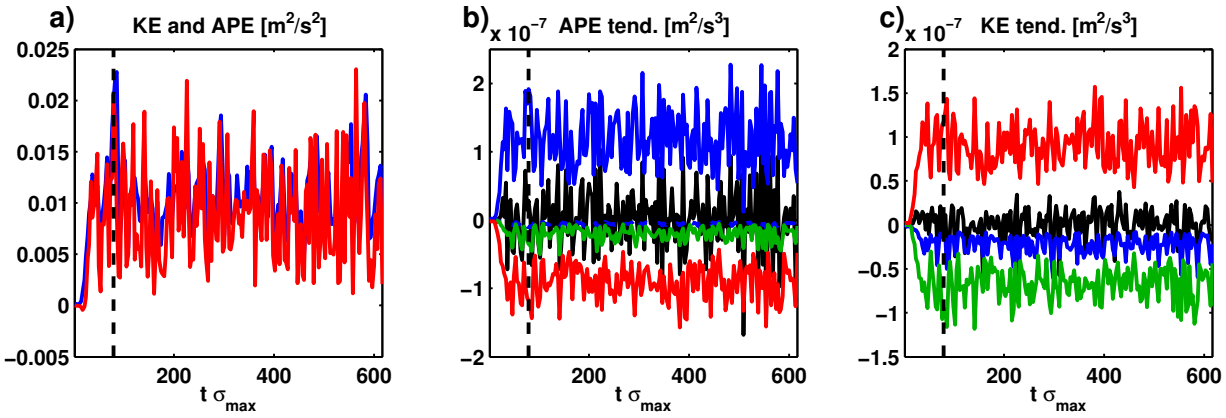

Figure 4.2: (a) Globally averaged KE (blue) and APE (red) as a function of time scaled by the initial maximum growth rate $\sigma_{\max}$ for a simulation with Ri = 20. Note that we have subtracted a constant value of $108\,\mathrm{m^2\,s^{-2}}$ from APE. (b) shows the tendency terms for APE where red denotes the tendency resulting from buoyancy production, green the tendency due to numerical mixing, blue the restoring of the zonal mean and black the total tendency of APE. The convective mixing component is indicated by a blue dashed line but it is negligible in comparison to the other terms in (b). (c) shows the tendency terms for kinetic energy where red denotes the buoyancy production, green the small-scale viscous friction, blue the zonal mean drag and black the total tendency of KE. The vertical dashed black lines in (a) - (c) indicate the averaging period to calculate time mean values of Ri, L and energy budgets or tendencies (see text for details).

where the hydrostatic relation ($\partial_z p = b$) was used and where $p' = p - N_m^2 z^2/2$.

A conservation equation for available potential energy APE can be obtained from the conservation equation of buoyancy

$$\partial_t b = -\nabla \cdot \boldsymbol{u} b + \lambda_b (b_0 - \bar{b}) + D_\mathrm{b}, \tag{4.5}$$

where $\bar{b}$ denotes the zonal mean buoyancy, b_0 a target buoyancy determined by N_0^2 and M_0^2 and D_b numerical diffusion. The latter is related to the third order upwind advection scheme for buoyancy that is known to be responsible for numerical diffusion[2] and convective mixing. Following e.g. Capet et al. (2008c), we determine the former by subtracting the advective tendency of the third order upwind scheme from the tendency of a second order centered advection scheme. We define the available potential energy APE by $P = b'^2/(2N_m^2)$ with $b' = b - N_m^2 z$ denoting the difference between the local buoyancy and

[2]In contrast, we use a centered second order scheme for momentum advection that conserves second order moments. Thus, we do not have to care about numerical dissipation in the kinetic energy budget.

the reference buoyancy $N_m^2 z$ of the global and time mean stratification N_m^2 of the equilibrated flow. The conservation equation for APE is then obtained by multiplying Eq. (4.5) with b'/N_m^2

$$\partial_t P = -\nabla \cdot \boldsymbol{u} P - b' w + \frac{b'}{N_m^2} \lambda_b (b_0 - \bar{b}) + \frac{b'}{N_m^2} D_\mathrm{b}. \tag{4.6}$$

Note that there is an exchange between kinetic and available potential energy by the term $-b'w$ on the right hand side of Eq. (4.6) which we refer to as baroclinic production.

Fig. 4.2a shows a time series of the volume averaged KE and APE. After a period of roughly $20\sigma_{\mathrm{max}}^{-1}$, the initial perturbations have grown to finite amplitude and KE and APE oscillate around their respective mean values. The globally averaged tendencies for APE and KE are given in Fig. 4.2b and c, respectively. The only energy source of the model is the restoring of zonal mean buoyancy (Fig. 4.2b). In the budget for APE it is balanced by two small dissipative sinks due to numerical diffusion and convective mixing and by a large sink due to baroclinic production. The latter acts as an exchange between APE and KE and thus can be found with opposite sign in Fig. 4.2c as a source for KE which is balanced by two sinks of KE, namely, the viscous friction acting primarily on small scales and the zonal mean drag acting primarily on large scales. Note that all other terms of Eq. (4.4) and Eq. (4.6) average exactly to zero in the global integral.

The time mean energy cycle for three simulations with different Ri is shown in Fig. 4.3. The external forcing by zonal restoring feeds the total APE and is balanced in equilibrium by numerical and implicit diffusion and by the buoyancy production term that converts APE into KE. This source of KE, on the other hand, is balanced by sinks due to viscous dissipation and the zonal mean drag. The main difference between the three simulations depicted in Fig. 4.3 is given by the ratio of the two dissipation terms for KE. While KE is dissipated to a much larger extent by the zonal mean drag than by the viscous friction for Ri = 1100, the opposite is the case for smaller Ri, which indicates that for ageostrophic dynamical conditions (small Ri), the energy transport to smaller scales is more efficient in comparison to quasi-geostrophic dynamical conditions (large Ri). This finding emphasizes the hypothesis that the direction of the energy cascade depends on the Richardson number. Note also that there is a large decrease in the rate between APE and KE and a small relative decrease in the dissipation of APE for an increasing Ri.

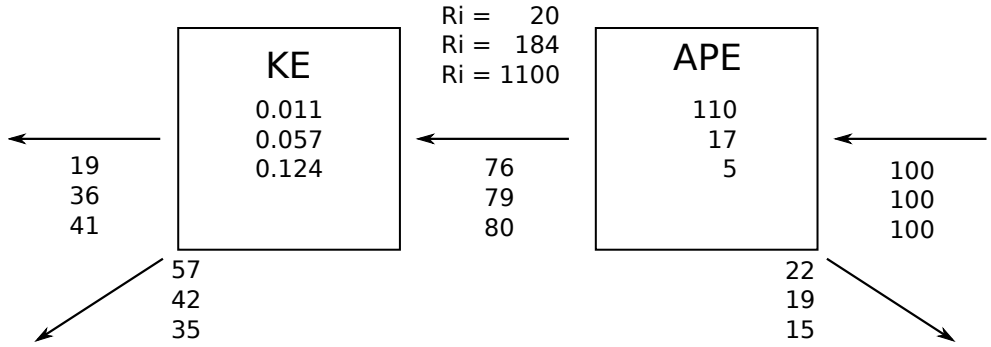

Figure 4.3: Schematic of the energy balances for three simulations with different Ri. The numbers in the boxes denote the volume averaged KE and APE in $\mathrm{kJ\,m^{-3}}$. The ingoing arrows indicate energy sources and outgoing arrows energy sinks due to the tendency terms of Eq. (4.4) and Eq. (4.6). All fluxes are scaled by the energy input due to the zonal buoyancy restoring which is $122 \times 10^{-6}\,\mathrm{W\,m^{-3}}$, $110 \times 10^{-6}\,\mathrm{W\,m^{-3}}$ and $81 \times 10^{-6}\,\mathrm{W\,m^{-3}}$ for the experiments with Ri = 20, 184 and 1100, respectively. More specifically, the arrow between the boxes of KE and APE denotes the tendency due to buoyancy production, the lateral arrows indicate the tendencies due to the zonal mean drag and the zonal mean buoyancy restoring and the diagonal-outward arrows indicate the dissipation by viscous friction for KE and numerical diffusion plus convective mixing for APE. While the tendencies for KE nearly balance each other, there is a small residual in the APE budget.

4.2.3 The energy cycle in wavenumber space

In order to diagnose at which spatial scales the specified energy sources and sinks act, we spectrally decompose the kinetic energy balance and consider equations for the spectral kinetic and available potential energy density E_{KE} and E_{APE}, respectively. We apply a horizontal Fourier transformation to Eq. (4.3) and multiply by $\widehat{\boldsymbol{u}_{\boldsymbol{h}}}^*$, where we denote a Fourier transformed quantity by a caret and its complex conjugated counterpart by a star. After taking a global average, we obtain an equation for the spectral density $E_{\mathrm{KE}} = 1/(2H\Delta k) \int \widehat{\boldsymbol{u}_{\boldsymbol{h}}}^* \cdot \widehat{\boldsymbol{u}_{\boldsymbol{h}}}\,\mathrm{d}z$ (e.g. Frisch, 1995)

$$\partial_t E_{\mathrm{KE}} = \frac{1}{H} \int \left[-\widehat{\boldsymbol{u}_{\boldsymbol{h}}}^* \cdot \widehat{\nabla \cdot \boldsymbol{u}\boldsymbol{u}_{\boldsymbol{h}}} - \widehat{\boldsymbol{u}}^* \cdot \widehat{\nabla p'} + \widehat{w}^* \widehat{b'} - \widehat{\boldsymbol{u}_{\boldsymbol{h}}}^* \cdot \widehat{\lambda_u \bar{\boldsymbol{u}}_{\boldsymbol{h}}} + \widehat{\boldsymbol{u}_{\boldsymbol{h}}}^* \cdot \widehat{\boldsymbol{D}_{\mathrm{u}}} \right] \mathrm{d}z, \quad (4.7)$$

(see Sec. 4.7 for a more detailed derivation). Likewise, we obtain an equation for the spectral density of available potential energy $E_{\mathrm{APE}} = 1/(2N_m^2 H\Delta k) \int \widehat{b'}^* \widehat{b'}\,\mathrm{d}z$ by multiplying the Fourier transform of Eq. (4.5) by $\widehat{b'}^*/N_m^2$ and taking the global average

$$\partial_t E_{\mathrm{APE}} = \frac{1}{N_m^2 H} \int \left[-\widehat{b'}^* \widehat{\nabla \cdot \boldsymbol{u} b'} - \widehat{b'}^* \widehat{w} N_m^2 + \widehat{b'}^* \widehat{\lambda_b (b_0 - \bar{b})} + \widehat{b'}^* \widehat{D_{\mathrm{b}}} \right] \mathrm{d}z. \quad (4.8)$$

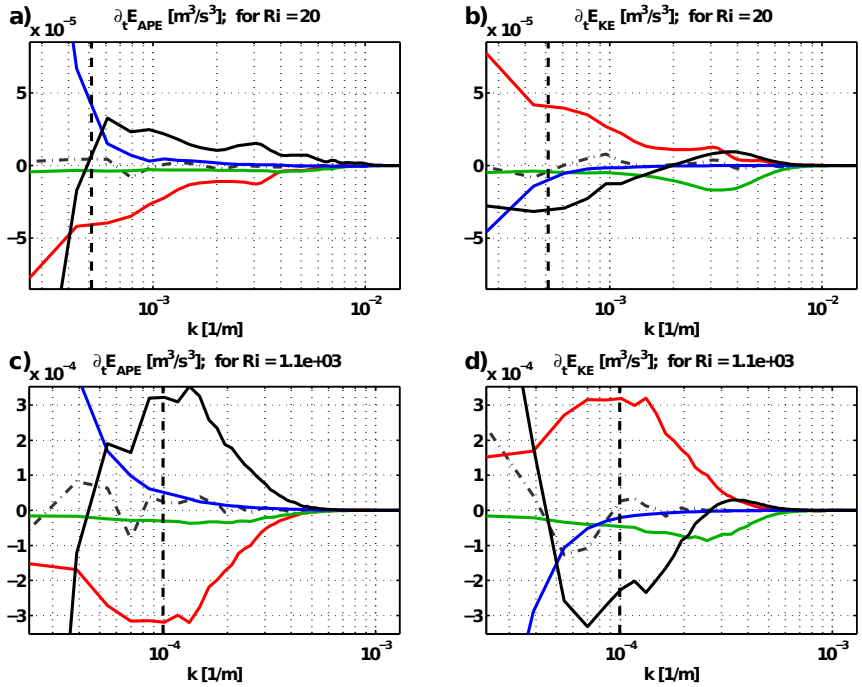

Figure 4.4: Tendencies for E_{APE} (a) and E_{KE} (b) as a function of the horizontal wavenumber $k = \sqrt{k_x^2 + k_y^2}$ for a simulation with Ri = 20. Black curves in (a) and (b) denote tendencies due to advection, red curves denote buoyancy production, green curves denote dissipation due to diffusion in (a) and due to viscous friction in (b), blue curves denote the restoring of zonal mean buoyancy in (a) and the zonal mean drag in (b) and dashed-dotted black lines indicate the sum of all other terms in (a) and (b). (c) and (d) the same as (a) and (b) but for an experiment for Ri = 1100. In addition, the length scale of the fastest growing mode $1/L$ is indicated by vertical black dashed lines in (a) - (d).

Note that all terms in Eq. (4.7) and Eq. (4.8) are real quantities. As in Eq. (4.4) and Eq. (4.6), the buoyancy production $\widehat{b'}^* \widehat{w} = \widehat{w}^* \widehat{b'}$ yields an exchange between E_{KE} and E_{APE} since it occurs with opposite signs in Eq. (4.7) and Eq. (4.8).

Fig. 4.4 shows the budget for spectral kinetic and available potential energy density in correspondence to Eq. (4.7) and Eq. (4.8), respectively. As mentioned above, the only energy source of the model results from the restoring of zonal mean buoyancy which increases APE on the largest scales (see Fig. 4.4a and c). Since dissipation is rather small in the E_{APE} budget, the main loss of E_{APE} results from baroclinic production converting E_{APE} into E_{KE} mainly around the length scale L of the fastest growing unstable baroclinic wave. The tendency due to APE advection is negative on the large forcing scales and positive on the intermediate scales of baroclinic production as can be inferred from Fig. 4.4a

and c. Therefore, the non-linear advection terms in Eq. (4.8) yield a connection between the large spatial scales of the APE source and the scales where baroclinic production transforms APE into KE. While baroclinic production is largest at the Rossby radius in the experiment with Ri = 1100, it reaches its maximum at the largest scales for Ri = 20.

In contrast to the source of APE, which can be found at the largest scales, baroclinic production increases KE on a wide range of scales. In our model, KE can only be dissipated at the large scales by the zonal mean drag and on the smallest scales by viscous dissipation, therefore there has to be a transfer of kinetic energy from the intermediate scales of baroclinic production to either the small or the large scales. Fig. 4.4b shows that in the simulation with Ri = 20, this advection of KE yields a negative tendency of E_{KE} at large and a positive tendency at small scales. Thus, there has to be a downscale kinetic energy flux in this simulations (which will be discussed in the next section). In the experiment with Ri = 1100, advection of KE increases E_{KE} at both large and small scales and decreases energy at the intermediate scales where baroclinic production is most effective. In this case, the corresponding energy flux has to be downscale at the small, but upscale at the large scales. The larger tendencies of the KE advection at large scales indicate that the energy flux is predominantly upscale as might be expected for quasi-geostrophic dynamics.

4.3 Energy fluxes

Fig. 4.3 indicates that an important difference between the dynamics at small and large Ri is the ratio between the small and the large-scale dissipation. Diagnosing the KE budget in spectral space (Fig. 4.4) reveals that advection of KE yields a redistribution of energy from intermediate to either small or large scales. To investigate this energy redistribution in dependency on the Richardson number, we consider spectral energy fluxes[3] caused by the advective terms in the energy budget. The local flux Π of any advected quantity can be derived from the spectral density of its advection term A by $\Pi(k) = -\int_0^k A(k')\,\mathrm{d}k'$. Especially for the kinetic energy Π_{KE} and available potential energy flux Π_{APE}, we obtain

$$\Pi_{\mathrm{KE}}(k) = \frac{1}{H}\int \sum_{k'=k}^{\infty} \widehat{\boldsymbol{u_h}}^* \cdot \widehat{\nabla \cdot \boldsymbol{u}\boldsymbol{u_h}}\,\mathrm{d}z, \qquad \Pi_{\mathrm{APE}}(k) = \frac{1}{H}\int \sum_{k'=k}^{\infty} \frac{1}{N_m^2}\widehat{b'}^* \widehat{\nabla \cdot \boldsymbol{u}b'}\,\mathrm{d}z. \tag{4.9}$$

[3]Note that any interpretation of the energy flux as a local transfer of energy between neighboring scales might be misleading since complex wave-wave (e.g. triade) interactions can be responsible for a non-local energy transfer in wavenumber space.

A comparison of the spectral densities and fluxes of KE and APE as well as for enstrophy $\eta = [(\partial_x v - \partial_y u + f)N^2]^2$ for experiments with different Ri illustrates the results of the previous sections. Fig. 4.5 shows that the slope of the KE spectrum is steeper for larger Ri approaching a value of approximately -3 which is characteristic for geostrophic turbulence (Charney, 1971). For smaller Ri, the slope comes close to a value of $-5/3$ as already observed by Capet et al. (2008c) and Molemaker et al. (2010). However, the theoretical predictions for the spectral slopes are made under the hypothesis that there is an inertial range at certain scales in which all energy sources and sinks vanish. In the present simulations, however, there is no inertial range. Although dissipation acts only on large or small scales in our setup, baroclinic production is active on nearly all spatial scales (see Fig. 4.4). Therefore, one cannot expect in principle the diagnosed slopes to resemble the theoretical expectations assuming an inertial range for both, the KE and the APE spectra.

As in the case of the KE density, we also find important changes of the KE flux for changing Ri (Fig. 4.5 e). For small Ri, the energy flux is positive on all spatial scales and Π_{KE} has a maximum at spatial scales smaller than the length scale L of the fastest growing wave. This maximum decreases when Ri increases while on the other hand, Π_{KE} becomes negative at larger scales with a minimum at scales smaller than L. Thus, we observe an upscale energy flux as expected from quasi-geostrophic turbulence for large Ri and a downscale energy flux similar to stratified turbulence for small Ri. In between these extrema, there is both a downscale flux at smaller and an upscale flux at larger scales. Thus, as soon as ageostrophic dynamics begin to become important, the flow is no longer restricted to transfer energy towards larger scales. Instead, the energy proceeds towards smaller scales providing a direct route to dissipation. These results are in agreement with Capet et al. (2008c) and Molemaker et al. (2010), since both observe a downscale energy flux as soon as ageostrophic dynamics are present and a negative energy flux for dynamics in quasi-geostrophic balance. Here, the transition can be directly related to Ri.

These findings also correspond to results that Lindborg (2006) and Waite and Bartello (2006) obtain for the transition towards stratified turbulence. A comparison of the Rossby numbers Ro and the Froude numbers Fr (Tab. 4.1) of our low-Ri simulations with the values of e.g. Waite and Bartello (2006) suggests that these simulations are at the lower end of their quasi-geostrophic turbulence regime and just about to approach the regime of stratified turbulence. Therefore, it might be argued whether the ageostrophic dynamics in these simulations already cause stratified turbulence although their spectral characteristics are quite similar to those of stratified turbulence.

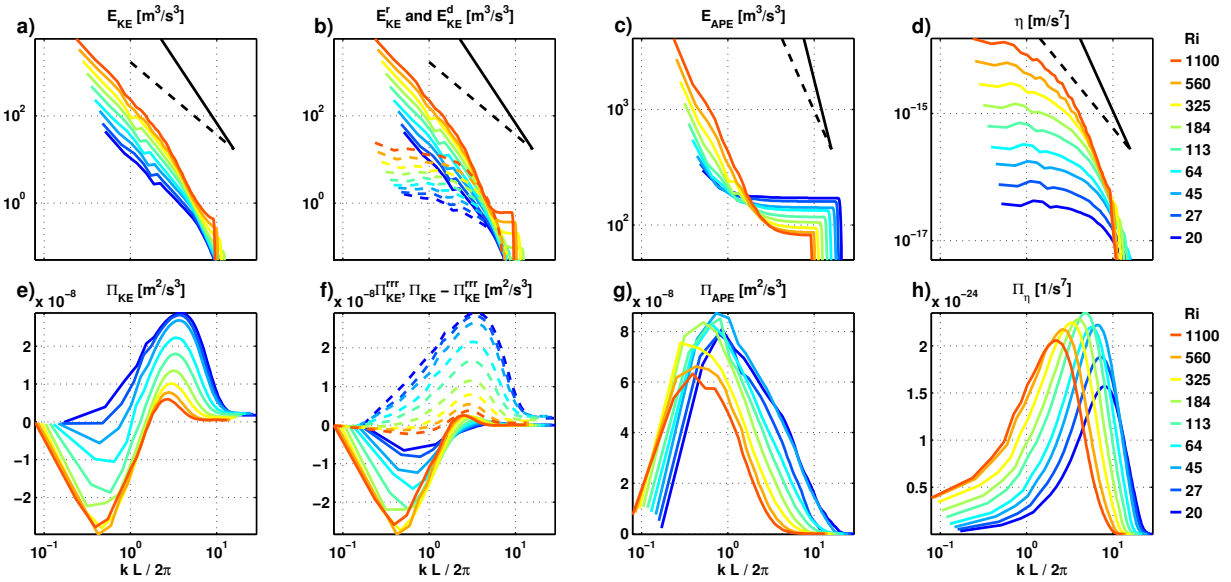

Figure 4.5: Energy and enstrophy spectra (a) - (d) and fluxes (e) - (h) as a function of the wavenumber k scaled by the length scale L of the fastest growing mode for different Ri. Spectra and fluxes for kinetic energy are depicted in (a) and (e), for kinetic energy divided into the rotational component E^r_{KE} and Π^{rrr}_{KE} (solid lines) and the residual component E^d_{KE} and $\Pi_{\mathrm{KE}} - \Pi^{rrr}_{\mathrm{KE}}$ (dashed lines) as defined in Sec. 4.3.1 in (b) and (f), for potential energy in (c) and (g) and for enstrophy in (d) and (h). Different colors of the lines denote experiments with different Ri as indicated by the legend. Black solid and dashed lines in (a) - (d) denote the spectral slopes of -3 and -5/3, respectively.

Fig. 4.5c shows that in the experiments with large Ri the spectral slope of APE is close to -5/3 at larger scales and becomes shallower for smaller scales until diffusion sets in and yields a strong decrease of the APE spectra. For smaller Ri, the part of the spectrum that resembles the -5/3 slope is more and more restricted to the largest scales of the domain and nearly the whole spectrum is flat. Note that Molemaker and McWilliams (2010) as well observe a slight flattening of the APE spectrum on smaller scales, but the decrease of the spectral slope in their simulations is by far not as strong as in ours. In accordance with Molemaker and McWilliams (2010), we find an overall positive flux of APE also for spatial scales and Ri where the KE flux changes its sign.

In contrast to the APE spectra, the enstrophy spectra shown in Fig. 4.5d are shallower at larger scales and steepen towards smaller scales. In consistency with Deusebio et al. (2013), we find that the enstrophy flux is positive for all Ri. Thus, the enstrophy flux is directed towards smaller scales and independent of the direction of the KE flux in all experiments and at all scales. Concerning both the APE and the enstrophy fluxes, we

note that the magnitude of the spectral fluxes are not deviating much between the single experiments. For APE, the maximum of the flux is close to L for small Ri and shifted slightly to larger scales at larger Ri. In contrast, the maximum of the enstrophy flux is at scales slightly smaller than L and shifted further towards smaller scales as Ri decreases.

4.3.1 Rotational and divergent components of the energy fluxes

A more detailed interpretation of the energy fluxes and spectra can be obtained if the velocity $\boldsymbol{u}$ is decomposed into a rotational part $\boldsymbol{u}^r = (u^r, v^r, 0)^T$ and a divergent part $\boldsymbol{u}^d = (u^d, v^d, w)^T$ so that $\partial_x u^r + \partial_y u^r = 0$ and $\partial_x v^d - \partial_y u^d = 0$ (see also Klein et al. (2008), Capet et al. (2008c) and Molemaker et al. (2010)). A decomposition of the spectral kinetic energy density into its rotational component $E^r_{\mathrm{KE}} \equiv 1/(H\Delta k) \int \widehat{\boldsymbol{u_h}}^{r*} \cdot \widehat{\boldsymbol{u_h}}^r \,\mathrm{d}z$ and the residual $E^d_{\mathrm{KE}} \equiv 1/(H\Delta k) \int (\widehat{\boldsymbol{u_h}}^* \cdot \widehat{\boldsymbol{u_h}} - \widehat{\boldsymbol{u_h}}^{r*} \cdot \widehat{\boldsymbol{u_h}}^r) \,\mathrm{d}z$ is shown in Fig. 4.5b. Except for the smallest scales, E^r_{KE} is much larger than the residual E^d_{KE} for all Ri. Furthermore, the rotational part of the energy spectrum has a much steeper slope for all Ri than the residual component (Fig. 4.5b). Note that a spectral slope of -3 would be expected for two dimensional turbulence (Fjørtoft, 1953).

In the same way, the energy flux can be decomposed into one component Π^{rrr}_{KE} that is derived by only considering the rotational velocity $\boldsymbol{u}^r$ in Eq. (4.9) and the residual $\Pi_{\mathrm{KE}} - \Pi^{rrr}_{\mathrm{KE}}$. If decomposed in this manner, the rotational flow can be considered as nearly two-dimensional. Following the argumentation of Fjørtoft (1953), a two-dimensional flow has to satisfy an additional conservation equation, for enstrophy $(\zeta^r)^2 = (\partial_x v^r - \partial_y u^r)^2$ and it thus must obey an inverse energy cascade. In fact, Π^{rrr}_{KE} is negative nearly everywhere in all experiments as can be inferred from Fig. 4.5f. Consequently, any positive part of the kinetic energy flux has to result from components of Π_{KE} that involve the divergent velocity $\boldsymbol{u}^d$. Fig. 4.5f also shows that the residual component $\Pi_{\mathrm{KE}} - \Pi^{rrr}_{\mathrm{KE}}$ is positive for nearly all scales and for all Ri.

The decomposition of the velocity field indicates a sharp separation between the dynamics that is caused by the rotational velocity field and that of the divergent velocity field. The steep kinetic energy spectrum and the upscale kinetic energy flux associated to the rotational velocity is similar to what would be expected for quasi-geostrophic turbulence (Charney, 1971). In contrast, the relatively flat kinetic energy spectrum and the downscale kinetic energy flux related to the divergent flow agrees well with energy spectra and fluxes observed in stratified turbulence (e.g. Lindborg, 2005). For larger Ri, kinetic energy spectra and fluxes seem to be dominated by the rotational part as one would expect for the

limit of quasi-geostrophic dynamics where the velocity is to first order divergence-free. For decreasing Ri the importance of the divergent velocity component increases and changes the main characteristics of the kinetic energy spectrum and flux.

We obtain a more detailed decomposition of the eddy fluxes by inserting $\boldsymbol{u}^r$ and $\boldsymbol{u}^d$ in Eq. (4.9) and considering all components separately. In this case, the kinetic energy flux Π_{KE} is decomposed into eight components Π_{KE}^{abc}, corresponding to each part of the advective momentum tendency $\boldsymbol{u_h}^a \nabla \cdot \boldsymbol{u}^b \boldsymbol{u_h}^c$ where a, b and c denote place holders for r and d and thus indicating either the rotational or the divergent component of $\boldsymbol{u}$. Fig. 4.6a and c show such a detailed decomposition for two simulations with Ri = 20 and Ri = 1100, respectively.

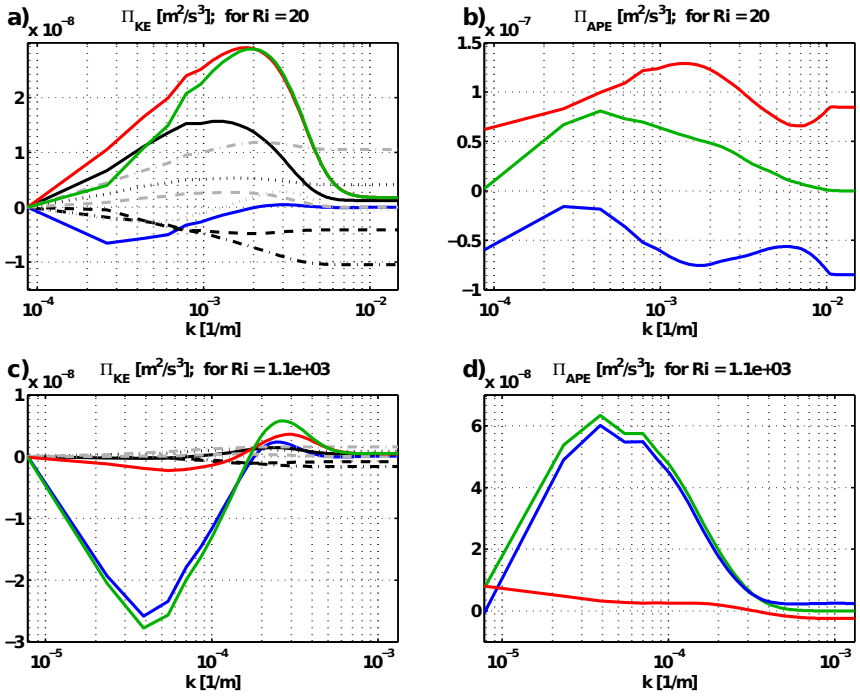

Figure 4.6: (a) and (c) Kinetic energy flux split up into its single components for Ri = 20 in (a) and Ri = 1100 in (c). Green lines denote the total kinetic energy flux Π_{KE}, blue lines the rotational component Π_{KE}^{rrr} and red lines the residual $\Pi_{\mathrm{KE}} - \Pi_{\mathrm{KE}}^{rrr}$. Grey and black lines denote a further decomposition of $\Pi_{\mathrm{KE}} - \Pi_{\mathrm{KE}}^{rrr}$ in Π_{KE}^{rdr} (black solid), Π_{KE}^{drr} (black dashed), Π_{KE}^{ddr} (black dashed-dotted), Π_{KE}^{rrd} (black dotted), Π_{KE}^{drd} (grey dashed), Π_{KE}^{rdd} (grey dashed-dotted) and Π_{KE}^{ddd} (grey dotted). The flux of available potential energy density is shown in (b) for Ri = 20 and in (d) for Ri = 1100. Blue lines denote Π_{APE}^{r}, green lines the total flux and red lines the residual $\Pi_{\mathrm{APE}} - \Pi_{\mathrm{APE}}^{r}$.

As mentioned above, the flux component Π_{KE}^{rrr} that only involves the rotational velocity

is predominantly negative for both simulations. In the simulation with Ri = 1100 (Fig. 4.6 c), it dominates all other components and determines nearly alone the total energy flux. In the simulation with Ri = 20, however, the components including $\boldsymbol{u}^d$ are of the same order of magnitude. Although these components partly compensate each other, their sum has a larger absolute value than Π_{KE}^{rrr} and is positive for all wavenumbers. For all Ri, we find that an important contribution to $\Pi_{\mathrm{KE}} - \Pi_{\mathrm{KE}}^{rrr}$ results from the term Π_{KE}^{rdr}. This term is not only one of the largest of all flux components, it also has a maximum at the same wavenumber as $\Pi_{\mathrm{KE}} - \Pi_{\mathrm{KE}}^{rrr}$.

The flux of available potential energy Π_{APE} can be decomposed with respect to its rotational component Π_{APE}^{r} and its divergent component Π_{APE}^{d}. In this case, Π_{APE}^{r} results from the advection of available potential energy by $\boldsymbol{u}^r$ and Π_{APE}^{d} from the advection by $\boldsymbol{u}^d$. We find that for small Ri the component Π_{APE}^{r} is negative but dominated by Π_{APE}^{d} which is positive, resulting in a net-positive Π_{APE} (Fig. 4.6b). For larger Ri, we observe an increase of Π_{APE}^{r} (not shown). It becomes positive at the larger scales and for even larger Ri positive on all spatial scales. In contrast, Π_{APE}^{d} decreases for increasing Ri and becomes less important compared to Π_{APE}^{r}. Thus, for large Ri, Π_{APE} is almost completely given by its rotational component (Fig. 4.6d).

4.3.2 Unbalanced dynamics as trigger for a forward energy flux

To which extent horizontal divergent motions evolve within a certain flow field can be inferred by considering the horizontal divergence of the friction-less version of Eq. (4.3)

$$\partial_t \Delta = -\boldsymbol{u} \cdot \nabla \Delta - \partial_x \boldsymbol{u} \cdot \nabla u - \partial_y \boldsymbol{u} \cdot \nabla v + f\zeta - \nabla^2 p, \tag{4.10}$$

with $\Delta = \partial_x u + \partial_y v$ denoting the horizontal divergence and $\zeta = \partial_x v - \partial_y u$ the relative vorticity. Thus, a significant local production of Δ occurs as soon as there is an imbalance between the terms on the right hand sight of Eq. (4.10) (McWilliams, 1985a). Similarly to Capet et al. (2008b), we define a parameter ϵ that measures the magnitude of the residual of the terms on the rhs of Eq. (4.10) weighted by the magnitude of the single terms. In contrast to Capet et al. (2008b), we exclude the advective tendency $\boldsymbol{u} \cdot \nabla \Delta$ from the parameter ϵ since the role of this term is restricted rather to a spatial redistribution than a production of Δ. Thus, we define ϵ as:

$$\epsilon = \frac{|-\partial_x \boldsymbol{u} \cdot \nabla u - \partial_y \boldsymbol{u} \cdot \nabla v + f\zeta - \nabla^2 p|}{|-\partial_x \boldsymbol{u} \cdot \nabla u - \partial_y \boldsymbol{u} \cdot \nabla v| + |f\zeta| + |\nabla^2 p| + \mu}, \tag{4.11}$$

where $\mu = f\zeta_{\mathrm{RMS}} + (\nabla^2 p)_{\mathrm{RMS}}$ is added to the denominator in order to prevent locations to be identified as unbalanced where the individual terms on the rhs of Eq. (4.10) are small (see Capet et al. (2008b)).

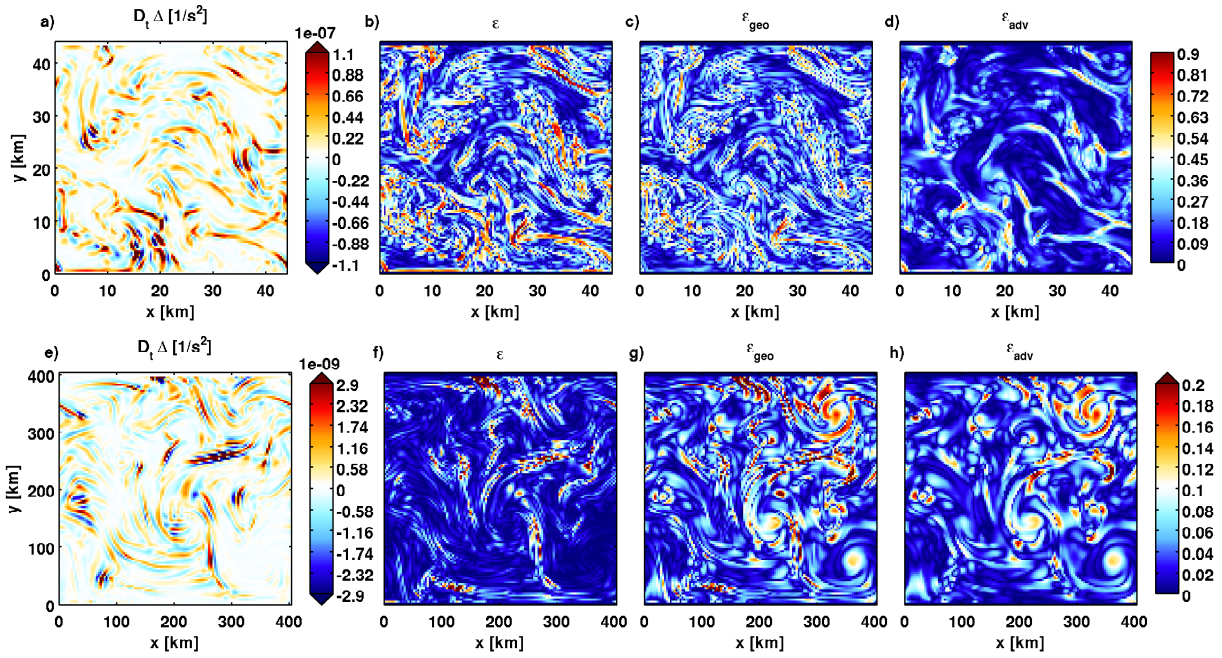

Figure 4.7: (a) Snapshots of the production of horizontal divergence $D_t\Delta$ at the surface for an experiment with Ri = 27. The total deviation from cyclostrophic balance according to Eq. (4.11) is shown in (d), for only the geostrophic terms $f\zeta - \nabla^2 p$ in (c) and for only the advective part $-\partial_x \boldsymbol{u} \cdot u - \partial_y \boldsymbol{u} \cdot v$ in (d). The same is shown in (e) - (h) as in (a) - (d) but for an experiment with Ri = 1100.

In Fig. 4.7a and e, we show the divergence production $D_t\Delta$ with $D_t = \partial_t + \boldsymbol{u} \cdot \nabla$ denoting the material derivative for an experiment with Ri = 27 and an experiment with Ri = 1100. As expected for the low Ri, the divergence production is much larger than for larger Ri. This might also be inferred from ϵ derived after Eq. (4.11). While for Ri = 1100 ϵ indicates hardly any unbalanced flow, for Ri = 27 large regions can be identified, which are out of balance. A decomposition of ϵ into its geostrophic ϵ_{geo} and advective ϵ_{adv} part

$$\epsilon_{\mathrm{geo}} = \frac{|f\zeta - \nabla^2 p|}{|-\partial_x \boldsymbol{u} \cdot \nabla u - \partial_y \boldsymbol{u} \cdot \nabla v| + |f\zeta| + |\nabla^2 p| + \mu}, \tag{4.12}$$

$$\epsilon_{\mathrm{adv}} = \frac{|-\partial_x \boldsymbol{u} \cdot u - \partial_y \boldsymbol{u} \cdot v|}{|-\partial_x \boldsymbol{u} \cdot \nabla u - \partial_y \boldsymbol{u} \cdot \nabla v| + |f\zeta| + |\nabla^2 p| + \mu}, \tag{4.13}$$

shows that the deviation from geostrophic balance dominates the total imbalance ϵ for

Ri = 27. For Ri = 1100 both components seem to cancel each other since they are much larger than the total deviation from balance. Nevertheless, in comparison to the experiment with Ri = 27, the two components are rather small for Ri = 1100.

Following McWilliams (1985b), the tendency of the horizontal velocity divergence Eq. (4.10) is of the order of Ri^{-1}. Thus, the growth of ageostrophic divergent velocity components is directly related to the Richardson number. These considerations suggest a simple relation between the small-scale dissipation and the dynamics of a flow: flows characterized by small Ri feature large divergent velocity components; these, on the other hand, induce a downscale kinetic energy flux that, if strong enough, dominates the total kinetic energy flux. In the case of a substantial downscale kinetic energy flux, a large part of injected kinetic energy has to be dissipated at small scales.

4.4 Dependency of the energy dissipation on the Richardson number

The differences in the energy fluxes for different Ri have a direct influence on the ratio of the large- and small-scale dissipation. If more energy is transferred to larger scales, the large-scale dissipation has to increase and the small-scale dissipation has to decrease in order to achieve an equilibrium. The opposite is the case if more energy is transferred towards smaller scales. Fig. 4.8a shows the tendency terms of the kinetic energy balance due to buoyancy production and dissipation in spectral space normalized by the global mean of the buoyancy production. Except for the experiments with the smallest Ri, the maximum of the energy production occurs at a scale of $k = 1/L$ and slowly decreases at smaller scales. In contrast, energy dissipation is acting as well on the largest scales by the zonal mean velocity drag and on the smallest scales by the viscous friction. In between, the energy dissipation nearly vanishes. Note that the relative small-scale dissipation of kinetic energy increases for increasing Ri, while the large-scale relative dissipation decreases for decreasing Ri.

Fig. 4.8b shows the Richardson dependency of the small- and large-scale kinetic energy dissipation D_s and D_l, respectively, normalized by the kinetic energy source due to baroclinic production B. We define here the small-scale energy dissipation as the global average over the viscous friction and, correspondingly, the large-scale energy dissipation as the dissipation induced by the zonal mean drag. While the large-scale dissipation increases with increasing Ri, the small-scale dissipation decreases. This finding is in good agreement

with the increase of the upscale kinetic energy flux for larger Ri. We obtain an approximative Ri-dependency of $D_l/B = \mathrm{Ri}^{0.23}$ by a least square fit for the large-scale dissipation and of $D_s/B = \mathrm{Ri}^{-0.15}$ for the small-scale dissipation. Note that for the smallest Ri approximately 80% of the kinetic energy injected by baroclinic production is dissipated by the small-scale dissipation and approximately 20% by large-scale dissipation. In contrast, for the largest Ri, approximately 55% result from the large-scale dissipation and 45% from the small-scale dissipation.

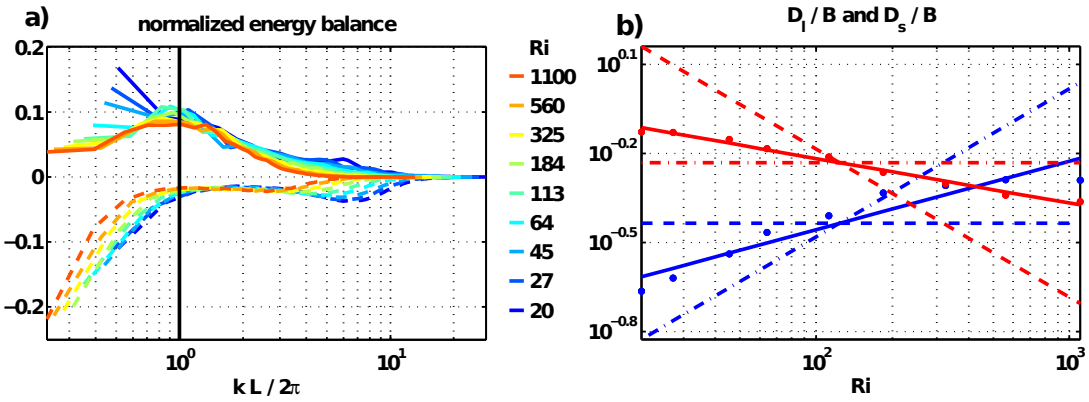

Figure 4.8: (a) Kinetic energy balance for different Ri with respect to the horizontal wavenumber scaled by L. The solid lines indicate the source of kinetic energy due to baroclinic production and the dashed lines indicate the sum of the dissipation due to zonal restoring and viscous friction. All curves are normalized by the global average of the baroclinic production. The black vertical line indicates the wavenumber of the fastest growing mode $2\pi/L$. Small scale dissipation D_s (red) and large-scale dissipation D_l (blue) normalized by the baroclinic production B are shown in (b). Solid lines indicate regression lines in correspondence to the following power laws $D_l/B = 0.1\mathrm{Ri}^{0.23}$ and $D_s/B = 1.2\mathrm{Ri}^{-0.15}$. Red and blue dashed lines indicate fits with Ri^0 and $\mathrm{Ri}^{-0.5}$ for the small-scale dissipation and Ri^0 and $\mathrm{Ri}^{0.5}$ for the large-scale dissipation.

4.5 Sensitivity experiments

Capet et al. (2008c) find a decreasing downscale kinetic energy flux for an increase in the model resolution. This emphasizes the necessity of an adequate resolution for the ageostrophic processes. Dissipation either due to numerical effects or due to any explicit diffusion acts predominantly at the grid scale. If the ageostrophic processes have a comparable scale, they are damped by the dissipation. Especially, the divergent velocities featured by the ageostrophic dynamics are immediately subject to dissipation, if they occur close to the

grid scale. In this case, a low resolution yields a strong interference between dissipation and the ageostrophic dynamics that might dampen a downscale energy flux. As described above, we aim to circumvent this problem by adjusting the resolution to the underlying dynamics and choose the resolution (and domain size) with respect to the length scale of the fastest growing unstable wave for each individual background state. Thus, we assume that the important dynamics which are responsible for the energy flux occur close to this spatial scale. However, in a series of sensitivity experiments, we aim to assure that the results described so far are robust with respect to different resolutions.

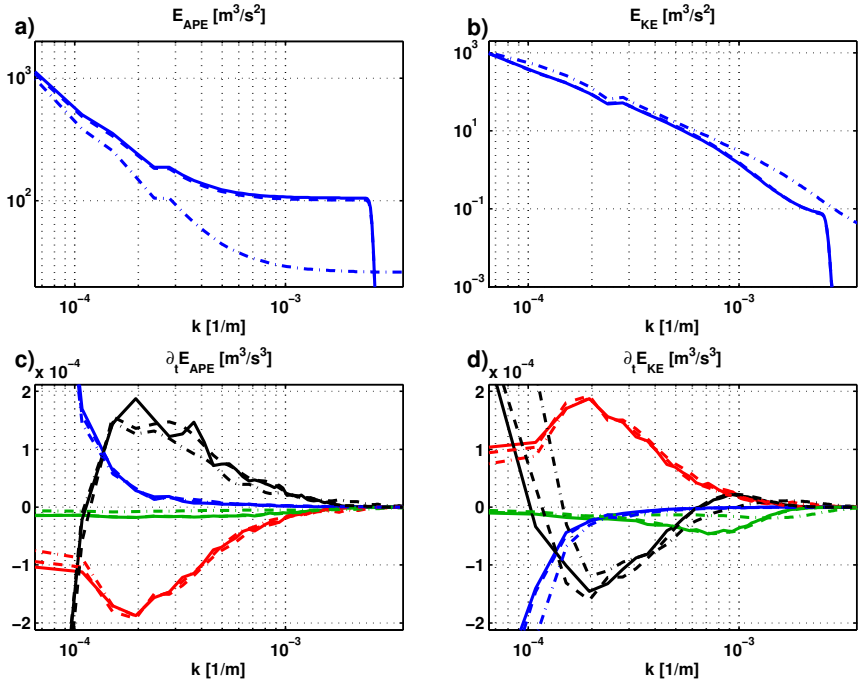

Figure 4.9: APE spectra (a), KE spectra (b) and tendencies for E_{APE} (c) and E_{KE} (d) for simulations with different horizontal and vertical resolution for $\mathrm{Ri}_0 = 200$. The colors are the same as in Fig. 4.4. Solid lines indicate the standard simulation with a resolution of 120 x 120 x 40, the dashed lines indicate a doubled vertical resolution 120 x 120 x 80 (hardly distinguishable from standard simulation) and the dashed-dotted lines a doubled horizontal resolution 240 x 240 x 40.

Fig. 4.9 shows the kinetic and available potential energy spectra E_{KE} and E_{APE}, respectively, as well as their tendencies in wavenumber space for different vertical and horizontal resolutions and an intermediate Ri (the same is found for large and small Ri). Doubling the vertical resolution from 40 to 80 layers yields hardly any changes of the spectra and tendencies. For a doubled horizontal resolution of 240 x 240 grid points, the main charac-

teristics are also similar to the counterparts with lower resolution. However, some minor differences can be observed. Higher horizontal resolution also allows to use smaller horizontal viscosity and we choose this in order to achieve a comparable grid Reynolds number for all simulations. This smaller viscosity yields a shift of the dissipation towards smaller scales as can be inferred from Fig. 4.9d. Therefore, the decrease of the spectral kinetic energy, that is induced by dissipation at small scales, is also shifted towards smaller scales for the simulations with higher horizontal resolution. In the higher resolved simulation, the slope of E_{APE} is steeper at the large and intermediate scales in comparison to the standard simulation.

Fig. 4.10 shows the small-scale dissipation rate D_s normalized by the total amount of buoyancy production B for the standard simulations shown in Fig. 4.8b as well as for simulations with higher resolution. As for the local balances shown in Fig. 4.9, a doubling of the vertical resolution has nearly no effect on D_s. By contrast, doubling the horizontal resolution yields a stronger decay of D_s with larger Ri. While there is hardly any difference for the simulations with $\mathrm{Ri} \approx 20$, a doubling of the resolution yields roughly 30% smaller D_s at $\mathrm{Ri} \approx 1000$. Thus, we find some quantitive implications on the small-scale dissipation rate by doubling the horizontal resolutions, even though there are hardly any major qualitative differences.

Another parameter that might influence the dissipation rate is the meridional buoyancy gradient M_0^2 of the restoring target. So far, we only varied N_0^2 for a fixed $M_0^2 = 4f^2$ to obtain a restoring buoyancy target in correspondence to the background Richardson number $\mathrm{Ri}_0 = N_0^2 f^2 / M_0^4$. Fig. 4.10 also shows simulations for one set of different Ri_0 with $M_0^2 = 0.25 f^2$ and another set with $M_0^2 = 16 f^2$. Although a change of M_0^2 changes the total energy content and energy dissipation (not shown), there are hardly any changes concerning the small-scale dissipation rate normalized by the buoyancy production. Thus, for the simulations performed within this study, the meridional shear is only important for the absolute magnitude of the energy dissipation, but as long as it does not change the Richardson number (e.g. a smaller M_0^2 is compensated by a smaller N_0^2), it has no qualitative influence on the dynamics.

As discussed above, the vigorous re-stratification of the eddies is responsible for a larger mean Richardson number Ri in comparison to the initial Richardson number Ri_0. For instance, a simulation in the standard configuration with $\mathrm{Ri}_0 = 1$ yields a mean Ri of $\mathrm{Ri} = 20$. To also obtain simulations with $\mathrm{Ri} = \mathcal{O}(1)$, we increase the restoring time scale λ_b from $\lambda_b = 2\sigma_{\max}$ to $\lambda_b = 64\sigma_{\max}$ (λ_b is still roughly 40 times larger than the time

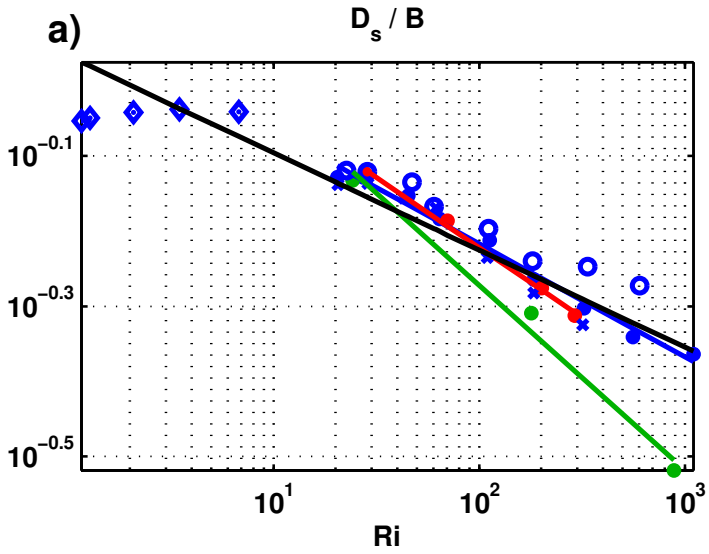

Figure 4.10: Globally averaged small-scale energy dissipation normalized by the globally averaged buoyancy production as a function of Ri for different sensitivity experiments. The blue dots indicate the simulations for different Ri_0 in the standard configuration with (120 x 120 x 40) grid points, $M_0^2/f^2 = 4$ and $\lambda_b = 2\sigma_{\max}$. Simulations indicated by red and green dots deviate from the standard simulation by a doubled vertical (120 x 120 x 80) and a doubled horizontal (240 x 240 x 40) resolution, respectively. Crosses indicate simulations in standard configuration but with $M_0^2/f^2 = 0.25$ and circles with $M_0^2/f^2 = 16$. Diamonds denote non-hydrostatic simulations with a larger restoring time scale of $\lambda_b = 64\sigma_{\max}$ and restoring buoyancy targets corresponding to Ri_0 between 0.1 and 4 and $M_0^2/f^2 = 4$. The black solid line indicates a power law fit to all simulation for which a linear regression yields $D_s/B = \mathrm{Ri}^{-0.13}$. Blue, green and red solid lines indicate fits to the simulations with standard ($D_s/B = \mathrm{Ri}^{-0.15}$), doubled vertical ($D_s/B = \mathrm{Ri}^{-0.19}$) and doubled vertical ($D_s/B = \mathrm{Ri}^{-0.25}$) resolution, respectively.

step of the model). This larger restoring time scale yields a stronger compensation of the buoyancy production by a larger source of potential energy and thus reduces the deviations between Ri_0 and Ri. A set of experiments with Ri_0 varying from $\mathrm{Ri}_0 = 0.1$ up to $\mathrm{Ri}_0 = 4$ indeed features much smaller mean Richardson numbers, ranging between $\mathrm{Ri} = 1.2$ and $\mathrm{Ri} = 6.8$.

The dissipation rate throughout these experiments is nearly constant as can be inferred from Fig. 4.10. This can be explained with a saturation of the small-scale energy flux at a critical Richardson number. At this Ri, nearly all energy is transferred towards smaller scales where it is dissipated. For instance, for the simulations with increased λ_b, roughly 90% of the energy injected by buoyancy production is dissipated by the small-scale

dissipation. Since we find a downscale energy flux on all scales for these experiments (not shown), only such an amount of energy can be dissipated at large scales which is directly injected at these scales. Note that the baroclinic production has its maximum at the largest scales in the experiments with smaller Ri as can be inferred from Fig. 4.8. Therefore, it might not be astonishing that still roughly 10% of the baroclinic production is dissipated by the large-scale dissipation.

4.6 Summary and conclusions

In this study, we show how different dynamical conditions influence the direction of the energy flux in wavenumber space. We use different numerical model configurations of a baroclinically unstable flow system to mimic a large range of dynamical conditions. Our model is forced by a restoring of zonally averaged buoyancy, which yields a large-scale source of available potential energy and prevents a re-stratification of the inclined buoyancy surfaces. Energy sinks result from a zonal mean drag as a large-scale sink of kinetic energy, and viscous friction, which acts predominantly on the smallest scales. Determining the relative strength of the small-scale dissipation with respect to its large-scale counterpart gives information about the efficiency of the flow to feature a downscale energy flux. In addition, we calculate spectral energy densities and fluxes and consider the energy cycle of the model in physical and spectral space to obtain a detailed understanding of the routes to dissipation in a baroclinically unstable flow.

Consistent with other studies (e.g. Lindborg, 2005; Waite and Bartello, 2006; Capet et al., 2008c; Molemaker et al., 2010), we find an upscale kinetic energy flux for dynamics in quasi-geostrophic balance and a downscale energy flux as soon as ageostrophic processes are about to become important. While an upscale energy flux is characteristic for geostrophic turbulence (Charney, 1971), the downscale flux might be interpreted as a result of stratified turbulence (Lindborg, 2006). In fact, dimensionless parameters like Froude or Richardson numbers derived from our simulations with a downscale kinetic energy flux indicate, that these simulations get close to the parameter regime that Lindborg (2005) and Waite and Bartello (2006) identify to be characteristic for stratified turbulence. The downscale flux of kinetic energy in the experiments with ageostrophic dynamics comes along with large dissipation rates at the smallest resolved scales by the viscous friction. Therefore, we confirm the results from Capet et al. (2008c) and Molemaker et al. (2010) who find that ageostrophic dynamics are able to yield a direct route to dissipation in contrast to quasi-

geostrophic dynamics. Here, we relate the strength of this direct route to the Richardson number Ri that characterizes the dynamical conditions of our model.

For simulations with large Ri, the observed dynamics are to a large extent in geostrophic balance. The smaller Ri becomes, however, the more unbalanced ageostrophic dynamics are evident (see also Stone (1970) and Molemaker et al. (2005)). These unbalanced dynamics feature a horizontal divergent velocity field. A decomposition of the energy flux into its rotational and divergent components shows a close relation between the energy flux associated with the divergent velocity component and the downscale energy flux. Therefore, we conclude that the strength of the small-scale dissipation directly depends on the strength of the divergent velocity field.

Until now it is not clear how the energy of the mesoscale eddy field is dissipated. Some possible candidates are lee wave generation (Bell, 1975; Nikurashin and Ferrari, 2011), Lighthill generation of gravity waves (Ford et al., 2000) or ageostrophic instability (Molemaker et al., 2005). If these processes are responsible for the downscale energy fluxes induced by ageostrophic dynamics as found by studies of (Capet et al., 2008c; Molemaker et al., 2010) and in this study is not entirely clear. However, a quantification for all these processes is mandatory in order to obtain a more detailed understanding of the energy cycle of the ocean circulation. The results obtained in this study can be used as a first step towards a quantification of the ageostrophic downscale kinetic energy flux. Together with a parameterization for baroclinic production that can be obtained e.g. from linear stability analysis (Stone, 1972b) or a scaling of the potential energy release (Fox-Kemper et al., 2008), the estimated Richardson-dependency of the present study might be used to obtain first estimates about location and magnitude of this direct route to dissipation.

Furthermore, a qualitative and quantitative understanding of direction and magnitude of the kinetic energy flux are helpful in improving parameterizations for momentum dissipation. Most numerical model studies (the present one included) use some kind of artificial viscous diffusion that extracts energy close to the grid scale in dependency on the magnitude of the viscosity and on the magnitude of the velocity shear (or higher derivatives of the velocity). For a constant viscosity, it is not guaranteed that only that amount of energy is dissipated that otherwise would be transferred towards the scales of molecular dissipation.

Smagorinsky (1963) uses the assumption of a downscale energy flux to control the specific amount of dissipation by adapting the viscosity. However, quasi-geostrophic dynamics yield an upscale energy flux and it is therefore questionable to which extent the

approach of Smagorinsky (1963) yields reasonable dissipation rates for these dynamics. Leith (1968) derives a scaling of the viscosity for a two-dimensional flow that preserves enstrophy. Therefore, the approach of Leith (1968) might be considered as more applicable to quasi-geostrophic dynamics. However, as shown by Capet et al. (2008c); Molemaker et al. (2010) and in this study, in the presence of ageostrophic dynamics, the energy flux is downscale. Therefore, it is important to combine the approaches of Smagorinsky (1963) and Leith (1968) for considering both dynamical regimes to obtain a more reasonable parameterization of the viscosity. Scaling laws as presented by this study that relate the dissipation to e.g. the Richardson number and with this to the dynamics of the flow can therefore provide the basis for more sophisticated parameterizations of momentum dissipation.

Although our model simulations allow some insights into the different dynamics acting at small and large Ri, they contain many simplifications in contrast to more realistic flow systems. The zonal mean drag extracts energy at the basin scale of our model domain. For a model with a larger domain size, we would expect this energy to be transferred further towards larger scales. At these scales, different dissipation mechanism like e.g. lee wave generation (Bell, 1975; Nikurashin and Ferrari, 2011), Lighthill generation of gravity waves (Ford et al., 2000) or ageostrophic instabilities (Molemaker et al., 2005) might play an important role. In our simulations, we prescribe an artificial cutoff of the energy transport and therefor assume that there is no further backscattering of energy. Furthermore, biharmonic diffusion is certainly rather an artificial than a realistic way to dissipate energy on small scales. However, we assume that the energy flux is more or less independent of the specific realization of the small-scale and large-scale dissipation and that our results would not change for other dissipation schemes.

The restoring of zonal mean buoyancy is a diabatic process. Since the ocean interior is assumed to be nearly adiabatic, our model might primarily be seen as a model of the ocean mixed layer where diabatic processes are certainly present. The buoyancy restoring might be replaced by other processes that prevent a re-stratification of an inclined buoyancy surface to obtain comparable flow conditions in an adiabatic environment. In general, we would expect that our results are also transferable to situations where an inclination of the buoyancy surfaces is retained by a more realistic process than our artificial restoring.

Furthermore, the setup considered in this study intents to simulate horizontally isotropic turbulence since we assume constant values of vertical and horizontal stratification as well as a constant planetary vorticity. Especially for larger scales, however, a change of the

planetary vorticity causes a development of zonal jets and thus a highly anisotropic flow. A characteristic length scale of these zonal jets is the Rhines scale $L_\beta \propto \sqrt{U/\beta}$ where β is the change of planetary vorticity and U a characteristic velocity scale. The upscale energy cascade of quasi-geostrophic turbulence is not necessarily halted at this scale, but the energy spectrum becomes highly anisotropic for larger scales (see e.g. Vallis (2006)) and it is not clear to which extent the results obtained e.g. for the scaling of the large and small-scale dissipation rates hold for such anisotropic flows. Nevertheless, we do not expect major changes on smaller scales since these are not effected by the β-effect as long as their scale is smaller than L_β.

4.7 Appendix A: Derivation of the spectral kinetic energy density

To obtain an expression for the spectral kinetic energy density, we first consider the cumulative kinetic energy associated with low pass filtered velocities (see Frisch (1995))

$$\boldsymbol{u}_K^< = \sum_{k<K} \widehat{\boldsymbol{u}_{\boldsymbol{h}}} e^{i\boldsymbol{k}\boldsymbol{r}}, \tag{4.14}$$

where $k = \sqrt{k_x^2 + k_y^2}$ is the horizontal wavenumber and K a cutoff wavenumber. The globally averaged cumulative kinetic energy $E_k^<$ than reads

$$E_k^< = \frac{1}{V} \int \frac{1}{2} \left(\boldsymbol{u}_K^<\right)^2 \mathrm{d}^3\boldsymbol{r}, \tag{4.15}$$

$$= \frac{1}{2H} \int \sum_{k,k'<K} \widehat{\boldsymbol{u}_{\boldsymbol{h}}}(\boldsymbol{k}) \cdot \widehat{\boldsymbol{u}_{\boldsymbol{h}}}(\boldsymbol{k}') \frac{1}{A} \int e^{i(\boldsymbol{k}+\boldsymbol{k}')\boldsymbol{r}} \,\mathrm{d}^2\boldsymbol{r}\,\mathrm{d}z, \tag{4.16}$$

by using $\frac{1}{A}\int e^{i(\boldsymbol{k}+\boldsymbol{k}')\boldsymbol{r}}\,\mathrm{d}^2\boldsymbol{r} = \delta_{\boldsymbol{k},-\boldsymbol{k}'}$ it can be written as

$$E_k^< = \frac{1}{2H} \int \sum_{k,k'<K} \widehat{\boldsymbol{u}_{\boldsymbol{h}}}(\boldsymbol{k}) \cdot \widehat{\boldsymbol{u}_{\boldsymbol{h}}}(\boldsymbol{k}') \delta_{\boldsymbol{k},-\boldsymbol{k}'}\,\mathrm{d}z, \tag{4.17}$$

$$= \frac{1}{2H} \int \sum_{k<K} \widehat{\boldsymbol{u}_{\boldsymbol{h}}}^*(\boldsymbol{k}) \cdot \widehat{\boldsymbol{u}_{\boldsymbol{h}}}(\boldsymbol{k})\,\mathrm{d}z, \tag{4.18}$$

From this, we obtain the spectral kinetic energy density by differentiating

$$E_{\mathrm{KE}} = \partial_k E_k^<, \tag{4.19}$$

$$= \frac{1}{H\Delta k} \int \widehat{\boldsymbol{u_h}}^* \cdot \widehat{\boldsymbol{u_h}} \, \mathrm{d}z, \tag{4.20}$$

with $\Delta k = 2\pi/(L_x^2 + L_y^2)^{1/2}$. Likewise, any spectral tendency $\widehat{T_{\mathrm{KE}}}$ within the balance of E_{KE} can be derived by the corresponding tendencies T_u and T_v of the zonal and meridional momentum equations, respectively

$$\widehat{T_{\mathrm{KE}}} = \frac{1}{2H\Delta k} \int \left(\widehat{u}^* \widehat{T_u} + \widehat{v}^* \widehat{T_v} \right) \mathrm{d}z. \tag{4.21}$$

Chapter 5

Conclusions

In this chapter, the main results of the previous studies are summarized and answers to the specific research questions formulated in Chapter 1 are given. Each discussion is followed by a short outlook on remaining and pursuing questions.

5.1 Effects of ageostrophic processes on the meridional overturning circulation

Are zonally averaged ocean models that parameterize the zonally averaged meridional flow with the zonally averaged meridional pressure gradient dynamically inconsistent?

Numerical layer and primitive equation models show that the zonally averaged meridional pressure gradient is independent of the zonally averaged meridional flow (in accordance to the hypothesis of Straub (1996)). Models that rely on a parameterization of the zonally averaged meridional flow by the meridional pressure gradient (e.g. Marotzke et al., 1988; Wright and Stocker, 1991; Wright et al., 1998) are therefore dynamically inconsistent. The flow and stratification of such a model shows important discrepancies in comparison to zonally resolved but otherwise identical three-dimensional models. Even though the inconsistent models predict the right direction of the meridional transport, they predict a wrong sign of the meridional pressure gradient as a consequence of the inherent inconsistency of the models.

If yes, how can geostrophic and ageostrophic dynamics be considered in order to obtain a dynamical consistent model of the zonally averaged meridional overturning circulation?

In Chapter 2, the approach of Wright et al. (1995) is followed and extended to construct a zonally averaged model that does not suffer from the inconsistency mentioned by Straub (1996). Therefore, the ocean is divided into two regimes, a western boundary current and an interior part. While for the latter a geostrophic balance that yields an upwelling dominated meridional Sverdrup transport is assumed, ageostrophic dynamics in form of simple Rayleigh friction are taken into account in the momentum budget for the former. In contrast to Wright et al. (1995), no attempt is made to integrate the resulting vorticity equation which includes the need to find an integration constant that determines the magnitude and direction of the meridional transport. Instead, the momentum equations averaged over the western boundary and the interior domain are considered, respectively. As a consequence, three quantities need to be parameterized; the zonal velocity at the interface between western boundary current and interior, the meridional pressure difference over the western boundary part and the meridional pressure difference over the interior.

Parameterizations for these three quantities are validated by a three-dimensional numerical model. The diagnosed quantities from the zonally resolved model are found to be in good agreement with the parameterizations. Furthermore, the circulation predicted by a numerical model simulation based on the new parameterization is analyzed. Again, good agreement is found between the dynamics predicted by the new zonally averaged model and that analyzed from a zonally resolved model. Therefore, it can be concluded that the proposed parameterization is able to yield a dynamically consistent model since it considers both dynamical regimes; the geostrophically balanced interior part of the ocean on the one hand and a western boundary layer part where ageostrophic dynamics play an important role, on the other hand.

Outlook

A numerical integration of zonally averaged models is less cost-intensive than that of a three dimensional domain. Therefore, zonally averaged models are a powerful tool whenever simulations need to be performed over long time periods. One of two classical examples is the simulation of paleo-climate phenomena or future climate predictions. In this case, it is quite common that simulations have to be performed over centuries to millennia. Therefore, zonally averaged models can be very helpful to investigate possible responses

like a halting of the MOC (e.g. Manabe and Stouffer, 1994; Jungclaus et al., 2006) of the ocean circulation to past or future atmospheric surface forcing. Zonally averaged models based on the inconsistent closure are already implemented in climate models of intermediate complexity (Claussen et al., 2002) and it is important to investigate how the results of such models are modified if the new consistent closure is used.

The second example concerns sensitivity studies of the meridional overturning circulation with respect to e.g. idealized surface forcing. The box-model of Stommel (1961) as well as zonally averaged models predict the possibility of different equilibria and hysteresis loops of the MOC (e.g. Marotzke et al., 1988). Since the model of Stommel (1961) and the zonally averaged models of Marotzke et al. (1988); Wright and Stocker (1991) and Wright et al. (1998) are based on similar parameterizations for the meridional flow, it is important to examine in which way the results obtained from these models are modified if the new consistent closure is used. Preliminary studies of multiple equilibria and hysteresis loops with the zonally averaged model introduced in this study promise interesting results as can be inferred from Olbers et al. (2012).

5.2 Parameterizations for eddy fluxes in an ageostrophic environment

What are the main differences between eddy flux parameterizations based on linear stability analysis and parameterizations based on scalings of the eddy potential energy release?

Linear stability analysis and a scaling of the potential energy release yield two competing approaches to parameterize eddy fluxes under geostrophic and ageostrophic conditions (Stone, 1972b; Fox-Kemper et al., 2008). A comparison of both parameterizations is achieved by relating the magnitude of the eddy fluxes to two dimensionless parameters which are important to characterize the dynamical condition of the flow, namely the Richardson number and the ratio between Rossby number and the aspect ratio. It is found that both parameterizations show the same parameter dependency with respect to the second parameter, i.e. the ratio of Rossby number and aspect ratio, but that they differ with respect to the first parameter, the Richardson number. As a consequence, they predict a different magnitude of the eddy fluxes for different dynamical conditions of the flow. This difference is especially important when both geostrophic and ageostrophic dynamics

are considered since the magnitude of the Richardson number varies over several orders of magnitude between both dynamical regimes.

Both parameterizations agree by predicting a parabolic-shaped vertical structure of the vertical eddy fluxes over a wide range of Richardson numbers. In contrast, a further difference between both parameterizations concerns the vertical dependency of the meridional eddy flux. While the parameterization based on linear stability analysis predicts a constant profile, the parameterization based on a scaling of the potential energy release predicts a parabolic-shaped vertical structure of the meridional eddy fluxes.

How do parameterizations of mixed layer eddy fluxes perform under ageostrophic and geostrophic conditions?

Both parameterizations are validated using numerical simulations for different dynamical conditions and thus different Richardson numbers in two scenarios, an equilibrated flow and the spin-down of a density front. A comparison of the diagnosed eddy fluxes and the parameterized counterparts reveals a slightly better performance of the parameterization based on linear stability analysis in the first scenario. In contrast, the parameterization based on the scaling of a potential energy release yields a slightly more accurate magnitude of the eddy fluxes in the second scenario. Both parameterizations predict the magnitude of the eddy fluxes up to a factor of three for simulations in which the Richardson number differs over three orders of magnitude.

Domain averages of the vertical profiles of the eddy fluxes are diagnosed and compared with the predicted analytical profiles of the parameterizations. It turns out that the vertical profile of the diagnosed vertical eddy flux is matched well by the vertical structure function predicted from both parameterizations. In contrast, the vertical profile of the meridional eddy flux is better matched by the parameterization based on linear stability analysis than by the parameterization based on the potential energy release.

Outlook

Fox-Kemper et al. (2011) implement the parameterization that is based on the potential energy release scaling in a global ocean model. A quantification of the influence of the parameterization on e.g. bio-geochemical processes or the air-sea gas exchange is still missing. For more sophisticated bio-geochemical models, adequate parameterizations for mixed layer eddies play a very important role, since they have a large influence on the mixed layer depth or on vertical fluxes of heat and other substances. So far no investi-

gations have been made about the influence of the competing parameterization of Stone (1972b) on bio-geochemical processes, the air-sea heat and gas exchange or the mixed layer depth. Therefore, it would be important to do so and to compare the results with the parameterization based on the scaling of the potential energy release (Fox-Kemper et al., 2008).

We also find a good agreement of both parameterizations for larger Richardson numbers and thus quasi-geostrophic conditions. Both parameterizations might thus also yield an adequate representation of the effect of mesoscale eddies in the ocean interior. Some variants of the parameterization based on linear stability analysis are already implemented in numerical ocean models (e.g. Killworth, 1997; Eden, 2011) partly with extensions to account also for a meridional gradient of the planetary vorticity. Therefore, it would be important to investigate how the parameterization based on the potential energy release scaling would perform in comparison. Since this parameterization does not consider any change of the planetary vorticity, it might have to be extended in order to yield reasonable results for the mesoscale eddy mixing on a global scale.

5.3 The route to dissipation in the presence of ageostrophic dynamics

How can a downscale energy flux and the resulting small-scale dissipation be related to the dynamical characteristics of a flow system?

In Chapter 4, the spectral kinetic energy flux for different dynamical conditions characterized by the Richardson number Ri is investigated. For simulations with large Ri and thus predominantly geostrophic dynamics, an upscale energy flux is found in accordance to the predictions of quasi-geostrophic turbulence (Charney, 1971). For simulations with smaller Ri, however, ageostrophic effects become important and a downscale energy flux emerges at smaller scales in addition to an upscale flux at larger scales. For $\mathrm{Ri} = \mathcal{O}(1)$, the energy flux is towards smaller scales for the whole wavenumber range and the upscale flux vanishes. Therefore, the results of this study confirm findings from Capet et al. (2008c) and Molemaker et al. (2010) who report a downscale energy flux for unbalanced ageostrophic dynamics. By dividing the velocity into its rotational and divergent components, it is also confirmed that the divergent part of the velocity features a downscale energy flux whereas the rotational part is predominantly responsible for an upscale energy flux.

For simulations with different dynamical conditions and thus varying Richardson numbers, a systematic decrease of the downscale energy flux for increasing Ri is found. The extent to which ageostrophic processes generate the downscale energy flux can now be identified by an easy accessible quantity like the Richardson number. It is thus possible to directly predict the ability of a flow to feature a downscale energy flux. A linear regression is used to infer the dependency of the dissipation on the Richardson number. The obtained power law yields reasonable predictions for the dissipation rates for the considered numerical simulations. This dependency of the dissipation makes it possible to quantify the direct route of kinetic energy to dissipation induced by ageostrophic dynamics.

Outlook

The pathway of energy contained in the mesoscale and sub-mesoscale eddy field is still not understood (Ferrari and Wunsch, 2009). In addition, parameterizations in ocean models are often implemented in an energetically inconsistent way. Current parameterizations for momentum dissipation, for instance, do not consider effects of an up- or downscale energy flux, i.e. the amount of energy that is dissipated by these parameterization is not related to the amount of energy that would be transported downscale by the ageostrophic flow. Instead current parameterizations extract a certain amount of energy that, for most parameterizations, is related to the mean velocity shear but not to dynamical parameters like the Richardson number. Therefore, the extracted amount of energy is likely to be inappropriate. Results obtained in this study can yield guidance to more appropriate parameterizations. The dependency of the energy dissipation on the Richardson number can be used to construct parameterizations that yield a more realistic energy extraction by accounting for the up- and downscale energy flux in dependency on the underlying dynamical conditions.

Furthermore, the proposed dependency of the energy dissipation on the Richardson number might be used to quantify the ability of ageostrophic dynamics to dissipate momentum. Since the scaling makes it possible to relate this ability to the Richardson number, a direct accessible quantity, it would be possible to obtain first estimates of the small-scale dissipation rate by using climatologies from observations or ocean models. Therefore, global estimates of the energy dissipation resulting from ageostrophic downscale energy fluxes might be obtained.

5.4 Synthesis

Progress in ocean sciences generated recently an increasing interest in the dynamics of the ocean on spatial and temporal scales below the planetary geostrophic or quasi-geostrophic scales. Numerical models and observations report large differences between the dynamics on these smaller scales in contrast to the larger scale dynamics. A large number of processes observed on these smaller scales cannot be explained under the assumption of a geostrophic balance – a fundamental concept that has brought otherwise much insight into many aspects of the large-scale circulation – indicating that ageostrophic dynamics need to be taken into account in order to yield more adequate explanations for the processes mentioned above.

Since many conceptual models based on the assumption of a geostrophic balance fail in describing small-scale phenomena as soon as ageostrophic processes become important, new concepts and models have to be developed and investigated to provide a theoretical framework for understanding and interpreting these phenomena. This thesis contributes to the development of such simplified models of the more complex reality by regarding three case studies and by investigating possible simplifications of the underlying processes. However, many remaining questions and also new ones maintain the need for pencils and CPU hours.

Acknowledgments

First of all, I would like to express my gratitude to my supervisor Carsten Eden for the opportunity to realize this work. I benefited a lot from his expertise and infinite pool of ideas. I am very thankful for his encouragement when I had too many doubts, and for tempering my enthusiasm when I had too few.

I would also like to thank Johann Jungclaus for the helpful discussions during my advisory panel meetings and for taking the time to serve as a referee for this work.

A very special thanks goes out to Lars Czeschel for his great support. He not only helped me with the MIT model, but also proof-read this thesis, answered so many of my questions and raised new ones.

Furthermore, I would like to acknowledge Thomas Pohlmann for his always helpful and encouraging advice not only during the advisory panel meetings.

I am very thankful for many interesting discussions with Dirk Olbers and his enthusiasm and help especially during the work on my first publication, but most of all for having raised my interest in oceanography.

Many thanks go also to my colleagues and friends of the work group of Theoretical Oceanography for a nice and friendly working atmosphere. Especially, I want to acknowledge Tanja Mildner for literally bringing color into our office and her catching good mood. I would also like to mention Martina Nemes for her helpful and obliging advice for all kinds of official concerns and for proof-reading.

Having been a member of the School of Integrated Climate System Sciences has enabled me to take part in many interesting lectures, but first of all it has brought me into contact with many other young earth system scientists, which is kindly acknowledged.

This work would not have been possible without the support of my friends and my family! Many thanks to you!

Finally, I want to thank Silke, not only for proof-reading, but most of all for having been such a patient and great support during the last year of my thesis.

Bibliography

Alexander, J. and A. H. Monahan, 2009: Nonnormal Perturbation Growth of Pure Thermohaline Circulation Using a 2D Zonally Averaged Model. *J. Phys. Oceanogr.*, **39**(2), 369–386.

Andrews, D. G., J. R. Holton, and C. B. Leovy, 1987: *Middle Atmosphere Dynamics*. Academic Press.

Bachman, S. and B. Fox-Kemper, 2013: Eddy parameterization challenge suite I: Eady spindown. *Ocean Modelling*, **64**(0), 12–28.

Badin, G., A. Tandon, and A. Mahadevan, 2011: Lateral Mixing in the Pycnocline by Baroclinic Mixed Layer Eddies. *J. Phys. Oceanogr.*, **41**(11), 2080–2101.

Bell, T. H., 1975: Topographically generated internal waves in the open ocean. *J. Geophys. Res.*, **80**(3), 320–327.

Blumen, W., 1978: Uniform Potential Vorticity Flow: Part I. Theory of Wave Interactions and Two-Dimensional Turbulence. *J. Atmos. Sci.*, **35**(5), 774–783.

Boccaletti, G., R. Ferrari, and B. Fox-Kemper, 2007: Mixed Layer Instabilities and Restratification. *J. Phys. Oceanogr.*, **37**(9), 2228–2250.

Brüggemann, N., C. Eden, and D. Olbers, 2011: A Dynamically Consistent Closure for Zonally Averaged Ocean Models. *J. Phys. Oceanogr.*, **41**(11), 2242–2258.

Capet, X., J. C. McWilliams, M. J. Molemaker, and A. F. Shchepetkin, 2008a: Mesoscale to Submesoscale Transition in the California Current System. Part I: Flow Structure, Eddy Flux, and Observational Tests. *J. Phys. Oceanogr.*, **38**(1), 29–43.

Capet, X., J. C. McWilliams, M. J. Molemaker, and A. F. Shchepetkin, 2008b: Mesoscale to Submesoscale Transition in the California Current System. Part II: Frontal Processes. *J. Phys. Oceanogr.*, **38**(1), 44–64.

Capet, X., J. C. McWilliams, M. J. Molemaker, and A. F. Shchepetkin, 2008c: Mesoscale to Submesoscale Transition in the California Current System. Part III: Energy Balance and Flux. *J. Phys. Oceanogr.*, **38**(10), 2256–2269.

Charney, J. G., 1971: Geostrophic Turbulence. *J. Atmos. Sci.*, **28**(6), 1087–1095.

Claussen, M., L. Mysak, A. Weaver, M. Crucifix, T. Fichefet, M.-F. Loutre, S. Weber, J. Alcamo, V. Alexeev, A. Berger, R. Calov, A. Ganopolski, H. Goosse, G. Lohmann, F. Lunkeit, I. Mokhov, V. Petoukhov, P. Stone, and Z. Wang, 2002: Earth system models of intermediate complexity: Closing the gap in the spectrum of climate system models. *Climate Dynamics*, **18**(7), 579–586.

Deusebio, E., A. Vallgren, and E. Lindborg, 2013: The route to dissipation in strongly stratified and rotating flows. *Journal of Fluid Mechanics*, **720**, 66–103.

Dewan, E., 1997: Saturated-cascade similitude theory of gravity wave spectra. *J. Geophys. Res.*, **102**(D25), 29799–29817.

Eady, E. T., 1949: Long Waves and Cyclone Waves. *Tellus*, **1**(3), 33–52.

Eden, C., 2007: Eddy length scales in the North Atlantic Ocean. *J. Geophys. Res.*, **112**(C6), C06004.

Eden, C., 2011: A closure for meso-scale eddy fluxes based on linear instability theory. *Ocean Modelling*, **39**(3-4), 362–369.

Eden, C., 2012: Implementing diffusivities from linear stability analysis in a three-dimensional general circulation ocean model. *Ocean Modelling*, **57-58**(0), 15–28.

Eden, C. and R. J. Greatbatch, 2008a: Diapycnal mixing by meso-scale eddies. *Ocean Modelling*, **23**(3-4), 113–120.

Eden, C. and R. J. Greatbatch, 2008b: Towards a mesoscale eddy closure. *Ocean Modelling*, **20**(3), 223–239.

Ferrari, R. and C. Wunsch, 2009: Ocean Circulation Kinetic Energy: Reservoirs, Sources, and Sinks. *Annual Review of Fluid Mechanics*, **41**, 253–282.

Ferreira, D. and J. Marshall, 2006: Formulation and implementation of a residual-mean ocean circulation model. *Ocean Modelling*, **13**(1), 86–107.

Fjørtoft, R., 1953: On the Changes in the Spectral Distribution of Kinetic Energy for Twodimensional, Nondivergent Flow. *Tellus*, **5**(3), 225–230.

Ford, R., M. E. McIntyre, and W. A. Norton, 2000: Balance and the Slow Quasimanifold: Some Explicit Results. *J. Atmos. Sci.*, **57**(9), 1236–1254.

Fox-Kemper, B., G. Danabasoglu, R. Ferrari, S. Griffies, R. Hallberg, M. Holland, M. Maltrud, S. Peacock, and B. Samuels, 2011: Parameterization of mixed layer eddies. III: Implementation and impact in global ocean climate simulations. *Ocean Modelling*, **39**(1-2), 61–78.

Fox-Kemper, B. and R. Ferrari, 2008: Parameterization of Mixed Layer Eddies. Part II: Prognosis and Impact. *J. Phys. Oceanogr.*, **38**(6), 1166–1179.

Fox-Kemper, B., R. Ferrari, and R. Hallberg, 2008: Parameterization of Mixed Layer Eddies. Part I: Theory and Diagnosis. *J. Phys. Oceanogr.*, **38**(6), 1145–1165.

Frisch, U., 1995: *Turbulence: the Legacy of A.N. Kolmogorov*. Cambridge University Press, Cambridge, USA.

Garabato, A. C. N., K. L. Polzin, B. A. King, K. J. Heywood, and M. Visbeck, 2004: Widespread Intense Turbulent Mixing in the Southern Ocean. *Science*, **303**(5655), 210–213.

Gent, P. R. and J. C. McWilliams, 1990: Isopycnal Mixing in Ocean Circulation Models. *J. Phys. Oceanogr.*, **20**(1), 150–155.

Gent, P. R., J. Willebrand, T. J. McDougall, and J. C. McWilliams, 1995: Parameterizing Eddy-Induced Tracer Transports in Ocean Circulation Models. *J. Phys. Oceanogr.*, **25**(4), 463–474.

Gill, A. E., 1982: *Atmosphere-ocean dynamics*. Academic Press, San Diego, CA.

Gnanadesikan, A., 1999: A Simple Predictive Model for the Structure of the Oceanic Pycnocline. *Science*, **283**(5410), 2077–2079.

Greatbatch, R. J. and J. Lu, 2003: Reconciling the Stommel Box Model with the Stommel-Arons Model: A Possible Role for Southern Hemisphere Wind Forcing? *J. Phys. Oceanogr.*, **33**(8), 1618–1632.

Green, J. S. A., 1970: Transfer properties of the large-scale eddies and the general circulation of the atmosphere. *Q.J.R. Meteorol. Soc.*, **96**(408), 157–185.

Haine, T. W. N. and J. Marshall, 1998: Gravitational, Symmetric, and Baroclinic Instability of the Ocean Mixed Layer. *J. Phys. Oceanogr.*, **28**(4), 634–658.

Holland, W. R., 1978: The Role of Mesoscale Eddies in the General Circulation of the Ocean – Numerical Experiments Using a Wind-Driven Quasi-Geostrophic Model. *J. Phys. Oceanogr.*, **8**(3), 363–392.

Jungclaus, J. H., N. Fischer, H. Haak, K. Lohmann, J. Marotzke, D. Matei, U. Mikolajewicz, D. Notz, and J. S. von Storch, 2013: Characteristics of the ocean simulations in the Max Planck Institute Ocean Model (MPIOM) the ocean component of the MPI-Earth system model. *J. Adv. Model. Earth Syst.*, **5**(2), 422–446.

Jungclaus, J. H., H. Haak, M. Esch, E. Roeckner, and J. Marotzke, 2006: Will Greenland melting halt the thermohaline circulation? *Geophys. Res. Lett.*, **33**(17), L17708.

Kawase, M., 1987: Establishment of Deep Ocean Circulation Driven by Deep-Water Production. *J. Phys. Oceanogr.*, **17**(12), 2294–2317.

Killworth, P., 1997: On the parameterization of eddy transfer Part I. Theory. *J. Mar. Res.*, **55**(6), 1171–1197.

Klein, P., B. L. Hua, G. Lapeyre, X. Capet, S. Le Gentil, and H. Sasaki, 2008: Upper Ocean Turbulence from High-Resolution 3D Simulations. *J. Phys. Oceanogr.*, **38**(8), 1748–1763.

Kolmogorov, A. N., 1941: Dissipation of Energy in the Locally Isotropic Turbulence. *Proceedings: Mathematical and Physical Sciences*, **434**(1890), 15–17.

Kuhlbrodt, T., A. Griesel, M. Montoya, A. Levermann, M. Hofmann, and S. Rahmstorf, 2007: On the driving processes of the Atlantic meridional overturning circulation. *Rev. Geophys.*, **45**(2), RG2001.

LaCasce, J. H., 2012: Surface Quasigeostrophic Solutions and Baroclinic Modes with Exponential Stratification. *J. Phys. Oceanogr.*, **42**(4), 569–580.

Larichev, V. D. and I. M. Held, 1995: Eddy Amplitudes and Fluxes in a Homogeneous Model of Fully Developed Baroclinic Instability. *J. Phys. Oceanogr.*, **25**(10), 2285–2297.

Leith, C. E., 1968: Diffusion Approximation for Two-Dimensional Turbulence. *Physics of Fluids (1958-1988)*, **11**(3), 671–672.

Leonard, B. P., 1979: A stable and accurate convective modelling procedure based on quadratic upstream interpolation. *Computer Methods in Applied Mechanics and Engineering*, **19**, 59–98.

Levermann, A. and J. J. Fürst, 2010: Atlantic pycnocline theory scrutinized using a coupled climate model. *Geophys. Res. Lett.*, **37**(14), L14602.

Lévy, M., D. Iovino, L. Resplandy, P. Klein, G. Madec, A.-M. Tréguier, S. Masson, and K. Takahashi, 2012: Large-scale impacts of submesoscale dynamics on phytoplankton: Local and remote effects. *Ocean Modelling*, **43-44**(0), 77–93.

Lévy, M., P. Klein, and A. M. Tréguier, 2001: Impact of sub-mesoscale physics on production and subduction of phytoplankton in an oligotrophic regime. *Journal of Marine Research*, **59**(4), 535–565.

Lindborg, E., 2005: The effect of rotation on the mesoscale energy cascade in the free atmosphere. *Geophys. Res. Lett.*, **32**(1), L01809.

Lindborg, E., 2006: The energy cascade in a strongly stratified fluid. *Journal of Fluid Mechanics*, **550**, 207–242.

Lorenz, E. N., 1955: Available Potential Energy and the Maintenance of the General Circulation. *Tellus*, **7**(2), 157–167.

Mahadevan, A., 2006: Modeling vertical motion at ocean fronts: Are nonhydrostatic effects relevant at submesoscales? *Ocean Modelling*, **14**(3-4), 222–240.

Manabe, S. and R. J. Stouffer, 1994: Multiple-Century Response of a Coupled Ocean-Atmosphere Model to an Increase of Atmospheric Carbon Dioxide. *J. Climate*, **7**(1), 5–23.

Marotzke, J., P. Welander, and J. Willebrand, 1988: Instability and multiple steady states in a meridional-plane model of the thermohaline circulation. *Tellus A*, **40A**(2), 162–172.

Marshall, J., A. Adcroft, C. Hill, L. Perelman, and C. Heisey, 1997: A finite-volume, incompressible Navier Stokes model for studies of the ocean on parallel computers. *J. Geophys. Res.*, **102**(C3), 5753–5766.

McManus, J. F., R. Francois, J. M. Gherardi, L. D. Keigwin, and S. Brown-Leger, 2004: Collapse and rapid resumption of Atlantic meridional circulation linked to deglacial climate changes. *Nature*, **428**(6985), 834–837.

McWilliams, J. C., 1985a: A Uniformly Valid Model Spanning the Regimes of Geostrophic and Isotropic, Stratified Turbulence: Balanced Turbulence. *J. Atmos. Sci.*, **42**(16), 1773–1774.

McWilliams, J. C., 1985b: Submesoscale, coherent vortices in the ocean. *Rev. Geophys.*, **23**(2), 165–182.

Molemaker, M. J. and J. C. McWilliams, 2010: Local balance and cross-scale flux of available potential energy. *Journal of Fluid Mechanics*, **645**, 295–314.

Molemaker, M. J., J. C. McWilliams, and X. Capet, 2010: Balanced and unbalanced routes to dissipation in an equilibrated Eady flow. *Journal of Fluid Mechanics*, **654**, 35–63.

Molemaker, M. J., J. C. McWilliams, and I. Yavneh, 2005: Baroclinic Instability and Loss of Balance. *J. Phys. Oceanogr.*, **35**(9), 1505–1517.

Munk, W., L. Armi, K. Fischer, and F. Zachariasen, 2000: Spirals on the sea. *Proceedings of the Royal Society of London. Series A: Mathematical, Physical and Engineering Sciences*, **456**(1997), 1217–1280.

Nastrom, G. D. and K. S. Gage, 1985: A Climatology of Atmospheric Wavenumber Spectra of Wind and Temperature Observed by Commercial Aircraft. *J. Atmos. Sci.*, **42**(9), 950–960.

Nikurashin, M. and R. Ferrari, 2011: Global energy conversion rate from geostrophic flows into internal lee waves in the deep ocean. *Geophys. Res. Lett.*, **38**(8), L08610.

Olbers, D. and M. Visbeck, 2005: A Model of the Zonally Averaged Stratification and Overturning in the Southern Ocean. *J. Phys. Oceanogr.*, **35**(7), 1190–1205.

Olbers, D., J. Willebrand, and C. Eden, 2012: *Ocean Dynamics*. Springer.

Oschlies, A., 2002: Improved Representation of Upper-Ocean Dynamics and Mixed Layer Depths in a Model of the North Atlantic on Switching from Eddy-Permitting to Eddy-Resolving Grid Resolution. *J. Phys. Oceanogr.*, **32**(8), 2277–2298.

Polzin, K. L., J. M. Toole, J. R. Ledwell, and R. W. Schmitt, 1997: Spatial Variability of Turbulent Mixing in the Abyssal Ocean. *Science*, **276**(5309), 93–96.

Quadfasel, D. and R. Käse, 2013: Present-Day Manifestation of the Nordic Seas Overflows. In: *Ocean Circulation: Mechanisms and Impacts – Past and Future Changes of Meridional Overturning*, pp. 75–89. American Geophysical Union.

Rahmstorf, S., 1996: On the freshwater forcing and transport of the Atlantic thermohaline circulation. *Climate Dynamics*, **12**(12), 799–811.

Rahmstorf, S., M. Crucifix, A. Ganopolski, H. Goosse, I. Kamenkovich, R. Knutti, G. Lohmann, R. Marsh, L. A. Mysak, Z. Wang, and A. J. Weaver, 2005: Thermohaline circulation hysteresis: A model intercomparison. *Geophys. Res. Lett.*, **32**(23), L23605.

Rhines, P., 1977: *The Sea*, volume 6, chapter The dynamics of unsteady currents, pp. 189–318. Wiley, New York.

Scully-Power, P., 1986: Navy Oceanographer Shuttle observations, STS 41-G Mission Report. Technical report, DTIC Document.

Shcherbina, A. Y., E. A. D'Asaro, C. M. Lee, J. M. Klymak, M. J. Molemaker, and J. C. McWilliams, 2013: Statistics of vertical vorticity, divergence, and strain in a developed submesoscale turbulence field. *Geophys. Res. Lett.*, **40**(17), 4706–4711.

Smagorinsky, J., 1963: General Circulation experiments with the primitive equations: I. The basic experiment. *Mon. Wea. Rev.*, **91**(3), 99–164.

Solomon, S., D. Qin, M. Manning, Z. Chen, M. Marquis, K. Averyt, M. Tignor, and H. Miller, 2007: *Climate Change 2007: The Physical Science Basis*. University Press.

Stommel, H., 1948: The westward intensification of wind-driven ocean currents. *Trans. Amer. Geophys. Union*, **29**(2), 202–206.

Stommel, H., 1961: Thermohaline Convection with Two Stable Regimes of Flow. *Tellus*, **13**(2), 224–230.

Stommel, H. and A. Arons, 1960: On the abyssal circulation of the world ocean-I. Stationary planetary flow patterns on a sphere. *Deep Sea Research (1953)*, **6**(0), 140–154.

Stone, P. H., 1966: On Non-Geostrophic Baroclinic Stability. *J. Atmos. Sci.*, **23**(4), 390–400.

Stone, P. H., 1970: On Non-Geostrophic Baroclinic Stability: Part II. *J. Atmos. Sci.*, **27**(5), 721–726.

Stone, P. H., 1971: Baroclinic stability under non-hydrostatic conditions. *Journal of Fluid Mechanics*, **45**(04), 659–671.

Stone, P. H., 1972a: A Simplified Radiative-Dynamical Model for the Static Stability of Rotating Atmospheres. *J. Atmos. Sci.*, **29**(3), 405–418.

Stone, P. H., 1972b: On Non-Geostrophic Baroclinic Stability: Part III. The Momentum and Heat Transports. *J. Atmos. Sci.*, **29**(3), 419–426.

Storch, J.-S. v., C. Eden, I. Fast, H. Haak, D. Hernández-Deckers, E. Maier-Reimer, J. Marotzke, and D. Stammer, 2012: An Estimate of the Lorenz Energy Cycle for the World Ocean Based on the STORM/NCEP Simulation. *J. Phys. Oceanogr.*, **42**(12), 2185–2205.

Straub, D. N., 1996: An inconsistency between two classical models of the ocean buoyancy driven circulation. *Tellus A*, **48**(3), 477–481.

Tailleux, R., 2013: Available potential energy density for a multicomponent Boussinesq fluid with arbitrary nonlinear equation of state. *Journal of Fluid Mechanics*, **735**, 499–518.

Tandon, A. and C. Garrett, 1996: On a Recent Parameterization of Mesoscale Eddies. *J. Phys. Oceanogr.*, **26**(3), 406–411.

Thomas, L. N., A. Tandon, and A. Mahadevan, 2008: Submesoscale Processes and Dynamics. In: *Ocean Modeling in an Eddying Regime*, pp. 17–38. American Geophysical Union.

Thompson, K. R., D. G. Wright, Y. Lu, and E. Demirov, 2006: A simple method for reducing seasonal bias and drift in eddy resolving ocean models. *Ocean Modelling*, **13**(2), 109–125.

Thomsen, S., C. Eden, and L. Czeschel, 2014: Stability Analysis of the Labrador Current. *J. Phys. Oceanogr.*, **44**(2), 445–463.

Trenberth, K. E. and J. M. Caron, 2001: Estimates of Meridional Atmosphere and Ocean Heat Transports. *J. Climate*, **14**(16), 3433–3443.

Tulloch, R. and K. S. Smith, 2009: Quasigeostrophic Turbulence with Explicit Surface Dynamics: Application to the Atmospheric Energy Spectrum. *J. Atmos. Sci.*, **66**(2), 450–467.

Vallis, G. K., 2006: *Atmospheric and Oceanic Fluid Dynamics*. Cambridge University Press, Cambridge, U.K.

Viebahn, J. and C. Eden, 2010: Towards the impact of eddies on the response of the Southern Ocean to climate change. *Ocean Modelling*, **34**(3–4), 150–165.

Waite, M. L. and P. Bartello, 2004: Stratified turbulence dominated by vortical motion. *Journal of Fluid Mechanics*, **517**, 281–308.

Waite, M. L. and P. Bartello, 2006: The transition from geostrophic to stratified turbulence. *Journal of Fluid Mechanics*, **568**, 89–108.

Wright, D. G. and T. F. Stocker, 1991: A Zonally Averaged Ocean Model for the Thermohaline Circulation. Part I: Model Development and Flow Dynamics. *J. Phys. Oceanogr.*, **21**(12), 1713–1724.

Wright, D. G., T. F. Stocker, and D. Mercer, 1998: Closures Used in Zonally Averaged Ocean Models. *J. Phys. Oceanogr.*, **28**(5), 791–804.

Wright, D. G., C. B. Vreugdenhil, and T. M. C. Hughes, 1995: Vorticity Dynamics and Zonally Averaged Ocean Circulation Models. *J. Phys. Oceanogr.*, **25**(9), 2141–2154.